Centro de Investigación y de Estudios Avanzados del Instituto Politécnico Nacional

Departamento de Física

Multi estados del modelo de materia oscura de campo escalar

T E S I S

para obtener el grado de

Doctor en ciencias

Presenta

Jordi Solís López

Asesor

Dr. Tonatiuh Matos Chassin

Ciudad de México, México.
21 de enero de 2022

Centro de Investigación y de Estudios Avanzados del Instituto Politécnico Nacional

Physics department

Multistate scalar field dark matter

T H E S I S

submitted in fulfillment of the requirements for the
Doctor of Philosophy degree

by

Jordi Solís López

Advisor

PhD. Tonatiuh Matos Chassin

Mexico city, Mexico.
January 21, 2022

A mis padres

Agradecimientos

A mi asesor Dr. Tonatiuh Matos Chassin por todo su apoyo y enseñanza.

Al CONACYT por el apoyo financiero que contribuyó a la realización de este posgrado.

A toda mi familia y amigos que siempre han estado a mi lado.

A Isabel por todo su amor y cariño que me ha dado desde que la conozco y por todo el apoyo que me ha brindado en los malos y buenos momentos durante el doctorado.

A mis sinodales Dra. Tula Bernal Marín, Dr. Francisco Shidartha Guzmán Murillo, Dr. Josué De Santiago Sanabria y Dr. Alfredo Cruz Orea por sus revisiones, comentarios y aportaciones.

A Malú y al personal de la coordinacion académica, Mariana y Rosemary, por toda su ayuda incondicional para los trámites administrativos que se tienen que realizar.

Resumen

Desde la primera mitad del siglo pasado se empezaron a encontrar inconsistencias entre las predicciones teóricas y las observaciones astronómicas que dieron lugar a la introducción de un nuevo tipo de materia en el universo, la materia oscura. Se han propuesto diferentes modelos de materia oscura o de teorías gravitacionales alternativas para evitar la introducción de este tipo de materia. El modelo más popular, simple y exitoso hasta el momento es el modelo de materia oscura fría, en éste, la materia oscura está compuesta de partículas masivas no relativistas que interactúan débilmente con la materia ordinaria. Aunque este modelo ha sido muy exitoso a nivel cosmológico, a nivel galáctico tiene algunos problemas, uno de los cuales, conocido como el problema de los planos de galaxias satélite, es estudiado en este trabajo a través de un modelo alternativo conocido como materia oscura de campo escalar.

Este modelo de materia oscura ha sido capaz de ajustar las observaciones cosmológicas al mismo nivel que el modelo estándar y ha podido resolver de manera natural muchas de las dificultades a escalas astronómicas que el modelo estándar no ha podido por lo que ha empezado a ganar mucha atención en la comunidad científica.

En este trabajo revisamos los problemas abiertos del modelo de materia oscura fría a escala astronómica, dando especial atención al problema de los planos de galaxias satélite, posteriormente se revisan los aspectos generales del modelo de materia oscura de campo escalar, para después estudiar una visión alternativa del modelo donde los halos galácticos de materia oscura ahora están compuestos por estados excitados axialmente simétricos. Finalmente este tipo de halos se propone para explicar algunos de los aspectos del problema de los planos de galaxias satélite como es la distribución anisotrópica de las galaxias satélites que orbitan alrededor de nuestra Vía Láctea.

Abstract

From the first half of the last century, inconsistencies began to be found between theoretical predictions and astronomical observations that led to the introduction of a new type of matter in the universe, dark matter. Different models of dark matter or alternative gravitational theories to avoid the introduction of this type of matter have been proposed. The most popular, simple, and successful model so far is the cold dark matter model, in which dark matter is composed of massive non-relativistic particles that weakly interact with ordinary matter. Although this model has been very successful at the cosmological level, at the galactic level it has some problems, one of which, known as the planes of satellite galaxies problem, is studied in this work through an alternative model known as scalar field dark matter.

This dark matter model has been able to adjust the cosmological observations to the same level as the standard model, and it has been able to naturally solve many of the difficulties on astronomical scales that the standard model has not, which is why it has started to gain a lot of attention in the scientific community.

In this work we review the open problems of the cold dark matter model on an astronomical scale, paying special attention to the planes of satellite galaxies problem, later we review the general aspects of the scalar field dark matter model, and then study an alternative vision of the model where the galactic dark matter halos are now composed of axially symmetrical excited states. Finally, this type of halos is proposed to explain some of the aspects of the planes of satellite galaxies problem, such as the anisotropic distribution of satellite galaxies orbiting our Milky Way.

Contents

List of Figures

List of Tables

Chapter 1

Introduction

The standard cosmological model Λ cold dark matter (ΛCDM) and the cosmological observations are consistent with a universe consisting of $\sim 68.4\%$ dark energy, $\sim 26.6\%$ cold dark matter and ~ 4.9 % baryons (all particles of the Standard Model of Elemental Particles). In this model, the dark energy is modeled as a constant Λ in the Einstein equations, and the dark matter as non-relativistic, collisionless (cold) particles that interact only gravitationally. dark matter is the main topic of this work.

Dark matter and dark energy are two types of exotic matter that, although together make more than 90% of the universe, have not been directly detected yet, and their nature and behaviour are not fully understand. Dark energy is the name given to a kind of matter (or mechanism) responsible of an accelerating expansion of the universe, while dark matter is a kind of matter that is not visible (does not interact with electromagnetic fields -dark-) but is necessary to explain cosmological and astrophysical observations as we will discuss in the following section.

1.1 Dark matter

First hints that something was not been matching between theory expectations and observations were given since the beginning of the last century, with the realization that to match the observed velocity dispersion of Milky Way stars with the modeled one, a nonvisible matter had to be present in the galaxy. Later, with the observation of galaxy clusters, the problem became more evident, Fritz Zwicky estimated the mass and velocity dispersion of the galaxies belonging to the Coma cluster, observed and predicted velocity dispersion mismatched by one order of magnitude and implied a excessive large mass-to-light ratio of the galaxies within the cluster [Zwicky, 1937]. A missmatch between galaxy masses inferred from the dynamics and the predicted by models in the Virgo cluster were also found.

Not only in galaxy clusters but in the galaxies them selves, dark matter was perceived by means of the rotation curves (the circular velocity of the stars within a galaxy as a function of its galactocentric distance). As well as on the galaxy clusters, in the beginning of the XIX century, the first measurements of the circular velocity of stars within the Andromeda a.k.a. Messier 31 (M31) galaxy were made. Later on rotation curve measurements of others spiral galaxies were made, all of those showing almost flat rotation curves at large radii, the circular

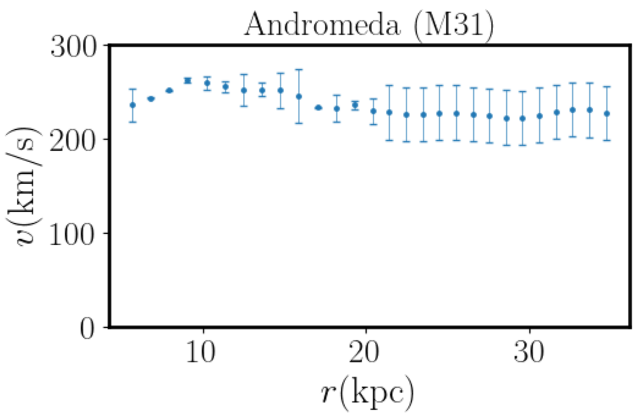

Figure 1.1 Andromeda (M31) galaxy rotation curve a flat tail is observed at large radii ($r >$ 20kpc) instead of a keplerian tail.

velocities of stars at large radii were larger than the expected by a stellar disk. In Figure 1.1 the Andromeda galaxy rotation curve is plotted, a flat tail is observed at large radii instead of the expected keplerian fall.

In the 60's and 70's with the coming of radio astronomy, it was possible to measure the 21cm spectral line of hydrogen emission in galaxies (the change of hyper fine states of hydrogen electrons in the ground state) and hence the rotation curves of galaxies. The photometry measurements of M31 improved as well [Rubin and Ford, 1970], by comparing the scale length of an exponential stellar disk of the photometric fit and the 21 cm rotation curve Freeman [1970] noted the lack of matter in this galaxy (and in others later) and that the distribution of this matter had to be very different from the exponential distribution of a stellar disk.

To explain this missing (non-visible) matter some candidates where proposed. Massive compact objects with low or null luminosity like Jupiter-like planets, brown, red and white dwarf stars, black holes and neutron stars, among others. Although this massive astronomic compact halo objects (MACHOs) are the most obvious and reasonable candidates, MACHOs can be only a few contribution of the dark matter in the universe [J. Hegyi and A. Olive, 1983]. Non-baryonic objects have been proposed too, for example the primordial black holes, black holes formed before the big bang nucleo synthesis, because of the low formation rate, they could not be sufficient to describe all dark matter in the universe.

The favorite candidate for the nonbaryonic dark matter is the cold dark matter model in which dark matter consist on weak-interacting massive particles (WIMPs), these particles are collisionless, weakly selfinteractive, and weakly and gravitationally interactive with baryons. Unfortunately the attempts to detect WIMPs directly or indirectly [Gaskins, 2016] have no successful results, and a large range of parameters thought to be detectable has not been measured.

Cold dark matter N-body simulations of structure formation are successful in reproducing the observed structure pattern of clusters of galaxies, filaments and voids [White et al., 1987]. The structures grow bottom-up hierarchically, the small over densities collapse first and then they merge to form larger objects. Simulations also show that the density profiles of the halos have self-similar shapes [Navarro et al., 1997, Wang et al., 2020], all the density profiles fit the universal Navarro-Frenk-White (NFW) profile at all scales [Navarro et al., 1997], the profile is proportional to r^{-1} ('cuspy') at small radii, and decays as r^{-3} for large radii.

Besides the already mentioned rotation curves of galaxies and the observations in galaxy clusters, without the dark matter component in the universe, it is difficult to explain:

- The observed anisotropies in the cosmic microwave background radiation [Peebles, 1982, Springel et al., 2005].
- The large-scale structure formation in the universe [White et al., 1987, Springel et al., 2005].
- The galactic formation process [Springel et al., 2005].
- The interaction in the galaxy cluster pair 1E0657-56 (the Bullet cluster): The collision of two galaxy clusters leads to a separation of stellar matter (the galaxies, behaving as collisionless particles and detected trough optical images), and the x-ray emitting plasma clouds (slowed down by ram pressure, and detected by X-ray imaging). As the X-ray plasma is the dominant visible (baryonic) matter, the gravitational potential should trace its distribution with lensing reconstructions.

  The lensing reconstruction of Clowe et al. [2006] pointed that the potential traced the distribution of another collisionless matter. There where a displacement between the peaks of the reconstructed gravitational potential and the brightest cluster galaxies and an offset of the the peaks of the reconstructed gravitational potential and the plasma clouds [see Figure 1 of Clowe et al., 2006], so the presence of another source of gravitational potential in the system (dark matter) was needed.
- Other micro-lensing observations in galactic clusters, like the observation of ringlike structures [Jee et al., 2007].

Although Λ cold dark matter describes observations well at cosmological scales (~ 1 to ~ 15000 Mpc), it is in apparent conflict with some observations on small scales (< 1 Mpc) some examples are:

- The core-cusp problem: The best candidates to study the internal structure of dark matter halos are the dark matter dominated galaxies, where the uncertainty of the mass-to-light ratio of the baryonic matter to account for their mass contribution is not a problem. The dwarf spiral galaxies are dark matter dominated from distances of 1 kpc. The problem is that their rotation curves indicate the presence of a constant dark matter density in the center of galaxies $\rho \sim r^0$ (a core) [Moore, 1994, Flores and Primack, 1994], it has actually a logarithmic inner slope on the order $\alpha = -0.2$ [Oh et al., 2011, de Blok et al., 2003], while the halos of cold dark matter simulations present a cusp density in the center $\rho \sim r^{-1}$[Dubinski and Carlberg, 1991, Navarro et al., 1997] ($\alpha = -0.2$). Although better resolution simulations have been made [for example Navarro et al., 2010, Stadel et al., 2009], all of them still show the cusp central density at small radii.
- The missing satellites problem: The number of subhalos (halos that host dwarf galaxies) of Milky Way-like halos predicted by cold dark matter simulations is much larger than the observed number of satellite galaxies of the Milky Way [Klypin et al., 1999, Moore

et al., 1999]. The Milky Way galaxy halo should contain $O(10^3)$ satellite galaxies with mass $\sim 10^8 M_\odot$ while in the Local Group only $O(10)$ are actually seen.

- The "too big to fail" problem [Boylan-Kolchin et al., 2011, 2012]: "The most massive satellites should be "too big to fail" at forming galaxies if the lower-mass satellites are capable of doing so" [Bullock and Boylan-Kolchin, 2017]. The subhalos of Milky Way-like halos in Λ cold dark matter simulations are too dense to host galaxies like the bright ($L_V > 10^5 L_\odot$) dwarf satellites observed in the Milky Way . There should be at least ten subhalos (bright satellites) in the Milky Way with circular velocities $v > 25$ km/s, while the Milky Way satellites have 12 km/s < v < 25 km/s. The same problem is also observed with non satellite galaxies of the Milky Way in the Local Group [Papastergis, E. et al., 2015] and in the satellites of the Andromeda galaxy [Tollerud et al., 2014].

- The diversity of dwarf galaxy rotation curve shapes [Santos-Santos et al., 2020]: There is a great diversity in dwarf galaxies rotation curves with the same maximum circular velocity $v_{\rm max}$, this diversity goes from fast rising rotation curves to slow rising rotation curves . The observation of this great diversity contrasts with the expected identical cold dark matter rotation curves for galaxies with the same $v_{\rm max}$ resulting from self-similar NFW profiles of cold dark matter simulations. This problem is also related with the core-cusp problem, in the low rising rotation curves there is a lack of matter in the galaxy center that is associated with a core dark matter density.

- The relations between baryonic properties and kinematic properties like the baryonic Tully-Fisher relation or the radial acceleration relation.

  The baryonic Tully-Fisher relation $M_b = A v_f^4$ ($A = 47 \pm 6\ M_\odot \mathrm{km}^{-4}\mathrm{s}^4$) is obtained from data of gas-rich galaxies, the baryonic mass M_b is the sum of the stellar and gas contributions and is related to the flat circular velocity v_f (the velocity at which the rotation curve tends to become flat) to the fourth power. This relation is a prediction of MOND (see below) but it is not obtained in the Λ cold dark matter model, in this theory the predicted power is 3 [McGaugh, 2012].

  Another prediction of MOND, not obtained in the Λ cold dark matter model is the radial acceleration relation that is obtained from data of elliptic, spiral, dwarf spheroidal and irregular galaxies, here, a correlation between g_{obs} the observed acceleration traced by the rotation curves and g_b the acceleration due to the observed distribution of baryons is found $g_{obs} = g_b \left(1 - e^{-\sqrt{g_b/g^\dagger}}\right)^{-1}$ [Lelli et al., 2017].

- The planes of satellite galaxies problem: there is an anisotropic distribution of satellite galaxies in the Milky Way , Andromeda and Cen A galaxy systems, satellites appear to be distributed and co-orbiting within planes. This will be addressed in detail in Section 1.2.

To help solving the cold dark matter issues several alternatives have been proposed, some examples are:

- Warm dark matter [Colin et al., 2000, Narayanan et al., 2000, Abazajian et al., 2001]: In this model the warmions are particles with light mass $m_{\rm WDM} \sim 1\mathrm{keV/c}^2$ that could be for example massive neutrinos, sterile neutrinos, gravitinos, majorons (pseudo-Goldstone bosons), shadow-world neutrinos or mirror-world neutrinos [Sommer-Larsen and Dolgov, 2001]. One difference between warm dark matter and cold dark matter is that warmons suppress the power spectrum at small scales limiting the substructure formation and acting like cold dark matter at large scales.

- Nonthermally produced WIMPs [Lin et al., 2001]: When WIMPS have this origin, the power spectrum is also dumped at small scales that will imply less substructure and less cuspy halo cores and thus making WIMPS still good dark matter candidates.

- Self-interacting cold dark matter [Spergel and Steinhardt, 2000, Rocha et al., 2013]: In this scenario, dark particles are still cold and nondissipative but now they have self-interactions that could be attractive or repulsive, with a large scattering cross section (much larger than the dark matter annihilation cross section) and the particle mass goes from 1 MeV to 10 GeV. This model predict spherical cores in halos and a lower number of satellites.

- Feedback effects of baryonic matter on the halo profile [Governato et al., 2010, Garrison-Kimmel et al., 2013]: To explain the too-big-to-fail problem, adding dynamical effects of supernova feedback to the numerical simulation has been proposed, unfortunately, the number of supernovae necessary to decrease the core densities is too large to be able to solve the problem.

- Ultra light boson particles: This model will be addressed in detail in Section 1.1.1

Instead of adding an unknown type of matter, the modification of the gravitational law has also been studied. For example:

- Modified Newtonian dynamics (MOND): The aim of this phenomenological theory is to modify the Newtonian dynamics in the limit of small accelerations $a \ll a_0$ to no longer require the existence of dark matter , here $a_0 \sim 1.2 \times 10^{-10}\text{m/s}^2$ is a constant introduced in this model to modify the acceleration a respect to the newtonian acceleration a_N as $a \approx \sqrt{a_N a_0}$ so the acceleration of a test particle due to the presence of a body of mass M at a distance r would be $a^2 = MGa_0 r^{-2}$, to recover the Newtonian limit of high accelerations $a \gg a_0$ the introduction of a function $\mu(a/a_0)$ is necessary, this function has to be $\mu(a/a_0) \approx 1$ for $a \gg a_0$ and $\mu(a/a_0) \approx a/a_0$ for $a \ll a_0$, the disadvantage is that the functional form of $\mu(a/a_0)$ has to be put in by hand [Milgrom, 1983a,b,c, 2002].

1.1.1 Scalar Field Dark Matter

An alternative model to cold dark matter that started in the 90's proposed by Sin [1994], Ji and Sin [1994] and Lee and Koh [1996] is the Scalar Field Dark Matter . Although it began in those years it was not until 1999 with Guzmán et al. [1999], and after, in the 2000's with Guzmán and Matos [2000], Matos et al. [2000], Matos and Ureña-López [2000], Sahni and Wang [2000], Hu et al. [2000], Matos and Ureña-López [2001], Arbey et al. [2001, 2002] and Arbey et al. [2003] that the first systematic studies of this model began.

This model has been rediscovered or/and appeared under various names, like Fuzzy Dark Matter [Hu et al., 2000], Quintessential Dark Matter [Arbey et al., 2001], Wave Dark Matter

[Bray, 2010, Schive et al., 2014a], ultra-light Dark Matter [Hui et al., 2017], ultralight axionic particles [Membrado et al., 1989] and Bose-Einstein condensate dark matter [Böhmer and Harko, 2007] among others. Here the most general and descriptive name: Scalar Field Dark Matter will be used [for reviews of SFDM, see Magaña and Matos, 2012, Suárez et al., 2014, Rindler-Daller and Shapiro, 2014, Marsh, 2016, Niemeyer, 2020].

The scalar field dark matter model assumes the dark matter in the universe is comprised of ultralight spinless boson particles. At cosmological scales it was first analyzed in Matos and Ureña-López [2000], the boson mass μ is one of the free parameters of the model and determines the cut-off scale of the mass power spectrum. The mass has to be ultra-light to mimic the behavior of the cold dark matter model at cosmological scales, this is, it would have the same mass power spectrum [Matos and Ureña-López, 2001] and the same cosmic microwave background (CMB) temperature power spectrum [Hlozek et al., 2015]. Due to the success at large scales (> 1 Mpc) of the Λ cold dark matter , any correct theory of the description of the universe must differ only at small (< 1 Mpc) scales.

The scalar field dark matter is an ultra-light complex (or real) scalar field Φ minimally coupled to gravity, and interacting only gravitationally with baryonic matter. The equation of motion of such a scalar field is the Klein-Gordon equation

$$\Box\Phi + \frac{dV(\Phi)}{d|\Phi|^2}\Phi = 0$$

where the potential $V(\Phi)$ accounts for the self-interactions of the scalar field, and the d'Alambert operator is defined as $\Box = \nabla_\mu \nabla^\mu = \nabla_\mu g^{\mu\nu}\nabla_\nu$, here ∇_m is the covariant derivative and the metric tensor $g_{\mu\nu}$ is the solution of the Einstein field equations

$$G_{\mu\nu} = \frac{8\pi G}{c^4} T_{\mu\nu}$$

where $G_{\mu\nu}$ is the Einstein tensor, $T_{\mu\nu}$ the energy momentum tensor and G the gravitational constant.

The scalar field potential usually is assumed to be of the form

$$V(\Phi) = \frac{\mu^2 c^2}{\hbar^2}|\Phi|^2 + \frac{\Lambda}{2}|\Phi|^4$$

when the autointeraction $\Lambda = 0$ it is called the free field case or fuzzy dark matter .

In the cosmological treatment, a flat, homogeneous and isotropic universe is assumed using the Friedman-Lemaitre-Robertson-Walker (FLRW) metric

$$ds^2 = -c^2 dt^2 + a^2(t)\left(dr^2 + r^2 d\Omega^2\right)$$

where a is the scale factor and $d\Omega^2 = d\theta^2 + \sin^2\theta d\phi^2$.

To model the evolution of the universe the presence of baryons, radiation (and neutrinos), dark energy and dark matter is required, the dark matter is modeled with a scalar field, dark energy with a cosmological constant Λ or a scalar field (quintessence), and the rest of ingredients as perfect fluids with different equations of state.

The Einstein equations with the FLRW metric become the Friedman equations, these together with the Klein-Gordon equation and the continuity equations of the rest of perfect fluids dictate the evolution of the universe:

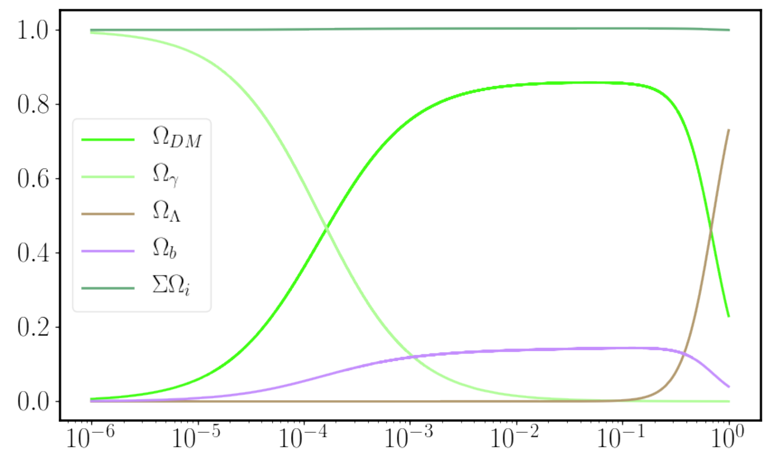

Figure 1.2 Evolution of the density parameters as function of the scale factor.

$$
\begin{aligned}
\dot{H} &= -\frac{4\pi G}{c^4}\left(\dot{\Phi}^2 + \frac{4}{3}\rho_\gamma + \rho_b\right) \\
1 &= \Omega_{DM} + \Omega_\gamma + \Omega_b + \Omega_\Lambda \\
\ddot{\Phi} &= -3H\dot{\Phi} - \frac{dV(\Phi)}{d\Phi} \\
\dot{\rho}_i &= -3H(\rho_i + P_i)
\end{aligned}
\tag{1.1}
$$

where Ω_i are the energy densities defined as $\Omega_i = \frac{8\pi G}{3c^4}\frac{\rho_i}{H^2}$, ρ_i and P_i are the density and pressure of dark matter (DM), baryons (b), radiation and neutrinos (γ), each satisfying different equation of state $\omega = P/\rho$.

The system (1.1) is solved using as boundary conditions the energy densities observed today Ω_{i0}. In Figure 1.2 the dimensionless energy densities are plotted as function of the scale factor. The standard cosmological evolution is recovered.

Analyzing the evolution of the perturbations gives the essential differences with the cold dark matter model. First, the evolution of the dark matter density contrast being almost the same as the cold dark matter one except at $a < 10^{-4}$ where small differences are observed [Matos and Ureña-López, 2000]. Second, the scalar field Jeans length provides a cut-off of the mass power spectrum at small scales as long as the boson mass be ultra-light $\mu \approx O(10^{-24}) \sim O(10^{-22})$ eV/c^2 [Hu et al., 2000, Matos and Ureña-López, 2001, Marsh and Ferreira, 2010, Harko, 2011a, Magaña et al., 2012] reducing the abundance of low mass subhalos and being more consistent with the amount of satellite galaxies observed in the Local Group.

Another difference with the cold dark matter model is the central density distribution in scalar field dark matter halos. The scalar field dark matter model could solve the cusp-core problem [Hu et al., 2000, Harko, 2011b, Su and Chen, 2011, Robles and Matos, 2012, Robles et al., 2018]. Fitting the rotation curves of low-surface-brightness galaxies a core in the dark matter central profile with logarithmic slope $\alpha = -0.27$ is found Robles and Matos [2012].

The early cosmological scalar field dark matter-only simulation of Woo and Chiueh [2009] found cusps in central galactic regions, similar to the cold dark matter ones. Later, better cosmological dark matter-only simulations of structure formation [Schive et al., 2014a,b, Schwabe et al., 2016, Veltmaat and Niemeyer, 2016, Mocz et al., 2017, Levkov et al., 2018, Hopkins, 2019, Mocz et al., 2019, 2020] revealed early-forming cores in the dark matter density profile resulting from the Heisenberg uncertainty principle. The resulting halos consisted thus of a central core, a.k.a soliton [Chavanis, 2011, Marsh and Pop, 2015, Chen et al., 2017, Levkov et al., 2018], surrounded by an NFW-like envelope generated by a quantum interference pattern.

The cosmological simulation of Schive et al. [2014a] shows a direct comparison between the cold dark matter and the scalar field dark matter models at large scales, and this was done by running both simulations with the same cosmological parameters. In their Figure 1, they intentionally suppress the high k-modes in their cold dark matter plot to see only the large-scale modes. Almost the same pattern of filaments and voids is observed for both models.

The Einstein-Klein-Gordon system in the weak field and non-relativistic limits (the Newtonian limit) becomes the Gross-Pitaevskii-Poisson system [Suárez and Chavanis, 2015]:

$$i\hbar\frac{\partial\Psi}{\partial t} = -\frac{\hbar^2}{2\mu}\nabla^2\Psi + \mu V\Psi + \Lambda|\Psi|^2\Psi, \tag{1.2}$$

$$\nabla^2 V = 4\pi G|\Psi|^2 \tag{1.3}$$

where $\Psi(\vec{x},t)$ is the order parameter, $V(\vec{x},t)$ the self-gravitational potential (the potential produced by the dark matter density $|\Psi|^2$ itself) and the short-range autointeraction

$$\Lambda = \frac{2\pi\hbar^2 a}{\mu}$$

is related with the scattering length a of the bosons. When there is no self-interaction $\Lambda = 0$, the system becomes the Schrödinger-Poisson system. So at galactic scales the dark matter is ruled by the Gross-Pitaevskii-Poisson system.

Boson stars [Ruffini and Bonazzola, 1969] are the stationary $\Psi(t,\vec{x}) = e^{-\frac{iEt}{\hbar}}\Phi(\vec{x})$ solutions of the Schrödinger-Poisson system (relativistic boson stars are stationary solutions of the Einstein-Klein-Gordon system) and describe a system of self-gravitating bosons all in the ground state. The total mass of the Bose-Einstein condensate goes as

$$M \sim \frac{m_P^2}{\mu}$$

where the plank mass is defined as

$$m_p^2 = \frac{\hbar c}{G}.$$

For a system of bosons of $\mu \sim 1$ GeV/c^2 the mass is extremely small $M \sim 10^{-19}M_\odot$ but for ultra-light particles $\mu \sim 10^{-22}$ eV/c^2 this mass is $M = 10^{12}M_\odot$, adequate for astronomical objects, in particular, it is interesting to model dark matter halos.

When the auto-interaction Λ is considered, the total mass and size of the configuration are highly increased, even for small values of Λ [Colpi et al., 1986, Lee and Koh, 1996, Lesgourgues et al., 2002] (see Figure 1.3 where the total mass N doubles the mass of the non auto-interactive

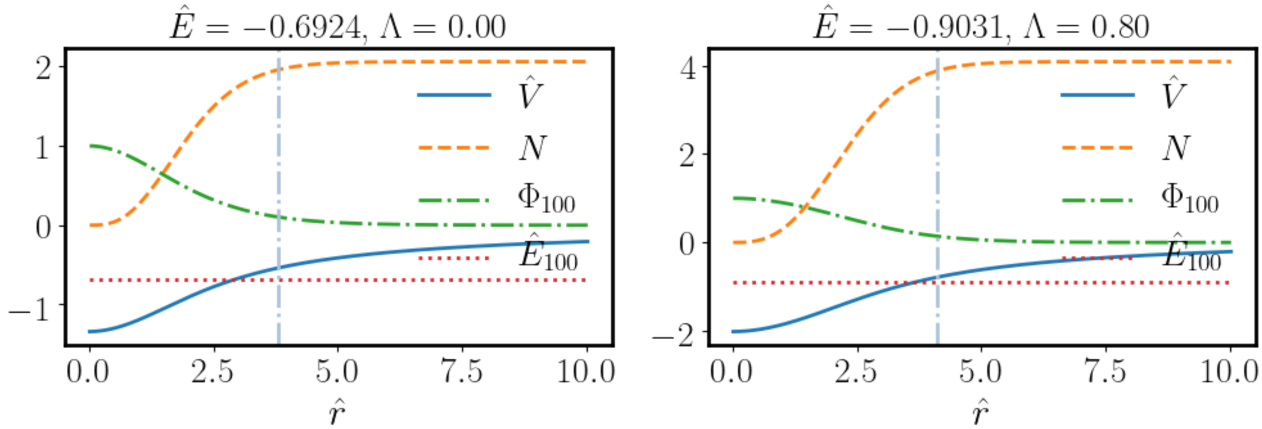

Figure 1.3 Boson star, ground state equilibrium solution of the Gross-Pitaevskii-Poisson system with $\Phi(0) = 1$ and $\Lambda = 0$ (left panel) or $\Lambda = 0.8$ (right panel) fixed. The order parameter Φ_{100}, the dimensionless gravitational potential $\hat{V} = V/c^2$, the dimensionless energy eigen-value $\hat{E}_{100} = E_{100}/(\mu c^2)$ and the dimensionless enclosed mass $N = \mu M/m_P^2$ at the dimensionless radius $\hat{r} = \mu cr/\hbar$ are plotted.

case $\Lambda = 0$ when $\Lambda = 0.8$). The auto-interaction may be repulsive $\Lambda > 0$ ($a > 0$) or attractive $\Lambda < 0$ ($a < 0$) in which case there is a bound in the mass M of the configuration for an equilibrium state to exist [Chavanis, 2011].

The stationary spherically symmetric Gross-Pitaevskii-Poisson (as well as the Schrödinger-Poisson) system, with fixed Λ, scalar field amplitude $\Phi(0)$ and specific boundary conditions of the scalar field and gravitational potential, is solved as an eigenvalue problem, with eigenvalues E and $V(0)$. The ground state $\Phi_{100}(r)$ is the solution for which the wave function has zero nodes, and the excited states Φ_{n00} solutions with $n-1$ nodes. In figure 1.3 the ground state equilibrium solution of the Gross-Pitaevskii-Poisson system is plotted for both the non-interactive $\Lambda = 0$ and the auto-interactive $\Lambda = 0.8$ cases with fixed value of the amplitude at $\Phi(0) = 1$.

In the scalar field dark matter model the dark matter halos are then self-gravitating Bose-Einstein condensates spanning over galactic scales because of the assumed ultralight mass that also gives a galactic-scale de Broglie wavelength that leads to quantum-like phenomena at this scale.

The non-relativistic Schrödinger-Poisson system was first used in Sin [1994] describing the macroscopic wave function of galactic halos to fit rotation curves , Sin obtained a particle mass $\mu = 3 \times 10^{-23}$ eV/c^2, nevertheless this was done using spherical excited states (Φ_{500}) that later turn out to be unstable, excited states settle down onto the ground-state equilibrium configuration [Guzmán and Ureña López, 2004]. Only the ground-state equilibrium configuration is stable under radial and non-radial perturbations [Bernal and Guzmán, 2006].

Dark matter halos modeled as the stationary states of the Gross-Pitaevskii-Poisson system have been used to fit the universal rotation curves [Persic et al., 1996] of large high and low-luminosity spiral galaxies resulting in a boson particle mass in the range $\mu = 4 \times 10^{-24}$ eV/c^2 to $\mu = 1.6 \times 10^{-23}$ eV/c^2 [Arbey et al., 2001], and then, considering repulsive autointeraction Lesgourgues et al. [2002] show that the mass could go further to $\mu \sim 1$ eV/c^2 when Λ is in the range $[1, 10^{-4}]$. Lora et al. [2012] also modeled halos as the ground state of the Gross-Pitaevskii-

Poisson system in dwarf galaxies to demonstrate that a mass of the scalar field 3×10^{-23} eV/c^2 < $\mu < 1 \times 10^{-22}$ explain the distribution of globular clusters in Fornax and the longevity of the cold clump in Ursa Minor.

Using the Thomas Fermi approximation (that becomes exact for large number of particles), stationary states have been also used to fit low-surface-brightness galaxies rotation curves [Böhmer and Harko, 2007] and dwarf disk galaxies rotation curves [Arbey et al., 2003, Böhmer and Harko, 2007]. In Silverman and Mallett [2002] the rotation curves of Andromeda (a large spiral galaxy) and M33 (a dwarf spiral galaxy) were fitted obtaining a particle mass $\mu = 10^{-24} - 10^{-23}$ eV/c^2.

The dwarf spheroidal (dSph) galaxies are highly dark matter dominated systems and allow to compare the dark matter profiles with stellar kinematical data through a Jeans analysis. In Schive et al. [2014a] they use the velocity dispersion measurements of the Milky Way's dSph satellite galaxy Fornax and the core+NFW-tail fitted profile of their simulation

$$\rho = \begin{cases} \frac{\rho_{sol}}{(1+(r/r_{sol})^2)^8} \text{ for r} < \text{r}_\epsilon \\ \frac{\rho_{NFW}}{(1+(r/r_s))^2(r/r_s)} \text{ for r} > \text{r}_\epsilon \end{cases}$$

to find a scalar field dark matter particle mass $\mu = 8.0^{+1.8}_{-2.0} \times 10^{-23}$ eV/c^2. Marsh and Pop [2015] use another method, they fit the slopes of the mass profiles of two dSph: Fornax and Sculptor, and they find a upper bound of the particle mass $\mu < 1.1 \times 10^{-22}$ eV/c^2 and the result that there is no bound in the parameters of the NFW-tail part of the profile implying a preference of the data to cores. With two ultra-faint galaxies of the Local Group: Draco II and Triangulum II Calabrese and Spergel [2016], find a particle mass $\mu = 5.6 \times 10^{-22}$ eV/c^2 for Draco and $\mu = 3.8 \times 10^{-22}$ eV/c^2 for Triangulum using the measurements of the half-light mass $M_{1/2}$. Chen et al. [2017] made a Jeans analysis fitting 8 dSph Milky Way satellite galaxies individually and then fitting all 8 simultaneously finding $\mu = 1.18^{+0.28}_{-0.24} \times 10^{-22}$ eV/c^2.

Nevertheless later an unbiased Jeans analysis on Fornax and Sculptor Milky Way satellite galaxies fitting the velocity dispersion (averaged with the luminosity) of sub populations of stars within the dwarf galaxies gave an upper bound of $\mu < 4 \times 10^{-23}$ eV/c^2 [González-Morales et al., 2017].

Analysis with other types of dark matter dominated galaxies has also been done, for example, with Dragonfly 44 ultra-diffuse galaxy Wasserman et al. [2019] obtained a particle mass of $\mu = 3 \times 10^{-22}$ eV/c^2, and with the dwarf irregular Antlia II Milky Way satellite galaxy Broadhurst et al. [2020] found a boson mass of $\mu = 1.1 \times 10^{-22}$ eV/c^2.

In [Matos and Ureña López, 2007] a related idea that was proposed for the first time: the mixed states (a.k.a. multistates), in which a complete galaxy halo in the scalar field dark matter scenario is described by the gravitational co-existence of different spherically symmetric eigenstates. Each state is described by a Schrödinger equation and the gravitational potential evolves with the Poisson equation sourced by contribution of all states. When all boson particles are in one state the system reduces to the usual Schrödinger-Poisson system. Matos and Ureña López [2007] consider the multistate configuration composed of the ground state Φ_{100} and the first spherically symmetric excited state Φ_{200}, they realized that the first peak in the rotation curve due to this multistate is set by the ground state and the size of the halo is set by the excited state. The excited state produce another peak at larger radii that delays the Keplerian fall of the rotation curve . This configurations are stable always that the mass ratio between the mass

Table 1.1 Summary of the properties of the dwarf galaxies.

Name	gas content	luminosity $L_\odot$	mass $M_\odot$	M_V mag	found
dIrr	gas-rich		$< 10^9$	-16 to -13.0	in field
BCD	gas-rich		$< 10^9$	$M_B > -18$	in field
dE	gas-poor	$\sim 10^9 - \sim 10^7$	$\sim 10^7 - \sim 10^9$	-18 to -14.0	in galaxy clusters
dSph	gas-poor	$\sim 10^7 - \sim 10^5$	$\sim 10^5 - \sim 10^7$	-17 to -8	as satellites
UFD	gas-poor	$\sim 10^5 - \sim 10^3$	$\sim 10^2 - \sim 10^5$	-8.0 to -1.5	as satellites

of the excited state and the ground state N_{200}/N_{100} is less than 1.1 [Ureña López and Bernal, 2010].

Recently, Guzmán and Ureña López [2020] showed a general method to find axisymmetric multistate configurations, this method encompasses the single states (the usual Newtonian boson stars), the spherical multistates of [Matos and Ureña López, 2007], the Newtonian l-boson stars [Alcubierre et al., 2018], and they present the new axi-symmetric multistates. Furthermore, Guzmán and Ureña López [2020] show a possible formation process of this axi-symmetric configurations by the collision of single states. The simplest of the multistate axi-symmetric configurations consisting on the ground state Φ_{100} and the dipolar state Φ_{210} is stable [Guzmán, 2021].

The multistate scenario is just beginning and will be the center of attention in this work.

1.2 Planes of satellite galaxies problem

There are two giant galaxies (galaxies with stellar mass $M_* \sim 10^{10} M_\odot$) in the Local Group (at distance < 1.5Mpc), our own, the Milky Way and the Andromeda galaxies, both having a set of small dwarf galaxies ($M_* \leq 10^9 M_\odot$) gravitationally bounded to them. The giant galaxies are called host galaxies while their gravitationally bounded dwarf galaxies are called satellite galaxies. There are also field dwarf galaxies, galaxies that are not gravitationally bounded to a host. In Figures 1.4, 1.7 and 1.11 the satellites of the two host galaxies in the Local Group are plotted.

Dwarf galaxies are defined as galaxies with stellar masses $M_* \leq 10^9 M_\odot$, or with circular velocities below 100 km/s, or with magnitude in the V band $M_V \leq -17$ mag (or $M_B \leq -16$ mag in the blue band). There are two groups of dwarf galaxies: gas-rich galaxies with ongoing star formation and gas-poor galaxies with old stellar populations. The former includes blue compact dwarfs (BCDs) and dwarf irregular galaxies (dIrrs), and they are mostly field dwarf galaxies. The latter includes dwarf elliptical galaxies (dEs), dwarf spheroidals (dSphs) and ultrafaint dwarfs (UFDs), and they are mostly satellite galaxies of spiral and elliptical galaxies or members of galaxy clusters (see Table 1.1).

Given their stellar mass, dwarf galaxies in the Local Group are classified in three classes: the bright dwarfs with $M_*/M_\odot = O(10^7) - O(10^9)$, the classical dwarfs with $M_*/M_\odot = O(10^5) - O(10^7)$, and the ultra-faint dwarfs with $M_*/M_\odot = O(10^2) - O(10^5)$.

Although cosmological simulations with the standard cold dark matter model predict that satellites must be isotropically distributed in the host halo and with random motions (in a Milky

Way-like galaxy should have ~ 500 sub-halos within 500kpc), in the Milky Way system this does not happen. In Figure 1.7 all classical and ultra-faint Milky Way satellites are plotted, beside the lack of satellites, it is evident the anisotropic distribution, all satellites are close to the polar axis and there is an empty zone, although there exists also a zone where the satellites might be obscured by the Milky Way stellar disc because our position inside the galaxy (see Figure 11 in Bullock and Boylan-Kolchin [2017]), this obscured zone does not cover all the empty area where not even ultra-faint satellites have been discovered.

Since the seventy's it has been realized that Milky Way satellites appear to be in an anisotropic disc-like planar structure [Lynden-Bell, 1976], in those years there were no predictions of structure formation with cosmological simulations in cold dark matter , it was until 2005 with cosmological simulations results in hand that Kroupa et al. [2005] make the first study of the distribution of the 16 then-known Milky Way satellites, by fitting the positions of N satellites, $N = 3, 4, ..., 16$. Kroupa et al. found that satellites lay in a disk-like structure perpendicular to the Milky Way stellar disc and that satellites could not come from an isotropic distribution even when they remove from the sample three satellites that were known to be kinematically related. Kroupa et al. also obtained the first hints that the satellites where co-orbiting, with the few (four) available measurements of the satellite's orbital poles being almost parallel with the vector normal to the fitted plane.

Once that the proper motion measurements of the classical satellites were available, it was possible to find the galactocentric velocities of the satellites and hence, their angular momenta. In Figure 1.5 (see also Figure 1 in Metz et al. [2008]) the orbital pole (angular momentum direction) of the classical Milky Way satellites is plotted in galactocentric spherical coordinates.

Metz et al. [2008] used the currently available proper motion measurements of 8 classical satellites to obtain the orbital poles, and they realized that most of these satellites co-orbit in a planar disk-like structure. This is, the mean direction of the satellites' orbital poles ($l = 177°, b = -9.4°$) were almost parallel with the normal to the fitted plane for the 11 Milky Way satellites ($l = 157.3°, b = -12.7°$)[Metz et al., 2007, 2008], see Figure 1.6 where an edge-on view of the plane of a posterior fit by Lipnicky and Chakrabarti [2017] of the Classical satellites is shown. The flattened structures of the simulated cold dark matter sub-halos did not show that behaviour, instead the sub-halos tended to disperse Metz et al. [2008]. Later on Pawlowski and Kroupa [2013] used the proper motions of all 11 classical satellites and came to the same conclusion (with 8 of the 11 satellites co-orbiting within the plane).

There is a richer structure because not only satellites, but globular clusters (30 objects) form a similar disk plane (see Figure 5 in Pawlowski et al. [2012]) with normal vector ($l = 144°, b = -4.3°$) closely aligned with the disk of satellites, furthermore, the normal vectors of seven streams of stars and gas closely align with the disk of satellites normal vector too [Pawlowski et al., 2012]. This richer structure around the Milky Way is called the vast polar structure (VPOS).

Because of the lack of satellites around the Milky Way (there were only 11 known bright satellites called the classical satellites, see Figure 1.4), people start looking (searching for stellar over-densities) for less luminous satellites. Since 2005, with the Sloan Digital Sky Survey (SDSS) [York et al., 2000] sixteen fainter Milky Way satellite galaxies have been discovered. This galaxies are fainter than the faintest classical Milky Way satellites (Ursa Minor and Draco), so they were called ultra-faint satellites. In Figure 1.7 all the Milky Way satellites are plotted in galactocentric coordinates.

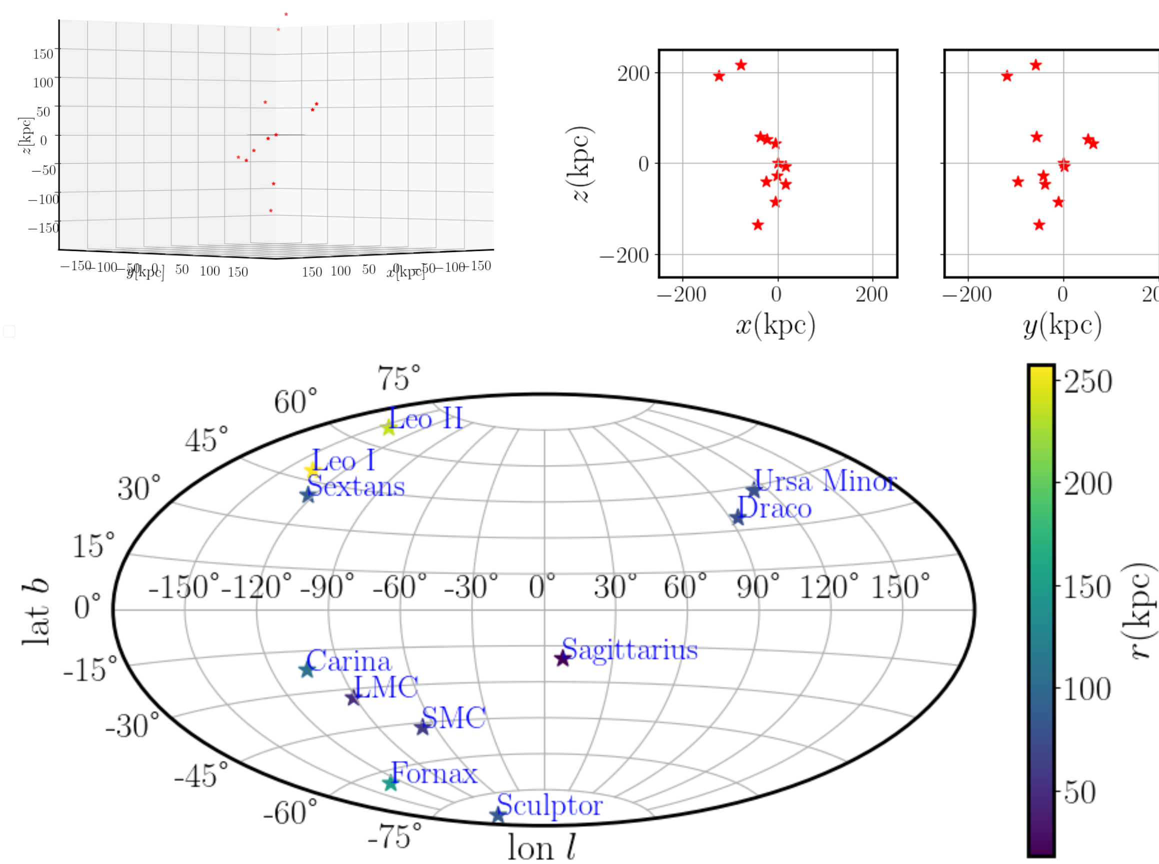

Figure 1.4 The Milky Way Classical satellites. Upper left: 3D plot of in galactocentric Cartesian coordinates The horizontal line represents the stellar disk of the Milky Way. Upper right: projection in the xz and yz planes in galactocentric cartesian coordinates of the 3D distribution. Bottom: aitoff projection in latitude b and longitude l galactocentric spherical coordinates of the 3D distribution. In color scale the distance from the galactic center to the satellite is plotted. Data from Pawlowski and Kroupa [2013]

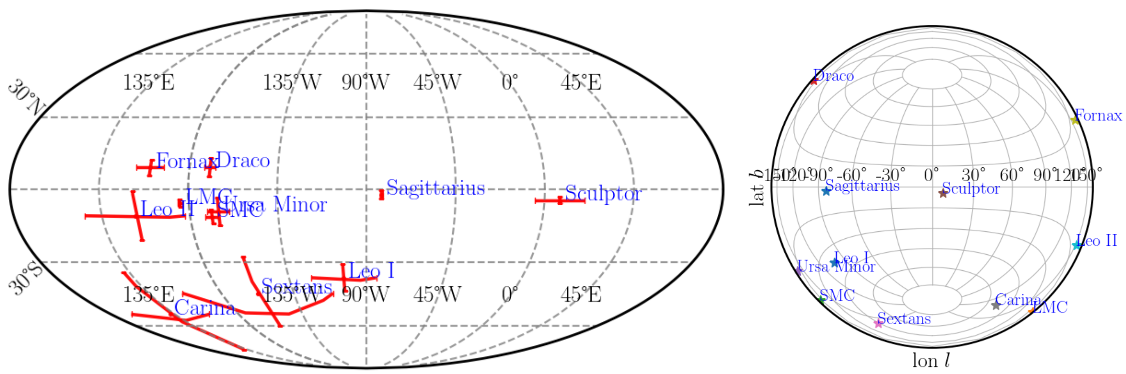

Figure 1.5 Mollweide (left panel) and Lambert (right panel) projections in latitude b and longitude l galactocentric spherical coordinates of the orbital poles (angular momentum direction) of the Milky Way classical satellites. Data from Pawlowski and Kroupa [2013]

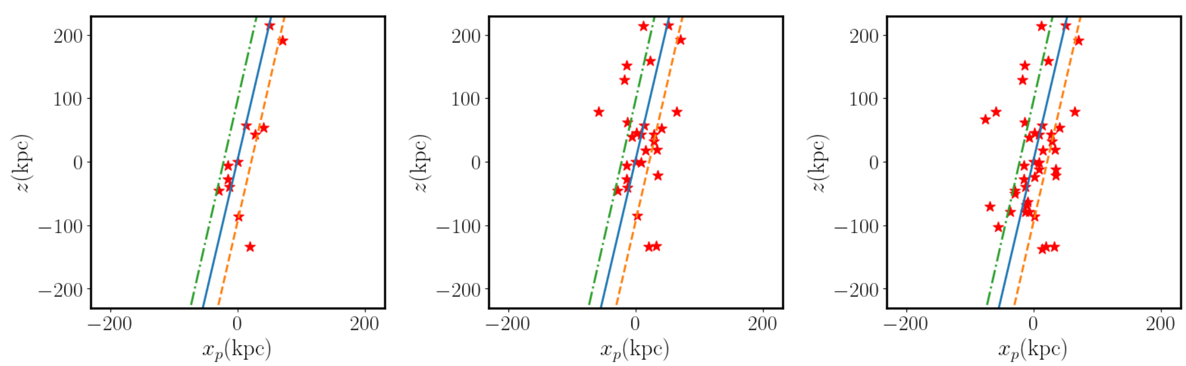

Figure 1.6 Left: Fitted plane of the Milky Way classical satellites made by Lipnicky and Chakrabarti [2017], the dotted lines are the rms height of the plane, the sample is the same as in Figure 1.4 but rotated an angle $\varphi = 158°$, rotated coordinate is $x_p = x\cos\varphi + y\sin\varphi$ so that the plane is viewed edge-on. Middle: same fit but now plotting the ultra-faint satellites of Figure 1.7 too. Right: same fit but now plotting the new satellite candidates of Figure 1.8 too.

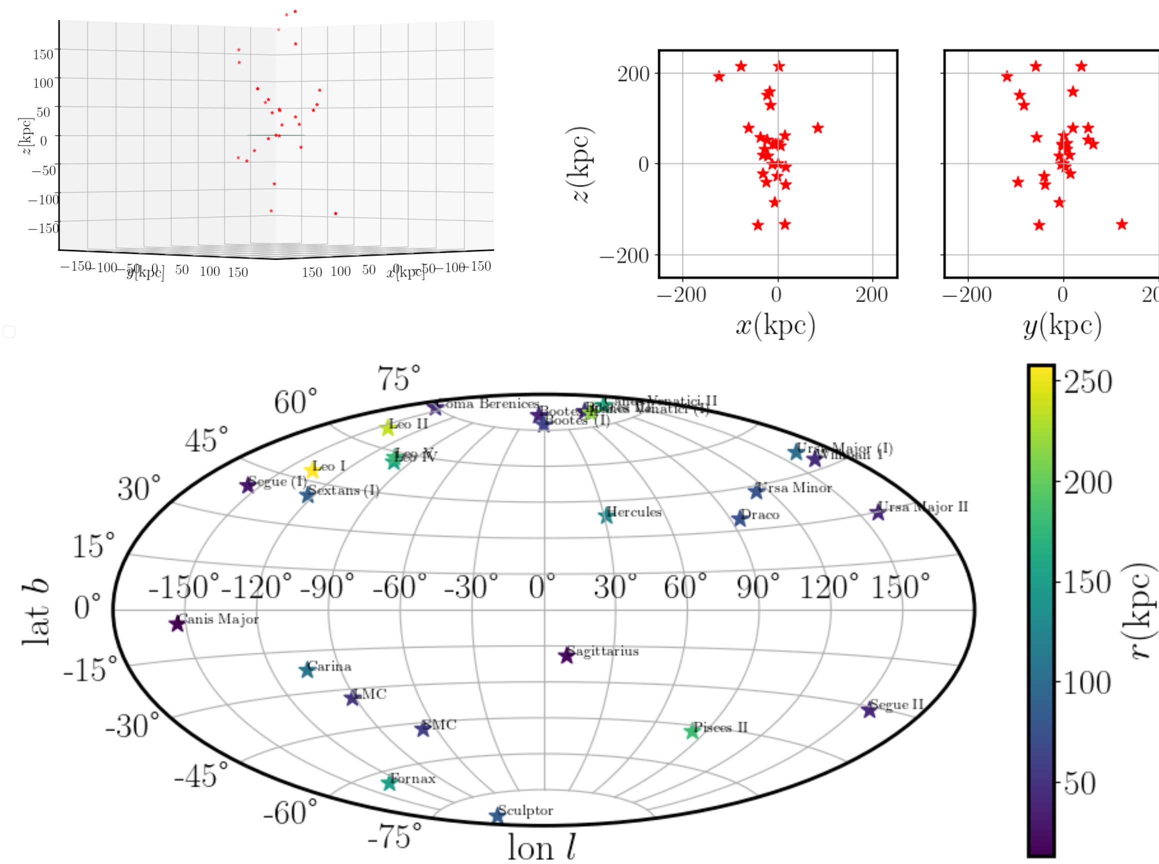

Figure 1.7 Same as in Figure 1.4 but for the Milky Way Classical + ultra-faint satellites. Data from Pawlowski et al. [2013].

With 11 classical plus 13 currently known ultra-faint Milky Way satellites, Kroupa, P. et al. [2010] fitted the positions of the galaxies and found that even with the addition of the new satellites, a disk-like structure is still preserved, with a normal vector pointing to ($l = 156.4°, b = -2.2°$) and a 57.8 kpc thickness. Furthermore the ultra-faint satellites fitted independently define a very similar (less thick and more inclined) plane to the classical satellites one with a normal vector pointing to ($l = 151.4°, b = 9.1°$) [Kroupa, P. et al., 2010].

The SDSS covers only the north galactic region, so new surveys began to explore beyond the SDSS footprint, specifically on the southern galactic hemisphere. More than 20 objects have been discovered: star clusters, unconfirmed dwarf galaxy candidates, and unclassified objects. In Table 1.2 the name, distance from the galactic center (r_{MW}), and galactocentric coordinates (x, y, z) of all the Milky Way satellites together with the new discovered objects are written, and in Figure 1.8 are plotted in galactocentric coordinates. With the addition of 11 new satellite candidates to the known Milky Way satellite data, Pawlowski et al. [2015] found a similar plane with normal pointing to ($l = 164°, b = -6.9°$) and a width of 61.8 kpc, and thinner 42.6 kpc, if 4 outliers are removed from the fitting sample, hence this new objects are consistent to be part of the VPOS.

More recently, the Gaia Collaboration in its Data Release 2 (DR2) [Gaia Collaboration, 2018] independently measured the proper motion of the 11 classical Milky Way satellites, Pawlowski and Kroupa [2020] combined it with the old data to find the best measurements of the orbital poles, in Figure 1.9 the orbital poles with the combined sample are plotted, compare with Figure 1.5 error bars are now considerably smaller, specifically the ones from Sextans and Carina dwarfs, Carina's orbital pole now pointing so much closer to the orbital pole cluster around $l \sim 180°$ consisting of LMC, Draco, Ursa Minor, SMC, Leo II, Fornax and Sculptor (counter orbiting $l \sim 180°$ out of phase). The mean direction of the 7 most concentrated orbital poles points at ($l = 179.5°, b = -9°$) Pawlowski and Kroupa [2020] close to the direction of the normal to the fitted plane for the 11 Milky Way satellites ($l = 157.3°, b = -12.7°$)[Metz et al., 2007, 2008]. This result confirms that classical Milky Way satellites co-orbit close to the plane formed by their positions increasing the tension with the cold dark matter model simulations where only less than 0.1 % of the systems [Pawlowski and Kroupa, 2020] have that much satellite orbital poles as aligned as the Milky Way has.

In figure 1.10 a compilation of all normal vector directions to the fitted planes of Milky Way satellites made by different authors is plotted. The directions of the average orbital pole of the 7, 6, and 5 most concentrated orbital poles are also shown.

Since 2006, it was realized that in the Andromeda system something similar was occurring, 9 of the then-known 15 Andromeda satellites were aligned in an almost polar ($l = 107.1°, b = 6.9°$) plane [Koch and Grebel, 2006]. In Metz et al. [2007] using two fitting algorithms and two different data sets the similar conclusion was found a thin (18.8kpc width) plane with 8 galaxies but not in a polar direction ($l = 168°, b = -26.7°$), and then adding a sample of 11 more dwarf galaxies [Metz et al., 2009]. Metz et al. [2007] also gave the first hint to a kinematic correlation of satellites in the Andromeda system.

Later on, with a better sample of 27 satellites of the PAndAS [1] database, it was confirmed that 13 satellites were aligned in a thin (of ~ 14 kpc width) and extensive (400 kpc diameter) plane [Ibata et al., 2013], the Great Plane of Andromeda (GPoA), they were not only aligned but

[1]Pan-Andromeda Archaeological Survey

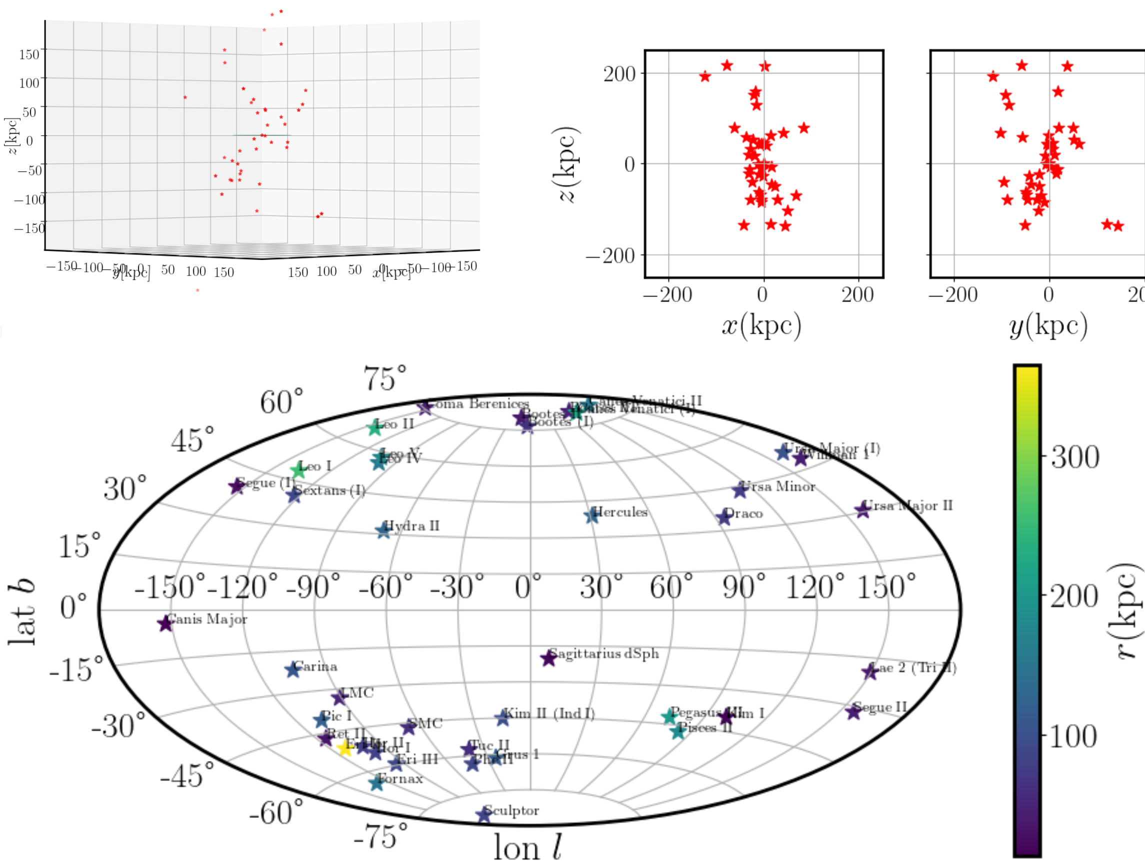

Figure 1.8 Same as in Figure 1.4 but for the Milky Way Classical + ultra-faint satellites + new satellite candidates. Compare with Figure 1.7, new objects fill the southern galactic hemisphere mostly at $90^\circ < l < 120^\circ$. Data from [Pawlowski et al., 2015] see also Table 1.2.

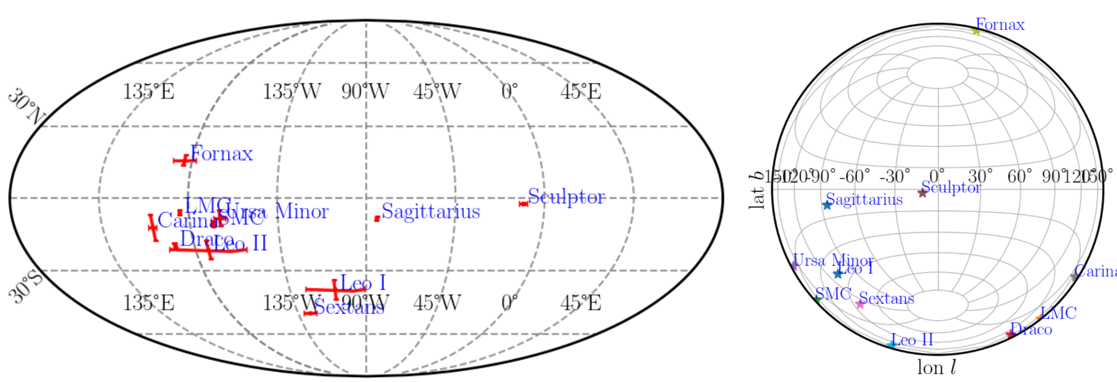

Figure 1.9 Same as in Figure 1.5 but with the data of Gaia DR2. Data from Pawlowski and Kroupa [2020]

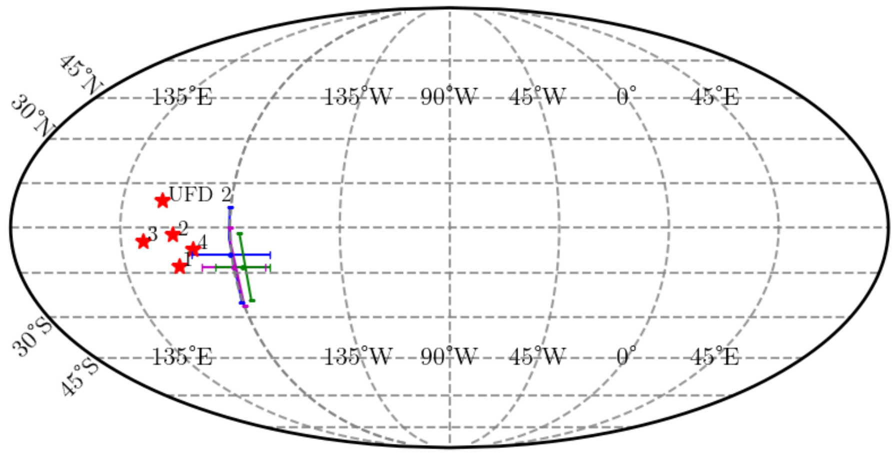

Figure 1.10 Red star markers are the normal of the fitted plane of the positions of the Milky Way satellites on galactocentric longitude l and latitude b. Results by 1: Metz et al. [2008], 2: Kroupa, P. et al. [2010], UFD 2: Kroupa, P. et al. [2010] considering the ultra faint dwarf satellites in the fit, 3: Pawlowski et al. [2012], 4: Pawlowski et al. [2015]. Markers with error bars are the directions of the average orbital pole of the 7 (blue), 6 (magenta) and 5 (green) most concentrated orbital poles [Pawlowski and Kroupa, 2020].

their motions were non-isotropic, they all appeared to have their orbital poles almost parallel indicating that the satellites in the plane structure were rotating [Ibata et al., 2013], see Figure 2 of Ibata et al. [2013] where the satellites and the plane are plotted.

The satellite distribution in the Andromeda system doesn't look as anisotropic as the Milky way's, because the GPoA only consists of almost half of the total known satellites, only a part of the satellites is anisotropic, one could ask your self if the whole group of Milky Way satellites something similar could be happening. Indeed, but only from 2 to 6 of the 27 classical and ultra-faint Milky Way satellites could be part of an isotropic distribution [Pawlowski, 2016] with a very high confidence.

In a posterior study of Conn et al. [2013], the authors found a more thin ($\sim$ 12 kpc width) plane disc of 15 satellites, along with very interesting asymmetries, the plane is perpendicular to the Milky Way stellar disc, is viewed edge-on from the Milky Way and is orthogonal to the Milky Way VPOS.

Beside the 2 already mentioned planes in the Local Group, the VPOS and the GPoA, Pawlowski et al. [2013] found that there are two more dwarf galaxy planes in the Local Group, one with 9 field dwarf galaxies and the other one with 5 (see Figure 9 in Pawlowski et al. [2013]) with only one non-satellite galaxy of the Local Group not belonging to either.

Some possible explanations of the planes of satellites problem within the cold dark matter frame have been proposed, for instance, that the alignment of satellites is due to the accretion of dwarf galaxies along filaments, or due to the accretion of dwarf galaxies in groups (see for example Pawlowski [2018] and references therein) but these explanations do not completely solve the problem or have inconsistencies.

One viable process in which a spatially and kinematically correlated system like the VPOS and GPoA systems could form, is the formation of galaxies in gas-rich tidal tails formed by

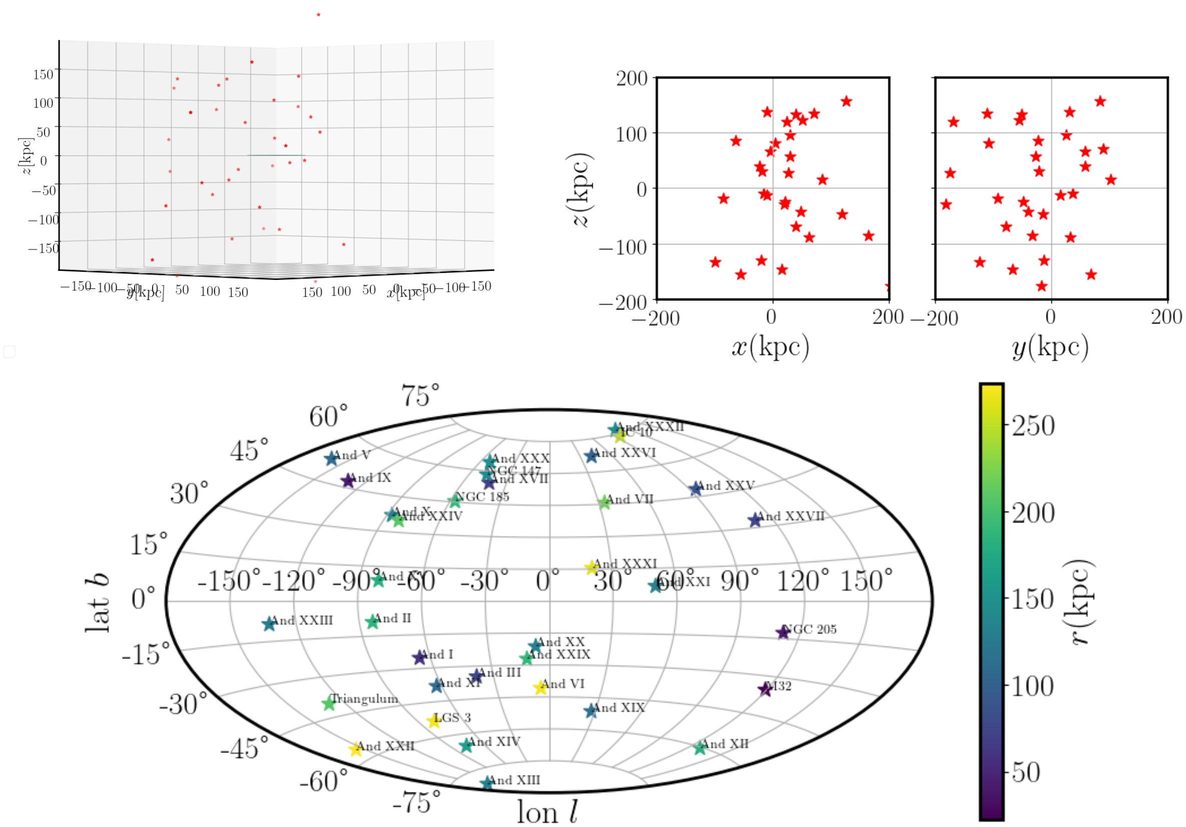

Figure 1.11 Same as in Figure 1.4 but for the Andromeda (M31) satellites. Data from Pawlowski et al. [2013].

the interaction of galaxies [Pawlowski, M. S. et al., 2011], the problem is that, in the cold dark matter model this tidal dwarf galaxies are dark matter free galaxies opposite to the observed dark matter dominated Milky Way dSph satellites. There are works studying tidal dwarf galaxies in alternative dark matter models, for example Foot and Silagadze [2013].

Other possibility is that the Milky Way and Andromeda are atypical galaxies in which this unexpected coherent distribution of dwarfs happens. Nevertheless, in addition to the Local Group there exists another group within the Local Volume (volume at distance < 10Mpc), the Centaurus Group, in which the Cen A subgroup, a set of 31 satellites interacts gravitationally with the elliptical galaxy Centaurus A (Cen A), displays similar behaviours. Having three systems so close together with the same behaviours makes that explanation insufficient.

First the anisotropy of the distribution of satellites in the Cen A subgroup was discovered, 27 of the then-known 29 Cen A satellites were found to lie in two almost parallel planes (see Figure 1 in Müller et al. [2016]) one with 346 kpc major axis, 73 kpc minor axis and 77 kpc width; the second one with 250 kpc major axis, 46 kpc minor axis and 55.7kpc width [Tully et al., 2015], in Figure 1.12 the Cen A satellites are plotted, colored in red, blue and grey meaning that they belong to plane 1, 2, or not belonging to neither, respectively. But with the later discovery of more satellites it turn out to be just one 69kpc wide and 309kpc major axis long planar structure orthogonal to the dust plane [Müller et al., 2016].

Later in 2018 the coherent motion of satellites and planetary nebulae was discovered. Back then with the current knowledge of 31 Cen A satellites of which 16 had measured line-of-sight (LoS) velocities Müller et al. [2018] find that 14 out of the 16 satellites could be co-rotating within the plane. The probability of finding such a system in cosmological simulations was 0.1% and 0.5 % for the Millenium-II [Boylan-Kolchin et al., 2009] a DM-only N-body simulation and for the Illustris [Vogelsberger et al., 2014] a dark matter plus gas physics, star formation and feedback simulation, respectively.

Recently Müller et al. [2021] studied the Cen A system with the addition of more discovered satellites, adding a total of 28 to their analysis, and they state that the probability of finding such a system in the Illustris cosmological simulation was 0.2% with the exception that in the simulations those structures are not long lived.

Noticing that now three galaxies, Cen A, Milky Way, and M31, of two different types (two spirals and one elliptical) show the same phenomenon (see Figure 1 on Pawlowski [2018]), indicates the possible need of an alternative explanation based on different dark matter models.

In this work, the possibility that multistate equilibrium configurations of an ultra light bosonic scalar field, considered as dark matter halos, could explain this observation due to the anisotropic (axially symmetric) mass density of the halo is explored. In these axisymmetric halos, there are regions where the mass density is higher, or equivalently local minimums of the halo gravitational potential that will influence the trajectories of particles and structures within the halo, and make them distribute in a non-isotropic manner. Explaining the observed anisotropic distribution of satellites and might eventually explain the coherent motion of satellite galaxies in the Milky Way, Andromeda and Centaurus A systems.

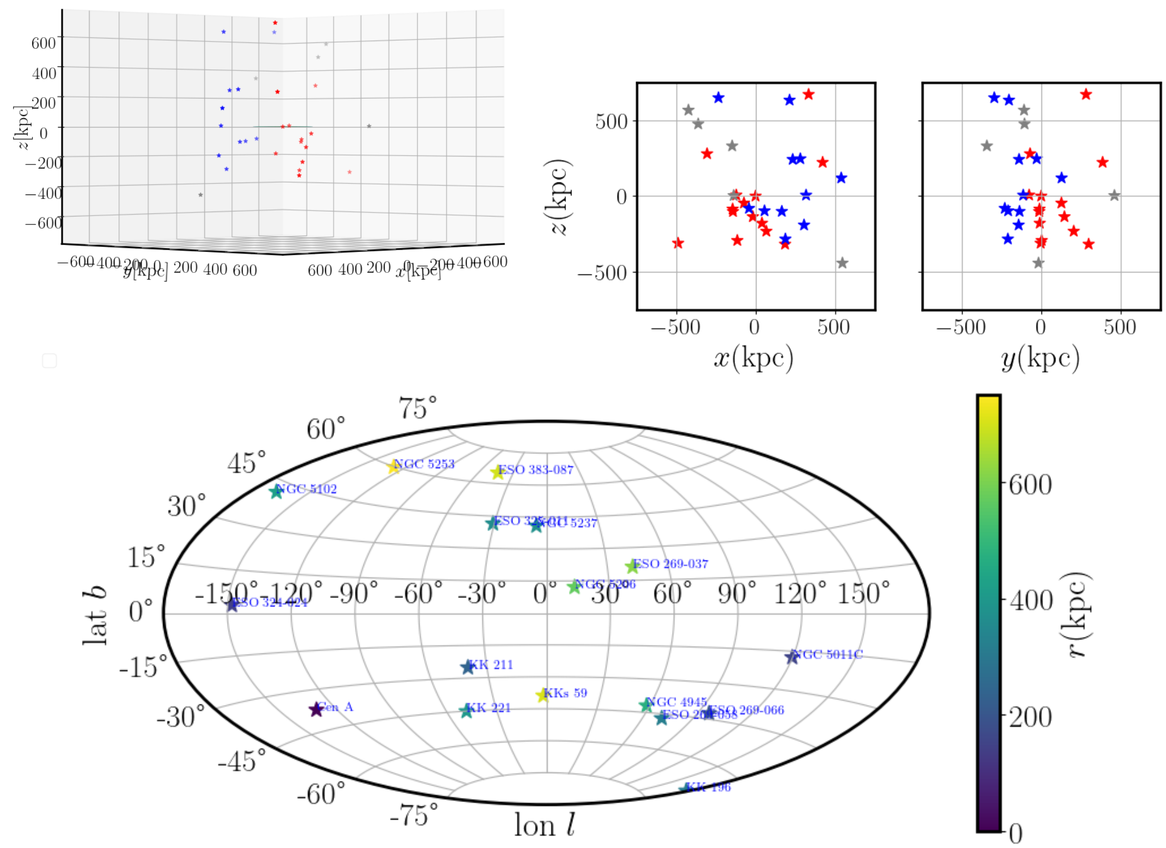

Figure 1.12 The CenA satellites. Upper left: 3D plot of in galactocentric Cartesian coordinates. Upper right: projection in the xz and yz planes in galactocentric cartesian coordinates of the 3D distribution. Satellites are colored in red, blue and grey meaning that they belong to plane 1, 2, or not belonging to neither, respectively. Bottom: aitoff projection in latitude b and longitude l galactocentric spherical coordinates of the 3D distribution. In color scale the distance from the galactic center to the satellite is plotted. Data adapted from Müller et al. [2018].

Table 1.2: Milky Way satellites and satellite galaxy candidates. Distance from the center of the Milky Way (r_{MW}) and galactocentric Cartesian coordinates (columns 3,4,5). Data from Pawlowski et al. [2015]

Name	r_{MW} (kpc)	x (kpc)	y (kpc)	z (kpc)	Type
Sagittarius	18.4	17.1	2.5	-6.4	Classical
Large Magellanic Cloud (LMC)	50.0	-0.6	-41.8	-27.5	
Small Magellanic Cloud (SMC)	61.2	16.5	-38.5	-44.7	
Draco	75.9	-4.4	62.2	43.2	
Ursa Minor	77.8	-22.2	52.0	53.5	
Sculptor	86.0	-5.2	-9.8	-85.3	
Sextans I	89.0	-36.7	-56.9	57.8	
Carina	106.8	-25.1	-95.9	-39.8	
Fornax	149.3	-41.3	-51.0	-134.1	
Leo II	235.9	-77.3	-58.3	215.2	
Leo I	257.4	-123.6	-119.3	191.7	
Canis Major	13.4	-11.9	-6.2	-1.0	ultra-faint
Segue I	27.9	-19.4	-9.5	17.7	
Ursa Major II	38.0	-30.6	11.6	19.2	
Bootes II	39.5	6.6	-1.7	38.9	
Segue II	40.8	-31.8	13.9	-21.4	
Willman 1	42.9	-27.7	7.6	31.8	
Coma Berenices	44.9	-10.6	-4.3	43.4	
Bootes III	45.8	1.3	6.9	45.3	
Bootes I	64.0	14.8	-0.8	62.2	
Ursa Major I	101.6	-61.1	19.8	78.7	
Hercules	126.1	84.1	50.7	79.1	
Leo IV	154.8	-15.1	-84.8	128.6	
Canes Venatici II	160.6	-16.5	18.6	158.7	
Leo V	178.6	-21.5	-91.9	151.7	
Pisces II	181.1	14.9	121.7	-133.3	
Canes Venatici I	217.5	2.1	37.0	214.3	
Kim I	19.1	-2.7	14.4	-12.3	Star Cluster
Kim II (Ind I)	98.9	67.5	-17.3	-70.2	
Ret II	33.0	-9.7	-20.4	-24.1	Unclassified
Lae 2 (Tri II)	36.6	-29.8	17.4	-12.2	
Hor II	80.0	-9.6	-48.7	-62.7	
Hor I	83.5	-7.2	-48.0	-67.9	
Phe II	88.1	28.7	-27.2	-78.8	
Eri III	91.2	-4.3	-46.0	-78.7	
Grus 1	116.4	50.6	-23.0	-102.2	
Pic I	121.9	-28.1	-88.2	-79.2	

Continued on next page

Table 1.2 – *Continued from previous page*

Name	r_{MW} (kpc)	x (kpc)	y (kpc)	z (kpc)	Type
Tuc II	59.2	24.4	-20.4	-49.9	Unconfirmed dwarf galaxy
Hydra II	129.0	40.8	-102.4	66.8	
Pegasus III	203.1	44.3	143.5	-136.8	
Eri II	365.0	-86.2	-211.4	-284.7	

Chapter 2

Multistate scalar field dark matter

A system of self-gravitating spinless bosons in the Newtonian and non-relativistic limits is ruled by the Gross-Pitaevskii-Poisson system, in which the order parameter Ψ describes the macroscopic Bose-Einstein condensate , in the special case of null auto-interaction the Gross-Pitaevskii-Poisson reduces to the Schrödinger-Poisson system. When not all boson particles are in the ground state, each state is described by its own Gross-Pitaevskii equation and is gravitationally coupled among the rest through the Poisson equation, resulting in a more general Schrödinger-Poisson system [Matos and Ureña López, 2007, Ureña López and Bernal, 2010]:

$$i\hbar\frac{\partial\Psi_{nlm}}{\partial t} = -\frac{\hbar^2}{2\mu}\nabla^2\Psi_{nlm} + \mu V\Psi_{nlm}, \tag{2.1}$$

$$\nabla^2 V = 4\pi G\sum_{nlm}|\Psi_{nlm}|^2 \tag{2.2}$$

where the wave function of each state is $\Psi_{nlm}(\vec{x},t)$, and $V(\vec{x},t)$ is the gravitational potential sourced by the mass density

$$\rho = \sum|\Psi_{nlm}|^2.$$

If dimensionless stationary states

$$\Psi_{nlm}(t,r,\theta,\varphi) = \frac{\mu c^2}{\hbar\sqrt{4\pi G}}e^{iE_{nlm}t/\hbar}\Phi_{nlm}(r,\theta,\phi) \tag{2.3}$$

are considered, it becomes

$$\nabla^2\Phi_{nlm} - \frac{2\mu}{\hbar^2}(\mu V + E_{nlm})\Phi_{nlm} = 0, \tag{2.4a}$$

$$\nabla^2 V = \frac{\mu^2 c^4}{\hbar^2}\sum_{nlm}|\Phi_{nlm}|^2, \tag{2.4b}$$

the harmonic time-dependence (2.3) of the wave function makes the mass density

$$\rho = \frac{\mu^2 c^4}{4\pi G\hbar^2}\sum_{nlm}|\Phi_{nlm}|^2$$

time independent and hence the gravitational potential time independent too.

If the redefinitions $\hat{V} \equiv V/c^2$, $\hat{E}_{nlm} \equiv \frac{E_{nlm}}{\mu c^2}$ and $\hat{\mu} \equiv \mu c/\hbar$ are made then equations (2.4) become a fully dimensionless, scale-free, system for the quantities Φ_{nlm} and $\hat{V}$:

$$\hat{\nabla}^2\Phi_{nlm} - 2(\hat{V} + \hat{E}_{nlm})\Phi_{nlm} = 0, \tag{2.5a}$$

$$\hat{\nabla}^2\hat{V} = \sum_{nlm} |\Phi_{nlm}|^2, \tag{2.5b}$$

The constant $\hat{\mu}$ has units of length^{-1} and makes the coordinates and the Laplace operator dimensionless: $\hat{r} = \hat{\mu}r$ and $\hat{\nabla}^2 = \frac{1}{\hat{\mu}^2}\nabla^2$.

The enclosed mass at radius r is

$$M(r) = \frac{c^2}{G\hat{\mu}} N(\hat{r}) \tag{2.6}$$

where $N = \sum_{n,l,m} N_{nlm}$ is the dimensionless enclosed mass, and the number of particles N_{nlm} of each state is

$$N_{nlm} = \int |\Phi_{nlm}|^2 \hat{r}^2 d\hat{r} d\Omega.$$

The Schrödinger-Poisson system (2.5) is invariant under the scaling property

$$\left(\hat{r}, \Phi_{nlm}, \hat{V}, \hat{E}_{nlm}, N\right) \to \left(\hat{r}/\lambda, \lambda^2\Phi_{nlm}, \lambda^2\hat{V}, \lambda^2\hat{E}_{nlm}, \lambda N\right) \tag{2.7}$$

for any real parameter λ (see e.g. Guzmán and Ureña López [2004]).

When only a single state is considered there are two free parameters for our model, the particle mass μ and the scaling parameter λ, but whenever more states are considered, extra free parameters appear, those could be, for example, the ratio between wave function amplitudes

$$\zeta \equiv \frac{\psi_{100}(0)}{\psi_{nlm}(0)}$$

or the ratio between total masses

$$\eta = \frac{N_{100}(r)|_{r\to\infty}}{N_{nlm}(r)|_{r\to\infty}}$$

Using this λ parameter, it is possible to construct an infinite number of solutions of the Schrödinger-Poisson system once one solution is known.

The Compton length of the boson particle is

$$L_C = \frac{\hbar}{\mu c} = \frac{1}{\hat{\mu}},$$

and establishes the typical length scale of the configurations, it is useful to fix units in terms of a mass scale as

$$L_C = 0.1\text{pc}\left(\frac{10^{-22}\text{eV}}{\mu c^2}\right),$$

From equation (2.6) the mass scale of the configurations is

$$M_C = \frac{c^2}{G\hat{\mu}} = \frac{m_P^2}{\mu} = \left(\frac{10^{-22}\mathrm{eV}}{\mu c^2}\right) 10^{12}\, M_\odot, \tag{2.8}$$

as mentioned in the introduction, for ultra-light particles this mass is adequate for astronomical objects, like dark matter halos, for example, for $\mu = 10^{-24}$ eV/c^2 this mass is $M_C = 10^{14} M_\odot$.

The physical mass of each multipolar contribution of a multistate configuration is obtained considering the scaling property

$$M_{nlm} = \sqrt{\lambda} N_{nlm} M_C.$$

The circular velocity v_h of a particle under an external axi-symmetric potential $V(r,\theta)$ is

$$v_h^2 = r\frac{\partial V}{\partial r}\bigg|_{\theta=\pi/2}$$

this relation can be written in dimensionless variables

$$\hat{v}_h^2 = \frac{v_h^2}{c^2} = \hat{r}\frac{\partial \hat{V}}{\partial \hat{r}}\bigg|_{\theta=\pi/2},$$

in the special case of the Schrödinger-Poisson system, this circular velocity will also follow a scaling property

$$\hat{v}_h \rightarrow \sqrt{\lambda}\hat{v}_h$$

that will allow us to fit the rotation curves of galaxies.

In what follows dimensionless variables will be used and the ˆ symbol will be dropped for simplicity.

Several cases for the multistate Schrödinger-Poisson system (2.5) can be considered:

1. The simplest possibility is to consider a single state, when all boson particles are in the same state Φ_{nlm}, with n taking only one value $1, 2, ...$, and also for l and m taking one of its possible values $l = 0, 1, .., n-1$ and $m = -l, -l+1, ..., l$. In this case there is only one Schrodinger equation (2.5a) and only one term in the right hand side of Equation (2.5b). It happens that in the single state case only the ground state Φ_{100} is stable [Guzmán and Ureña López, 2004].

2. Newtonian l-boson stars, configurations where the dark matter density in the right hand side of Equation (2.5b) is of the form $\sum_{m=-l}^{l} |\Phi_{nlm}|^2$ with fixed n and l. This configurations are spherically symmetric because of the Unsöld's theorem $\sum_{m=-l}^{l} Y_l^m(\theta,\phi) Y_l^{m*}(\theta,\phi) = \frac{2l+1}{4\pi}$.

3. Multistates, configurations where boson particles are in many different sates. A specific configuration (called from now on multiSFDM) where some particles are in the ground state and some in only one other excited state will be used in this work only. The dark matter density in the right hand side of Equation (2.5b) is then of the form $|\Phi_{100}|^2 + |\Phi_{nlm}|^2$, with fixed n, l and m (this numbers can take the values $n = 2, 3, ...$; $l = 0, 1, .., n-1$; and $m = -l, -l+1, ..., l$), and there is one Schrödinger equation (2.5a) for each state, one for the ground state and one for the excited state.

In the scalar field dark matter model a galaxy halo is modeled as a boson gas in the ground state, a galactic-size boson star. The idea now is that the halo should be described with a collection of states. The number of states and the particular value of the n, l, m parameters in the multistate configuration should depend on the process of evolution and formation of the galaxy interested to model, so in general these parameters should not be able to be set in a general way for all types of galaxies.

2.1 General method for the construction of bound solutions

In this section the general framework of Guzmán and Ureña López [2020] to search for stationary solutions of multistate wave functions of the Schrödinger-Poisson system of equations (2.5) is reproduced in detail.

First the following expression in spherical coordinates for the stationary wave function is assumed

$$\Phi_{nlm}(r,\theta,\varphi) = \sqrt{4\pi} r^l \psi_{nlm}(r) Y_l^m(\theta,\varphi), \tag{2.9}$$

next, the gravitational potential V is expanded as

$$V(r,\theta,\phi) = \sqrt{4\pi} \sum_{l,m} V_{lm}(r) r^l Y_l^m(\theta,\phi) \tag{2.10}$$

where $Y_l^m(\theta,\phi)$ are the spherical harmonics and (n, l, m) can only take the values

$$\begin{aligned} n &= 1, 2, 3, ... \\ l &= 1, 2, ..., n-1 \\ m &= -l, -l+1, -l+2, ..., l-2, l-1, l. \end{aligned}$$

The Laplacian operates in functions expanded in this form as:

$$\nabla^2 F(r,\theta,\phi) = \sqrt{4\pi} \sum_{l,m} Y_l^m(\theta,\phi) r^l \nabla^2_{r_l} F_{lm}(r)$$

where F is a generic function that could be V or Φ_{nlm} and F_{lm} are the radial functions in the expansion in spherical harmonics, and the l-Laplacian operator is defined as

$$\nabla^2_{r_l} \equiv \frac{d^2}{dr^2} + \frac{2(l+1)}{r}\frac{d}{dr}.$$

The multiplication of two spherical harmonics can be written in terms of a third as

$$Y_{l_1}^{m_1}(\theta,\phi) Y_{l_2}^{m_2}(\theta,\phi) = \sum_{l,m} G^{l_1,l_2,l}_{m_1,m_2,m} Y_l^m(\theta,\phi)$$

where

$$G^{l_1,l_2,l}_{m_1,m_2,m} = \sqrt{\frac{(2l_1+1)(2l_2+1)}{4\pi(2l+1)}} \langle l_1, 0, l_2, 0 | l, 0 \rangle \langle l_1, m_1, l_2, m_2 | l, m \rangle$$

are the Gaunt coefficients, as l's and m's are integers the last equation is equivalent to

$$G^{l_1,l_2,l}_{m_1,m_2,m} = \int_{4\pi} Y^{m_1}_{l_1}(\Omega) Y^{m_2}_{l_2}(\Omega) Y^{m*}_{l}(\Omega) d\Omega \tag{2.11}$$

the Gaunt coefficients are nonzero when

$$\begin{aligned} |l_1 - l_2| \leq \quad & l \quad \leq l_1 + l_2, && (2.12a) \\ m \quad & = \quad m_1 + m_2, && (2.12b) \\ l_1 + l_2 + l \quad & \quad \text{is even.} && (2.12c) \end{aligned}$$

Poisson equation

Using equations (2.9, 2.10) Poisson equation (2.5b) becomes

$$\begin{aligned} \sum_{lm} Y^m_l r^l \nabla_{r_l} V_{lm} &= \sqrt{4\pi} \sum_{l_1 m_1} r^{2l_1} \psi^2_{n_1 l_1 m_1} Y^{m_1}_{l_1} (-1)^{m1} Y^{-m_1}_{l_1} \\ &= \sqrt{4\pi} \sum_{l_1 m_1} (-1)^{m1} r^{2l_1} \psi^2_{n_1 l_1 m_1} \sum_{l_2 m_2} G^{l_1 l_1 l_2}_{m_1,-m_1,m_2} Y^{m_2}_{l_2} \end{aligned}$$

because of condition (2.12b) $m_2 = 0$, and then

$$\sum_{lm} Y^m_l r^l \nabla_{r_l} V_{lm} = \sqrt{4\pi} \sum_{l_2} \sum_{l_1 m_1} (-1)^{m1} G^{l_1 l_1 l_2}_{m_1,-m_1,0} r^{2l_1} \psi^2_{n_1 l_1 m_1} Y^0_{l_2}$$

using the linear independence of the spherical harmonics, each (l, m) in the left side is equal to each $(l_2, m_2 = 0)$ in the right side of the previous equation so

$$r^l \nabla_{r_l} V_{l0} = \sqrt{4\pi} \sum_{l_1 m_1} (-1)^{m1} G^{l_1 l_1 l}_{m_1,-m_1,0} r^{2l_1} \psi^2_{n_1 l_1 m_1} \tag{2.13}$$

this is the final expression of the Poisson equation and shows that the gravitational potential V thus does not have azimuthal angle ϕ dependence.

Schrödinger equation

Using equation (2.9) in the Schrödinger equation (2.5a)

$$\begin{aligned} \nabla^2_{r_l} \psi_{nlm}(r) &= 2(V + \Lambda |\Psi_{nlm}|^2 - E_{nml}) \psi_{nlm} \\ &= 2\left(\sqrt{4\pi} \sum_{l_1 m_1} V_{l_1 m_1} r^{l_1} Y^{m_1}_{l_1} + 4\pi\Lambda r^{2l} \psi^2_{nlm} Y^m_l (-1)^m Y^{-m}_l - E_{nml} \right) \psi_{nlm} \\ &= 2\left(\sqrt{4\pi} \sum_{l_1 m_1} r^{l_1} V_{l_1 m_1} Y^{m_1}_{l_1} + 4\pi\Lambda (-1)^m r^{2l} \psi^2_{nlm} \sum_{l_2,m_2} G^{l,l,l_2}_{m,-m,m_2} Y^{m_2}_{l_2} - E_{nlm} \right) \psi_{nlm} \end{aligned}$$

then multiplying both sides of the equation by $Y_l^m Y_l^{m*}$ and integrating all the equation over the solid angle Ω, and using (2.11) results in

$$\nabla^2_{r_l}\psi_{nlm}(r) = 2\left(\sqrt{4\pi}\sum_{l_1 m_1} G^{l_1,l,l}_{m_1,m,m} r^{l_1} V_{l_1 m_1} + 4\pi\Lambda(-1)^m r^{2l}\psi^2_{nlm}\sum_{l_2,m_2} G^{l,l,l_2}_{m,-m,m_2} G^{l_2,l,l}_{m_2,m,m} - E_{nlm}\right)\psi_{nlm}$$

the condition (2.12b) implies that both m_2 and m_1 are zero.

$$\nabla^2_{r_l}\psi_{nlm}(r) = 2\left(\sqrt{4\pi}\sum_{l_1} G^{l_1,l,l}_{0,m,m} r^{l_1} V_{l_1 0} + 4\pi\Lambda(-1)^m r^{2l}\psi^2_{nlm}\sum_{l_2} G^{l,l,l_2}_{m,-m,0} G^{l_2,l,l}_{0,m,m} - E_{nlm}\right)\psi_{nlm} \tag{2.14}$$

the relation (2.14) is the final expression of the stationary Schrödinger equation.

Schrödinger-Poisson system

In summary the Schrödinger-Poisson system is now composed of equations (2.13) and (2.14)

$$\nabla^2_{r_l} V_{l0}(r) = \frac{\sqrt{4\pi}}{r^l}\sum_{n_1,l_1,m_1}(-1)^{m_1} G^{l_1,l_1,l}_{m_1,-m_1,0} r^{2l_1}\psi^2_{n_1 l_1 m_1} \tag{2.15a}$$

$$\begin{aligned}\nabla^2_{r_l}\psi_{nlm}(r) &= 2\left(\sqrt{4\pi}\sum_{l_1} G^{l_1,l,l}_{0,m,m} r^{l_1} V_{l_1 0}\right.\\ &+ \left. 4\pi\Lambda(-1)^m r^{2l}\psi^2_{nlm}\sum_{l_2} G^{l,l,l_2}_{m,-m,0} G^{l_2,l,l}_{0,m,m} - E_{nlm}\right)\psi_{nlm}.\end{aligned} \tag{2.15b}$$

the Gaunt coefficients are nonzero when

$$\begin{aligned}|l_1 - l_2| \le \quad l &\le l_1 + l_2,\\ m &= m_1 + m_2,\\ l_1 + l_2 + l & \quad \text{is even.}\end{aligned}$$

As said before, a specific configuration composed of only two states, the ground state and one excited state will be only used in this work.

2.2 multiSFDM case (100, 21m)

The multiSFDM case (Ψ_{100}, Ψ_{21m}) occurs when the source terms in the Poisson equation (2.15a) are ψ_{100} and ψ_{21m}, in this case the equation is

$$\begin{aligned}\nabla^2_{r_l} V_{l0}(r) &= \frac{\sqrt{4\pi}}{r^l}\left((-1)^0 G^{0,0,l}_{0,0,0} r^0 \psi^2_{100} + (-1)^m G^{1,1,l}_{m,-m,0} r^2 \psi^2_{211}\right)\\ &= \frac{\sqrt{4\pi}}{r^l}\left(G^{0,0,l}_{0,0,0}\psi^2_{100} + (-1)^m G^{1,1,l}_{m,-m,0} r^2 \psi^2_{211}\right)\end{aligned} \tag{2.16}$$

because of (2.12a) the first coefficient $G^{0,0,l}_{0,0,0}$ is non-zero only for $l = 0$, and the second coefficient $G^{1,1,l}_{m,-m,0}$ is non-zero only for $0 \leq l \leq 2$, and because of (2.12c), l can only take the values $l = 0, 2$.

Therefore, there are going to be only two terms in the gravitational potential expansion V_{00} and V_{20}, and thus two equations (2.16):

$$
\begin{aligned}
\nabla^2_{r_0} V_{00}(r) &= \frac{\sqrt{4\pi}}{r^0}\left(G^{0,0,0}_{0,0,0}\psi^2_{100} + (-1)^m G^{1,1,0}_{m,-m,0} r^2 \psi^2_{211}\right) && (2.17a)\\
\nabla^2_{r_2} V_{20}(r) &= \frac{\sqrt{4\pi}}{r^2}(-1)^m G^{1,1,2}_{m,-m,0} r^2 \psi^2_{211} && (2.17b)
\end{aligned}
$$

but $G^{0,0,0}_{0,0,0} = \frac{1}{\sqrt{4\pi}}$, $(-1)^m G^{1,1,0}_{m,-m,0} = \frac{1}{\sqrt{4\pi}}$ for $m = 0, \pm 1$ and

$$
(-1)^m G^{1,1,2}_{m,-m,0} = \begin{cases} \frac{1}{\sqrt{5\pi}}, & \text{for m} = 0 \\ -\frac{1}{2\sqrt{5\pi}}, & \text{for m} = \pm 1 \end{cases}
$$

Thus the system (2.17) becomes

$$
\begin{aligned}
\nabla^2_{r_0} V_{00}(r) &= \psi^2_{100} + r^2 \psi^2_{21m}, \\
\nabla^2_{r_2} V_{20}(r) &= C\psi^2_{21m},
\end{aligned} \tag{2.18}
$$

where the constant

$$
C = \begin{cases} \frac{2}{\sqrt{5}}, & \text{for m} = 0 \\ -\frac{1}{\sqrt{5}}, & \text{for m} = \pm 1 \end{cases} \tag{2.19}
$$

The Schrödinger equations for states ψ_{100} and ψ_{21m} are found from Equation (2.15b):

$$
\begin{aligned}
\nabla^2_{r_l}\psi_{100}(r) &= 2\left(\sqrt{4\pi}\sum_{l_1} G^{l_1,0,0}_{0,0,0} r^{l_1} V_{l_1 0} - E_{100}\right)\psi_{100} \\
\nabla^2_{r_l}\psi_{21m}(r) &= 2\left(\sqrt{4\pi}\sum_{l_1} G^{l_1,1,1}_{0,m,m} r^{l_1} V_{l_1 0} - E_{21m}\right)\psi_{21m}
\end{aligned}
$$

in the first equation condition (2.12a) tells $l_1 = 0$, and in the second equation condition (2.12a) tells $l_1 = 0, 1, 2$ but condition (2.12c) restrict to the values $l_1 = 0, 2$ thus:

$$
\begin{aligned}
\nabla^2_{r_l}\psi_{100}(r) &= 2\left(\sqrt{4\pi} G^{0,0,0}_{0,0,0} r^0 V_{00} - E_{100}\right)\psi_{100} \\
\nabla^2_{r_l}\psi_{21m}(r) &= 2\left(\sqrt{4\pi}\left(G^{0,1,1}_{0,m,m} r^0 V_{00} + G^{2,1,1}_{0,m,m} r^2 V_{20}\right) - E_{21m}\right)\psi_{21m}
\end{aligned}
$$

but $G^{0,0,0}_{0,0,0} = G^{0,1,1}_{0,m,m} = \frac{1}{\sqrt{4\pi}}$, and

$$
G^{2,1,1}_{0,m,m} = \begin{cases} \frac{1}{\sqrt{5\pi}}, & \text{for m} = 0 \\ -\frac{1}{2\sqrt{5\pi}}, & \text{for m} = \pm 1 \end{cases}
$$

so finally the system becomes

$$
\begin{aligned}
\nabla^2_{r_0}\psi_{100}(r) &= 2(V_{00} - E_{100})\psi_{100}, \\
\nabla^2_{r_1}\psi_{21m}(r) &= 2(V_{00} + Cr^2 V_{20} - E_{21m})\psi_{21m}
\end{aligned} \tag{2.20}
$$

where C is the same constant that appears in equation (2.19).

Final boson star-like system

In summary, the equations of motion for the multiSFDM case (100, 21m) are (2.18) and (2.20):

$$
\begin{aligned}
\nabla^2_{r0}\psi_{100}(r) &= 2(V_{00} - E_{100})\psi_{100}, \\
\nabla^2_{r_1}\psi_{21m}(r) &= 2(V_{00} + Cr^2 V_{20} - E_{21m})\psi_{21m}, \\
\nabla^2_{r0}V_{00}(r) &= \psi^2_{100} + r^2\psi^2_{21m}, \\
\nabla^2_{r_2}V_{20}(r) &= C\psi^2_{21m},
\end{aligned} \tag{2.21}
$$

where the constant

$$
C = \begin{cases} \frac{2}{\sqrt{5}}, & \text{for m} = 0 \\ -\frac{1}{\sqrt{5}}, & \text{for m} = \pm 1. \end{cases}
$$

To solve this system of four second-order ordinary differential equations, the auxiliary functions P_0, P_2, F_1 and F_2 have to be introduced to reduce the order of the equations. The system (2.21) becomes a set of eight first-order ordinary differential equations

$$\frac{d\psi_{100}}{dr} = F_1, \tag{2.22a}$$

$$\frac{dF_1}{dr} = 2(V_{00} - E_{100})r^2\psi_{100}, \tag{2.22b}$$

$$\frac{d\psi_{21m}}{dr} = F_2, \tag{2.22c}$$

$$\frac{dF_2}{dr} = -\frac{4}{r}F_2 + 2(V_{00} + Cr^2V_{20} - E_{21m})\psi_{21m}, \tag{2.22d}$$

$$\frac{dV_{00}}{dr} = \frac{P_0}{r^2}, \tag{2.22e}$$

$$\frac{dP_0}{dr} = r^2\psi^2_{100} + r^4\psi^2_{21m}, \tag{2.22f}$$

$$\frac{dV_{20}}{dr} = P_2, \tag{2.22g}$$

$$\frac{dP_2}{dr} = -\frac{6}{r}P_2 + C\psi^2_{21m}. \tag{2.22h}$$

The system (2.22) with the following boundary conditions

$$
\begin{aligned}
\psi_{100}(r_f) = 0, &\qquad \left.\frac{d\psi_{100}}{dr}\right|_{r=0} = 0, \\
\psi_{21m}(r_f) = 0, &\qquad \left.\frac{d\psi_{21m}}{dr}\right|_{r=0} = 0, \\
V_{00}(r_f) = -\frac{N_T}{r_f}, &\qquad P_0(r_f) = N_T, \\
V_{20}(r_f) = 0, &\qquad P_2(0) = 0,
\end{aligned}
$$

becomes a boundary value problem that is solved using the shooting method. Here N_T is the total mass enclosed by the boundary radius $r = r_f$, $N_T = N(r_f)$.

The boundary conditions on ψ_{100} and ψ_{21m} mean that the system is isolated and the conditions on their derivatives allow regularity at the origin. The boundary condition on V_{00} recovers the Keplerian fall of the potential, the boundary condition on V_{20} means that at large distances, the mass density would look spherically symmetric hence the non-spherically symmetric part of the potential should be vanished. From equation (2.22f) one can see that $P_0(r)$ is actually the enclosed mass $N(r)$ so the boundary condition in P_0 ensure us a finite mass of the halo.

To solve the equations, the central value $\psi_{100}(0) = 1$ is fixed to find the eigen-values E_{100} and E_{21m} and the initial values $V_{00}(0), V_{20}(0), \psi_{21m}(0)$ of the bound multiSFDM configuration.

The system is solved in a fixed range of $r \in (0, r_f)$ and the boundary value N_T is varied to find a family of solutions.

The circular velocity v_h of a particle due to the potential V in terms of the auxiliary functions and the radial functions in the expansion of the potential is given by

$$v_h^2 = \frac{P_0}{r} - \frac{r^2}{C}\left(rP_2 + 2V_{20}\right), \tag{2.23}$$

this expression will be usefull to fit rotation curves of galaxies in Chapter 4.

2.2.1 multiSFDM case (100, 210)

The first possibility for the multiSFDM case (Ψ_{100}, Ψ_{21m}) is the configuration with $m = 0$.

In Table 2.1 the different quantities that characterize each of the solutions of the family are shown: the total mass of the configuration N_T (that is used as the solution identifier within the family); the energy eigen-values of the ground state E_{100} and the excited state E_{210}; the total energy of the configuration $E_T = (E_{100}N_{100} + E_{210}N_{210})/N_T$; and the mass ratio $\eta = N_{210}(r_f)/N_{100}(r_f)$ and amplitude ratio $\zeta = \psi_{100}(0)/\psi_{210}(0)$ between states of the configuration.

In Figure 2.1 the functions $\psi_{100}(r), \psi_{210}(r), V_{00}(r), V_{20}(r), E_{100}, E_{210}, N(r)$, and, the total energy E_T are plotted for the family of solutions found.

In Figure 2.2 the projections in the (x, z) plane of the mass density $\rho = |\Phi_{100}|^2 + |\Phi_{210}|^2$ as function of the (x, y, z) cartesian coordinates are shown for all the solutions in the family. The figure begins in the upper left panel with the solution with $N_T = 2.0$, where the monopole term ψ_{100} dominates over the dipole term ψ_{210}, and ends in the bottom right panel with the solution with $N_T = 5.5$ where the opposite happens.

2.2.2 multiSFDM case (100, 211)

The second possibility for the multiSFDM case (Ψ_{100}, Ψ_{21m}) is the configuration with $m = 1$.

Table 2.2 is the analogous of Table 2.1 but now for the solutions found in the multiSFDM case (Ψ_{100}, Ψ_{211}). In Figure 2.3 the functions $\psi_{100}(r), \psi_{211}(r), V_{00}(r), V_{20}(r), E_{100}, E_{211}, N(r)$, and, the total energy E_T are plotted for the family of solutions found. One difference with the $m = 0$ case is that the dipole contribution to the gravitational potential is now positive. In Figure 2.4 the density plots of the mass density $\rho = |\Phi_{100}|^2 + |\Phi_{211}|^2$ as function of the (x, y, z) cartesian coordinates are ploted for all the solutions in the family. The figure begins in the upper left panel with the solution with $N_T = 2.7$, where the monopole term ψ_{100} dominates over the dipole term ψ_{211}, and ends in the bottom right panel with the solution with $N_T = 4.1$ where the

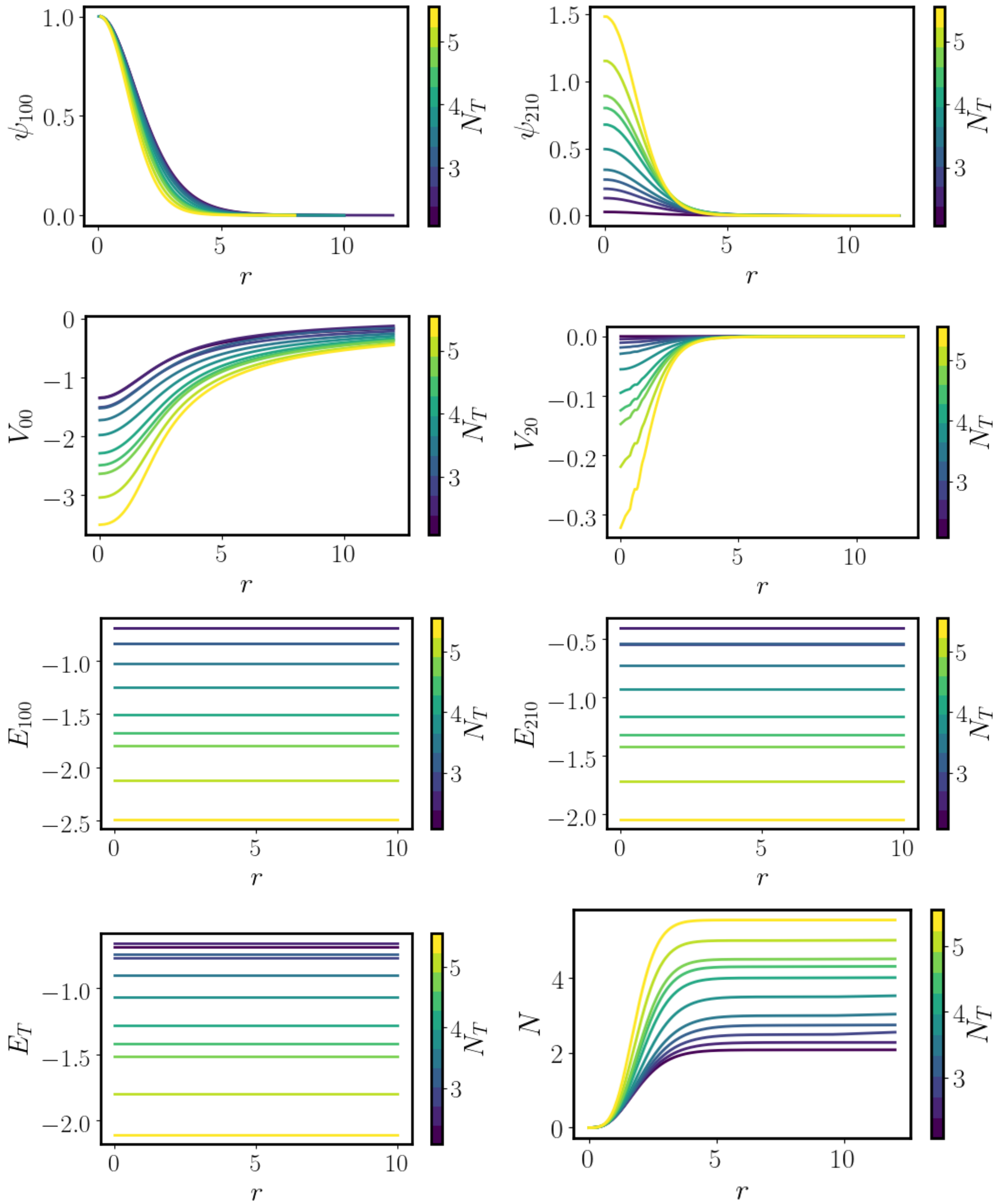

Figure 2.1 Family of solutions of the multiSFDM (Ψ_{100}, Ψ_{210}). First row: the ground state radial function ψ_{100} (left panel) and the excited state radial function ψ_{210} (right). Second row: first function V_{00} (left) and second function V_{20} (bottom panel) in the expansion of the potential V. Third row: energy eigen-values of the ground (left) and excited (right) states. Last row: total energy (left) and total enclosed mass at radius r. In color scale, the total mass N_T of each of the solutions in the family is shown.

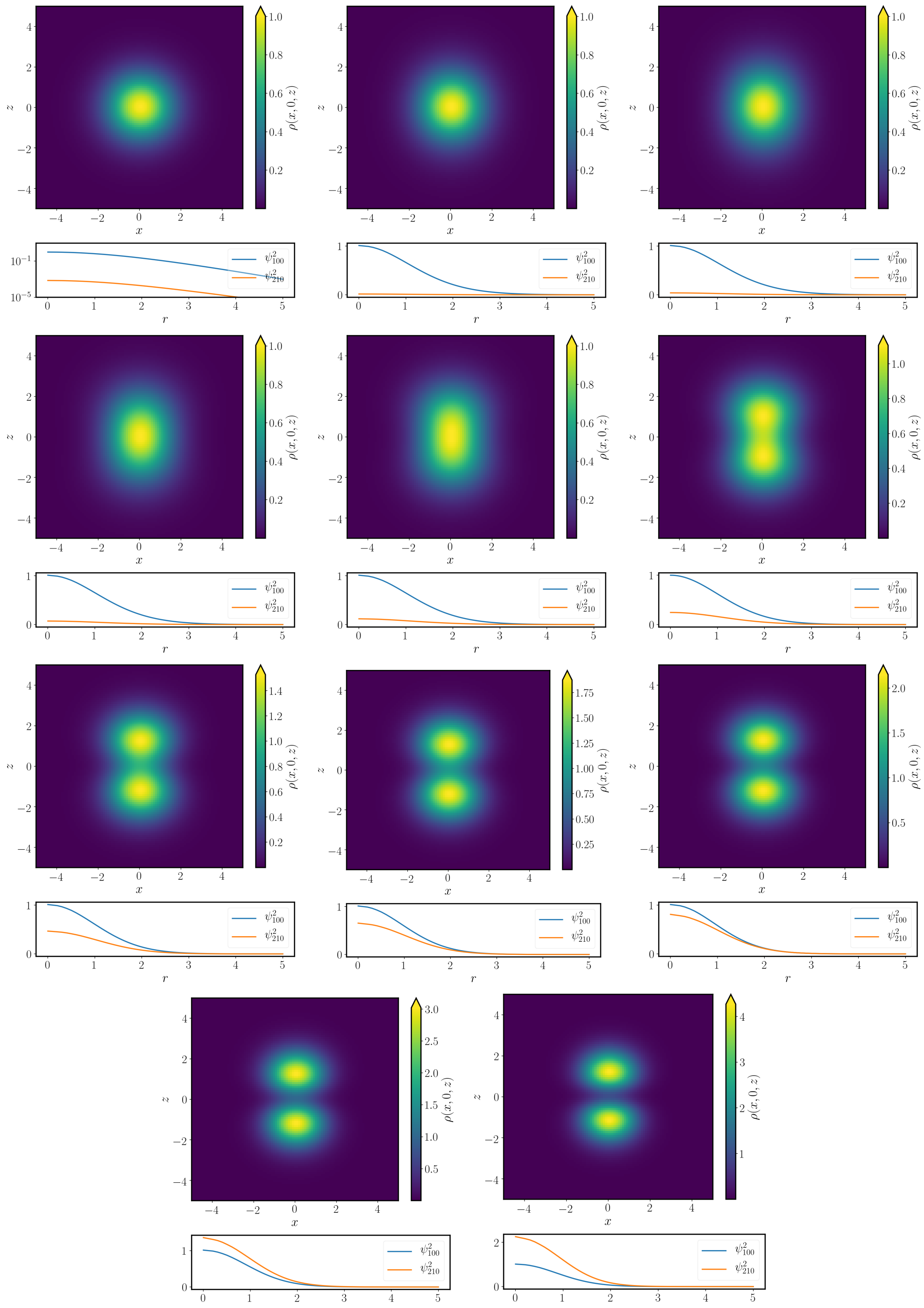

Figure 2.2 Projection in the (x, z) plane of the mass density as function of the (x, y, z) cartesian coordinates for the multiSFDM (Ψ_{100}, Ψ_{210}) family of solutions. The progression from the solution with $N_T = 2.0$ in the top left panel where the monopole term ψ_{100} dominates over the dipole term ψ_{210} to the bottom right panel the solution with $N_T = 5.5$ where the excited state ψ_{210} dominates is shown. In color scale the mass density is shown. In the bottom of each density plot, a plot of the ground state and excited state densities as function of the radial coordinate is shown.

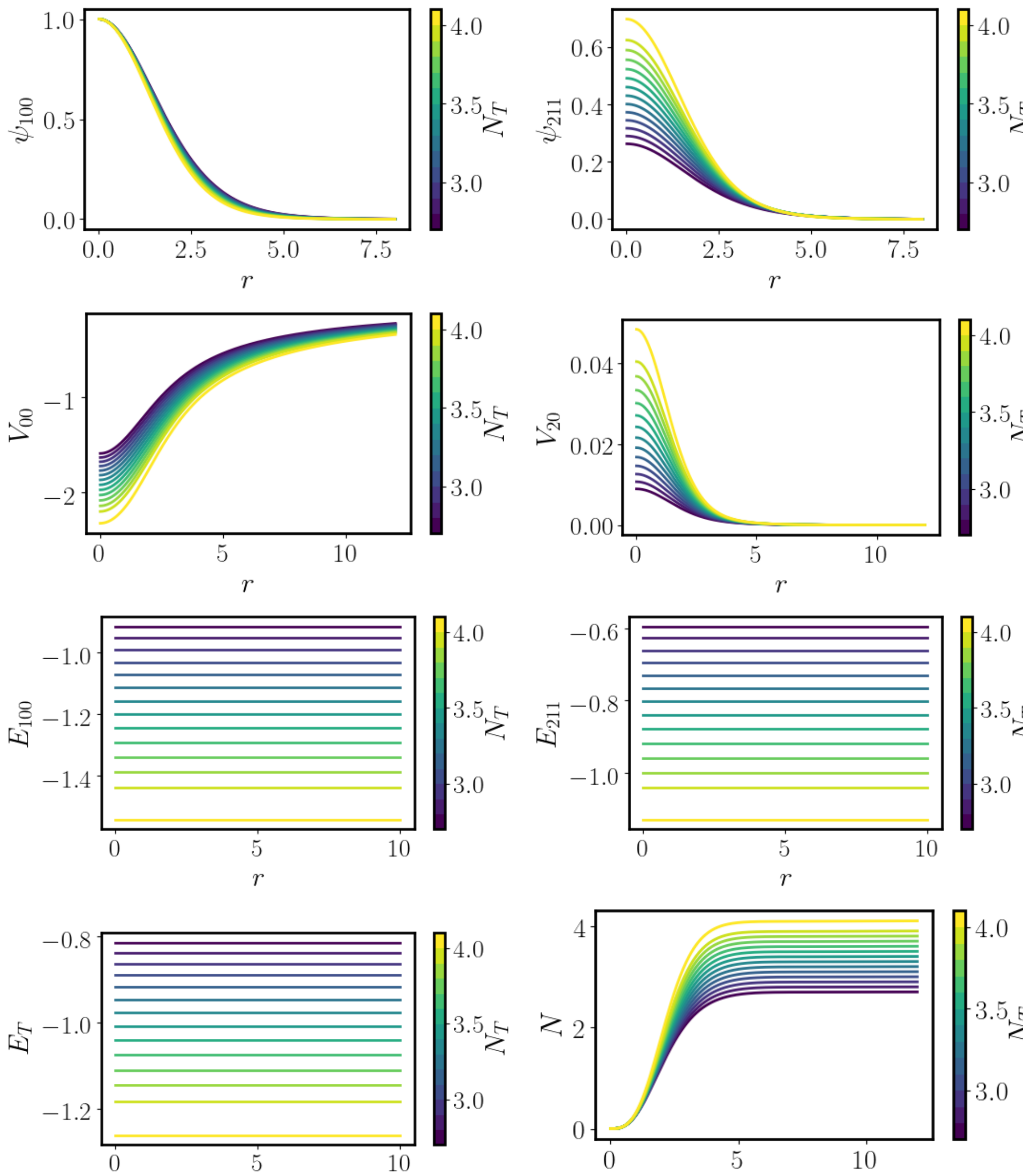

Figure 2.3 Same as in Figure 2.1 but now for the multiSFDM (Ψ_{100}, Ψ_{211}) family of solutions.

Table 2.1. multiSFDM $(100, 210)$. Total mass of the configuration (column 1), gravitational potential at the origin (2),energy eigen-values of the ground (3) and excited state (4), total energy of the configuration (5), mass ratio between states of the configuration $\eta = N_{210}(r_f)/N_{100}(r_f)$ (6) and amplitude ratio between states of the configuration $\zeta = \psi_{100}(0)/\psi_{210}(0)$ (7).

N_T (1)	$V_{00}(0)$ (2)	E_{100} (3)	E_{210} (4)	E_T (5)	η (6)	ζ (7)
2.1	-1.340	-0.691	-0.400	-0.69	0.01	37.27
2.3	-1.348	-0.692	-0.400	-0.66	0.14	7.70
2.5	-1.504	-0.839	-0.540	-0.77	0.29	5.01
2.7	-1.519	-0.843	-0.538	-0.74	0.48	3.73
3.0	-1.723	-1.032	-0.721	-0.90	0.71	2.93
3.5	-1.979	-1.251	-0.925	-1.07	1.27	2.02
4.0	-2.288	-1.511	-1.160	-1.28	1.97	1.47
4.3	-2.492	-1.679	-1.314	-1.42	2.50	1.25
4.5	-2.638	-1.798	-1.422	-1.52	2.90	1.12
5.0	-3.043	-2.125	-1.715	-1.79	4.12	0.87
5.5	-3.507	-2.488	-2.040	-2.11	5.83	0.67

opposite happens. This is an axi-symmetric configuration, the three-dimensional mass density is thus a donut-like shape given by the (211) state with a spherical shape in the center given by the (100) contribution.

The third possibility for the multiSFDM case (Ψ_{100}, Ψ_{21m}) is the configuration with $m = -1$. The equation of motion are the same as the $m = 1$ case, the only difference is the direction of the azimuthal rotation in the wave function, $\varphi \rightarrow -\varphi$ that gives no change in the mass density which is the relevant physical quantity. This case will not be considered then.

2.3 multiSFDM case (100,200)

The multiSFDM case (Ψ_{100}, Ψ_{200}) occurs when the source terms in the Poisson equation are ψ_{100} and ψ_{200}, in this case the Poisson equation (2.15a) is

$$
\begin{aligned}
\nabla^2_{r_l} V_{l0}(r) &= \frac{\sqrt{4\pi}}{r^l} \sum_{n_1,l_1,m_1} (-1)^{m_1} G^{l_1,l_1,l}_{m_1,-m_1,0} r^{2l_1} \psi^2_{n_1 l_1 m_1} \\
&= \frac{\sqrt{4\pi}}{r^l} \left((-1)^0 G^{0,0,l}_{0,0,0} r^0 \psi^2_{100} + (-1)^0 G^{0,0,l}_{0,0,0} r^0 \psi^2_{200} \right) \\
&= \frac{\sqrt{4\pi}}{r^l} G^{0,0,l}_{0,0,0} \left(\psi^2_{100} + \psi^2_{200} \right)
\end{aligned}
$$

Table 2.2. multiSFDM $(100, 211)$. Total mass of the configuration (column 1), gravitational potential at the origin (2), energy eigen-values of the ground (3) and excited state (4), total energy of the configuration (5), mass ratio between states of the configuration $\eta = N_{210}(r_f)/N_{100}(r_f)$ (6) and amplitude ratio between states of the configuration $\zeta = \psi_{100}(0)/\psi_{210}(0)$ (7).

N_T (1)	$V_{00}(0)$ (2)	E_{100} (3)	E_{210} (4)	E_T (5)	η (6)	ζ (7)
2.70	-1.590	-0.914	-0.594	-0.81	0.46	3.81
2.80	-1.632	-0.952	-0.627	-0.84	0.54	3.46
2.90	-1.677	-0.991	-0.661	-0.86	0.63	3.16
3.00	-1.722	-1.031	-0.695	-0.89	0.72	2.91
3.10	-1.769	-1.071	-0.730	-0.92	0.82	2.69
3.20	-1.817	-1.113	-0.766	-0.95	0.92	2.50
3.30	-1.867	-1.156	-0.802	-0.98	1.03	2.33
3.40	-1.919	-1.200	-0.840	-1.01	1.14	2.17
3.50	-1.971	-1.246	-0.878	-1.04	1.25	2.04
3.60	-2.026	-1.292	-0.918	-1.08	1.38	1.91
3.70	-2.082	-1.339	-0.958	-1.11	1.51	1.80
3.80	-2.139	-1.388	-0.999	-1.15	1.64	1.70
3.90	-2.199	-1.438	-1.041	-1.18	1.78	1.60
4.10	-2.322	-1.542	-1.128	-1.26	2.09	1.43

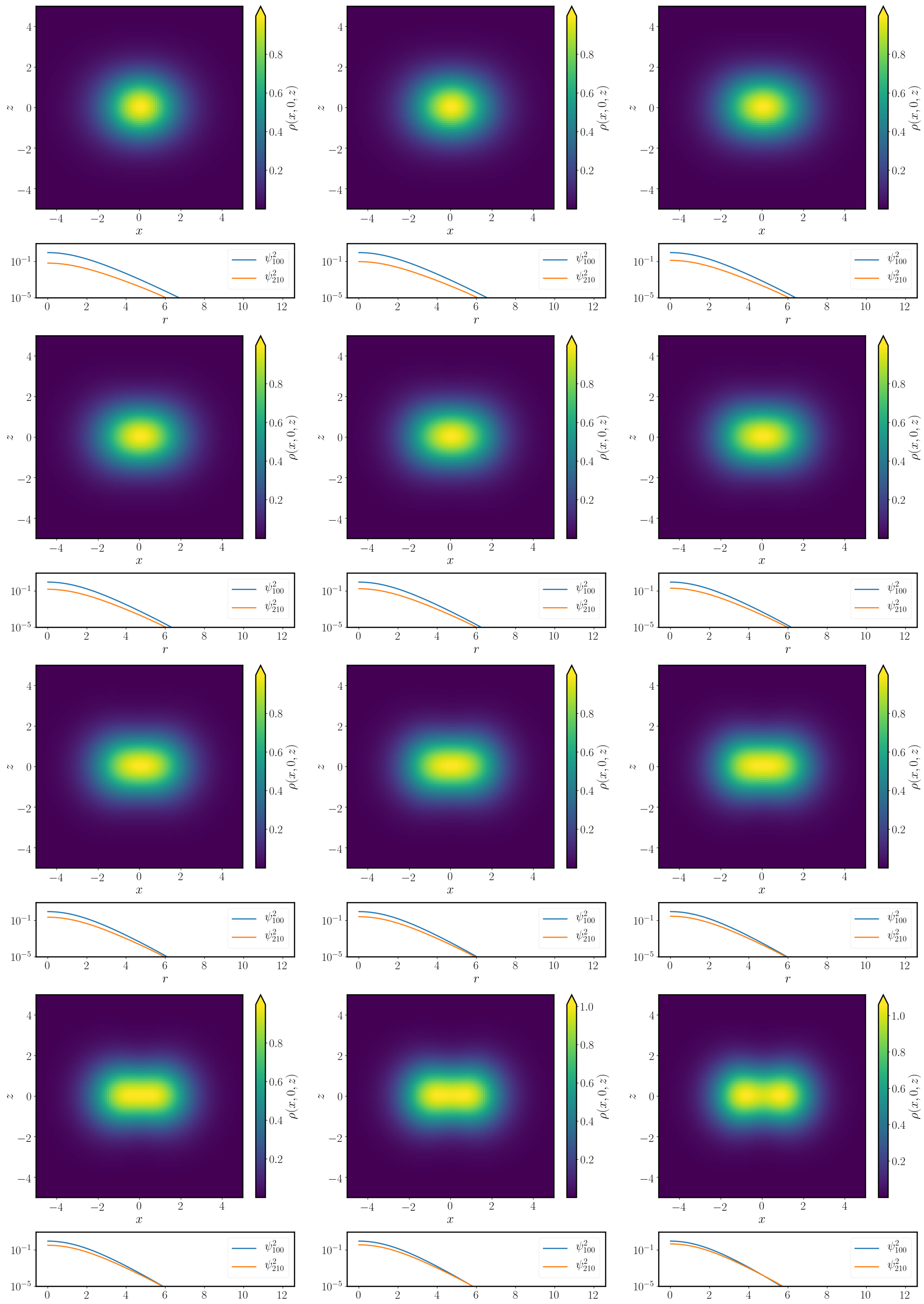

Figure 2.4 Projection in the (x, z) plane of the mass density as function of the (x, y, z) cartesian coordinates for the multiSFDM (Ψ_{100}, Ψ_{211}) family of solutions. The progression from the solution with $N_T = 2.7$ in the top left panel where the monopole term ψ_{100} dominates over the dipole term ψ_{211} to the bottom right panel the solution with $N_T = 4.1$ where the excited state ψ_{211} dominates is shown. In color scale the mass density is shown. In the bottom of each density plot, a plot of the ground state and excited state densities as function of the radial coordinate is shown.

because of condition (2.12a) l can only take the value zero, the only non-zero Gaunt coefficient is $G^{0,0,0}_{0,0,0} = 1/\sqrt{4\pi}$. The only term in the potential expansion will be the monopole term, a spherically symmetric potential, the Poisson equation reduces to

$$\nabla^2_{r_0} V_{00}(r) = \psi^2_{100} + \psi^2_{200}.$$

The Schrödinger equations (2.15b) for the ground and excited states are

$$\begin{aligned}
\nabla^2_{r_0}\psi_{100}(r) &= 2\left(\sqrt{4\pi}\sum_{l_1} G^{l_1,0,0}_{0,0,0} r^{l_1} V_{l_1 0} - E_{100}\right)\psi_{100}, \\
\nabla^2_{r_0}\psi_{200}(r) &= 2\left(\sqrt{4\pi}\sum_{l_1} G^{l_1,0,0}_{0,0,0} r^{l_1} V_{l_1 0} - E_{200}\right)\psi_{200}.
\end{aligned}$$

again, condition (2.12a) tells that l_1 can only take the value $l_1 = 0$. The Schrödinger equations finally become

$$\begin{aligned}
\nabla^2_{r_0}\psi_{100}(r) = 2(V_{00} - E_{100})\psi_{100}, \\
\nabla^2_{r_0}\psi_{200}(r) = 2(V_{00} - E_{200})\psi_{200}.
\end{aligned}$$

The general system (2.15) thus reduces to the spherically symmetric case in Matos and Ureña López [2007], Ureña López and Bernal [2010] where they first propose the spherically symmetric multistates:

$$\begin{aligned}
\nabla^2_{r_0}\psi_{100}(r) = 2(V_{00} - E_{100})\psi_{100}, \\
\nabla^2_{r_0}\psi_{200}(r) = 2(V_{00} - E_{200})\psi_{200}, \\
\nabla^2_{r_0} V_{00}(r) = \psi^2_{100} + \psi^2_{200},
\end{aligned}$$

where the gravitational potential is simply

$$V(r,\theta) = \sqrt{4\pi} V_{00}(r) Y_{00}(\theta,\phi) = V_{00}(r)$$

and the circular velocity

$$v^2_h = \frac{P_0}{r}. \tag{2.24}$$

In Ureña López and Bernal [2010], these multistate configurations were shown to be stable only when $N_{200}(r_f)/N_{100}(r_f) < 1.1$ so only with this kind of solutions are considered here. Once again the total mass N_T is used as a solution identifier within the family. In Table 2.3 the energy eigen-values, the total energy, and the mass and amplitude ratios for each solution in the family are written.

Table 2.3: Same as in Table 2.1 but now using state ψ_{200}.

N_T (1)	$V_{00}(0)$ (2)	E_{100} (3)	E_{200} (4)	E_T (5)	η (6)	ζ (7)
2.18	-1.392	-0.737	-0.337	-0.71	0.07	6.00
2.30	-1.408	-0.745	-0.341	-0.70	0.14	4.11
2.40	-1.436	-0.766	-0.359	-0.70	0.20	3.37
2.50	-1.465	-0.788	-0.377	-0.70	0.27	2.90
2.60	-1.496	-0.811	-0.395	-0.71	0.34	2.56
2.66	-1.520	-0.830	-0.412	-0.72	0.38	2.41
2.70	-1.527	-0.834	-0.414	-0.71	0.41	2.31
2.75	-1.538	-0.840	-0.418	-0.71	0.45	2.20
2.94	-1.631	-0.917	-0.486	-0.76	0.59	1.89
2.97	-1.613	-0.896	-0.463	-0.73	0.62	1.84
3.10	-1.649	-0.925	-0.491	-0.75	0.71	1.75
3.30	-1.722	-0.977	-0.532	-0.77	0.88	1.54
3.50	-1.800	-1.032	-0.575	-0.80	1.07	1.37

The corresponding wave functions, potential, energy eigenvalues, total energy and enclosed mass are also plotted for the family of solutions in Figure 2.5.

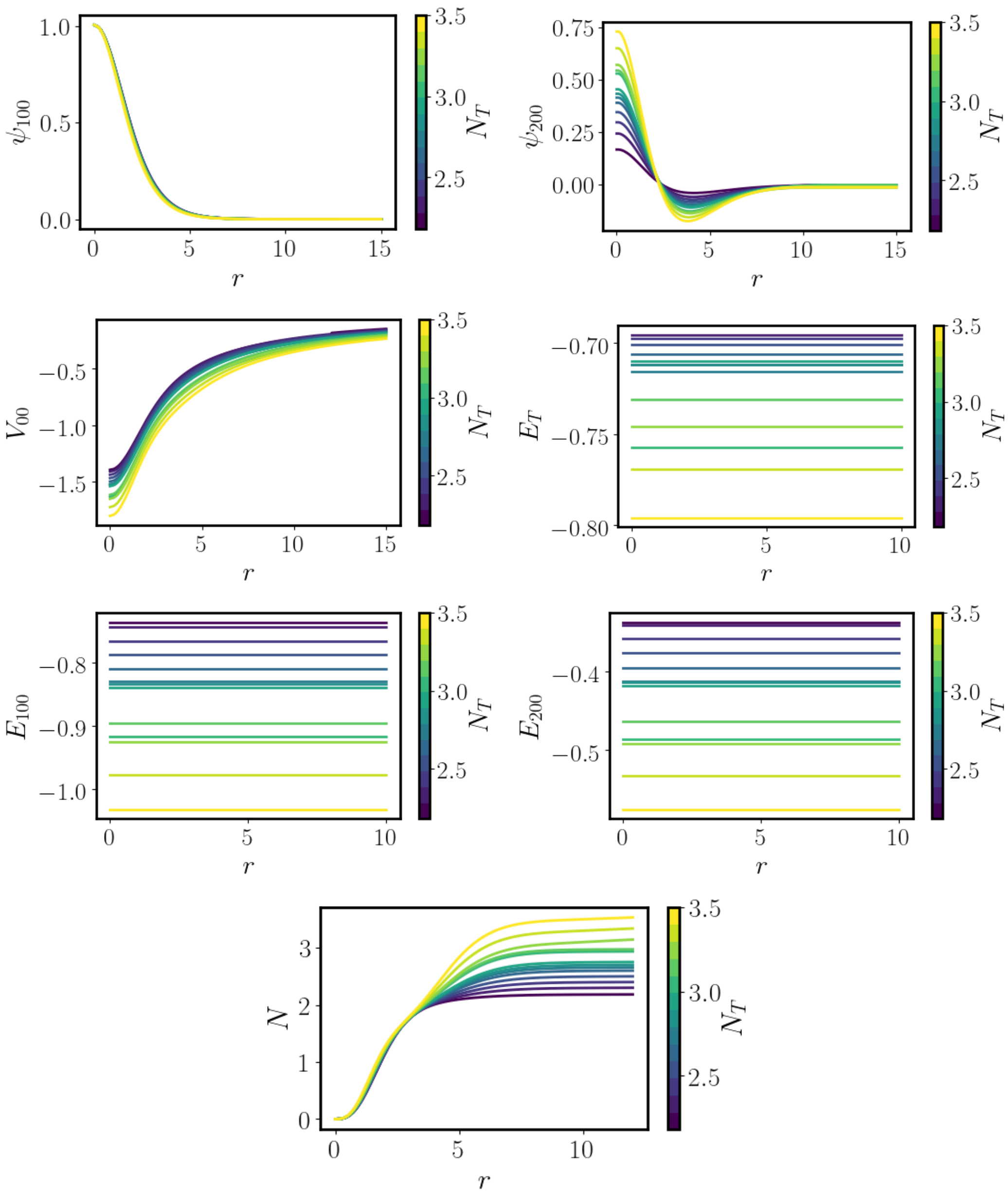

Figure 2.5 Family of solutions of the multiSFDM (Ψ_{100}, Ψ_{200}). First row: The wave function of the ground state ψ_{100} (left panel), and the excited state ψ_{200} (right). Second row: the potential V (left) and the total energy of the configuration (right). Third row: the energy eigen-values of the ground (left) and excited (right) states. Bottom row: the enclosed mass as function of the radius. In color scale, the total mass N_T of each of the solutions in the family is shown.

Chapter 3

Satellites

3.1 Model

To explain the anisotropic distribution of satellites observed in the Milky Way , M31 and Cen A systems, a model with four major assumptions is proposed:

- The gravitational potential of the host galaxy is dominated by the dark matter .
- The dark matter halo will be a stationary multiSFDM configuration.
- The satellites are assumed to behave as test particles orbiting around the halo.
- The non-relativistic and weak field regimes hold, which is valid at galactic scales.

Under these conditions the resulting scalar field is the order parameter of the Gross-Pitaevskii-Poisson system (2.1), that rules the dynamics of a condensate of bosons in coherent states Ψ_{nlm} [Guzmán and Ureña López, 2020].

For the dark matter halo, solutions with the spherical Ψ_{100} and first dipolar Ψ_{210} contributions will be considered, the multiSFDM (Ψ_{100}, Ψ_{210}) configuration. This configuration is only chosen for three reasons: first, that this is the simplest non-spherically symmetric multistate configuration after the spherical (Ψ_{100}, Ψ_{200}) equilibrium configuration, second, the resulting two blobs associated to the dipolar (210)-mode are expected to pull test particles toward the poles to broke the isotropy, and third, in Guzmán and Ureña López [2020] a possible mechanism for the formation of such structures has been envisioned.

In Chapter 2 a full family of solutions in the multiSFDM (Ψ_{100}, Ψ_{210}) configuration was found, nevertheless, in this chapter only two solutions are going to be considered and used as workhorse examples. The first one (that from now on will be called **dipole**-dominated) where the dipolar contribution is larger than the monopole contribution, such that the mass ratio between the spherical and dipolar masses is $\eta = 0.36$ and it has energy eigenvalues $E_{100} = 1.8$ and $E_{210} = 1.42$. In the second one, the opposite happens, the spherical ground state contribution is larger than the dipolar with a mass ratio $\eta = 3$, from now on this configuration will be called **monopole**-dominated and has energy eigenvalues $E_{100} = 0.84$ and $E_{210} = 0.54$. A projection in the xz plane of the mass density $\rho(x, y, z)$ of both configurations is shown in Figure 3.1, in dimensionless and scale-free quantities. A projection along the $z-$axis of the individual contribution to the mass density of each state in the configuration is showed

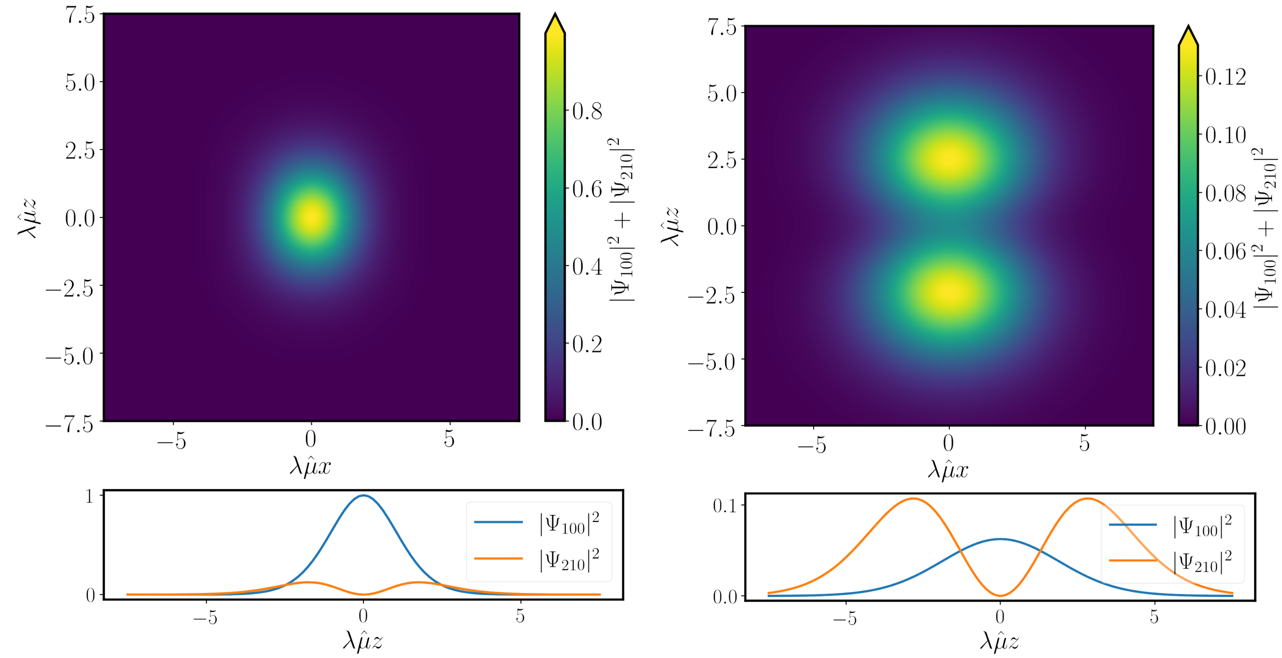

Figure 3.1 Mass density $\rho(x, y, z) = |\Psi_{100}|^2 + |\Psi_{210}|^2$ of both multiSFDM (Ψ_{100}, Ψ_{210}) configurations used in this Chapter. In the left panel, the **monopole**-dominated configuration with mass ratio between states $\eta = 3$ is shown. In the right panel, the **dipole**-dominated configuration in which the mass ratio between the spherical and dipolar contributions is $\eta = 0.36$ is shown. At the top of each panel a density plot of the projection on the $xz-$plane of the mass density is shown in dimensionless units, whereas at the bottom the projection along the $z-$axis of the individual contributions to the mass density of each state in the multiSFDM configuration: $|\Psi_{100}|^2$ and $|\Psi_{210}|^2$ are shown.

to note that although in the 2D density plot it appears that only the dominant mutipole is plotted, the nondominant contribution is present. In Figure 3.2 the 3D density plot of the **monopole**-dominated configuration mass density is plotted, the individual contributions to the mass density of the ground and excited states ($|\Psi_{100}|^2$ and $|\Psi_{210}|^2$) are plotted too. The main difference between both is the notorious presence of the dipole blobs in the **dipole**-dominated configuration.

The gravitational potential $V(\rho, z)$ due to both multiSFDM (Ψ_{100}, Ψ_{210}) configurations is plotted in Figure 3.3, figure shows a density plot of the projection on the ρz-plane of the potential and the projection along the ρ-axis for fixed values of the z coordinate, namely $z = 0, 2.5$, in this projections two things can be noted: for the **monopole**-dominated configuration the potential wells produced by the dipole contribution (located at $z \approx 2.5$) are half deep than the produced by the monopole configuration, whereas in the **dipole**-dominated case they are almost equally deep.

Using the scaling property written in relation (2.7), appropriate galactic size scales are obtained assuming a particle mass of $\mu = 10^{-25}\text{eV}/c^2$, corresponding to $\hat{\mu} = 15.65/\text{kpc}$, and a scaling parameter $\lambda \simeq 10^{-3}$. For example, from equation (2.8), the halo mass scale is $M_C = 10^{12} M_\odot$. From hereafter, the latter will be the fiducial values for the physical examples studied

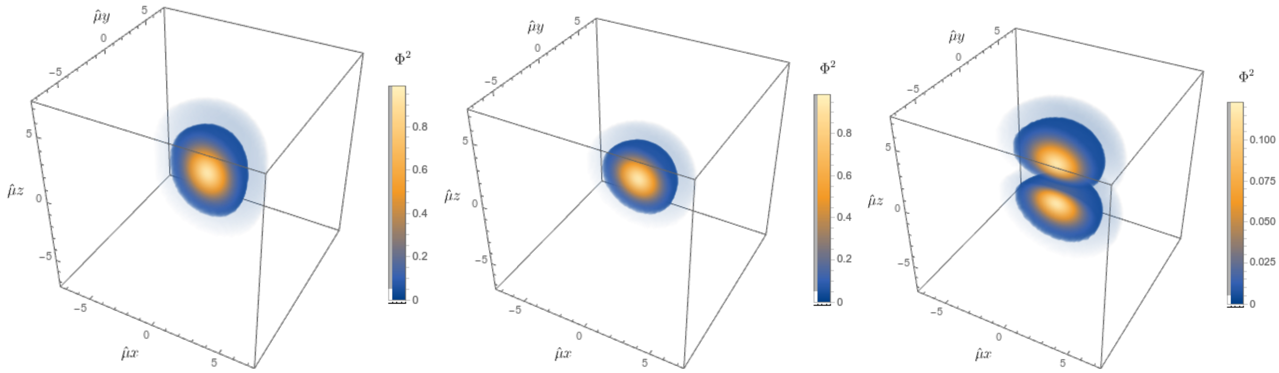

Figure 3.2 Three-dimensional density plot of the mass density $\rho(x, y, z) = |\Psi_{100}|^2 + |\Psi_{210}|^2$ of the multiSFDM (Ψ_{100}, Ψ_{210}) **monopole**-dominated configuration. In the left panel the total mass density is plotted. In the middle (right) panel, the individual contribution to the mass density of the ground (excited) state $|\Psi_{100}|^2$ ($|\Psi_{210}|^2$) is plotted. The $y < 0$ part of the density is not showed for a better appreciation of the inner part.

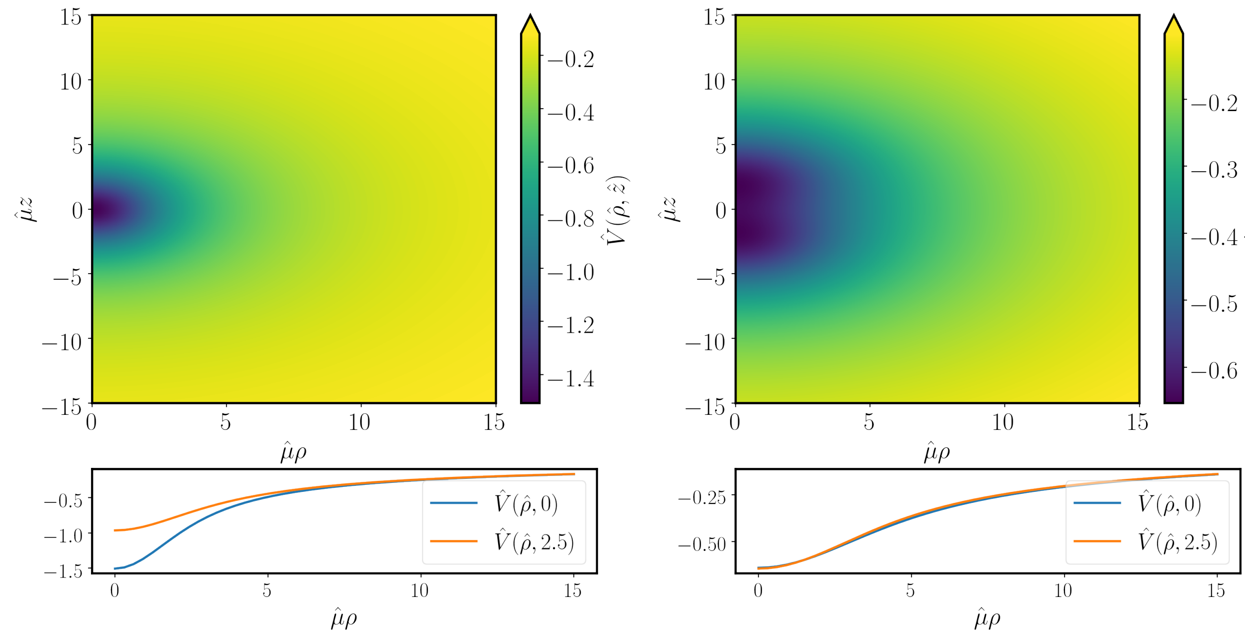

Figure 3.3 Gravitational potential $V(\rho, z)$ due to both multiSFDM (Ψ_{100}, Ψ_{210}) configurations used in this Chapter. In the left panel, the potential due to the **monopole**-dominated configuration with mass ratio between states $\eta = 3$ is shown. In the right panel, the potential due to the **dipole**-dominated configuration in which the mass ratio between the spherical and dipolar contributions is $\eta = 0.36$ is shown. At the top of each panel a density plot of the projection on the ρz-plane of the potential in dimensionless units is shown, whereas at the bottom the projection along the ρ-axis of the potential is shown for fixed values of the z coordinate, namely $z = 0, 2.5$.

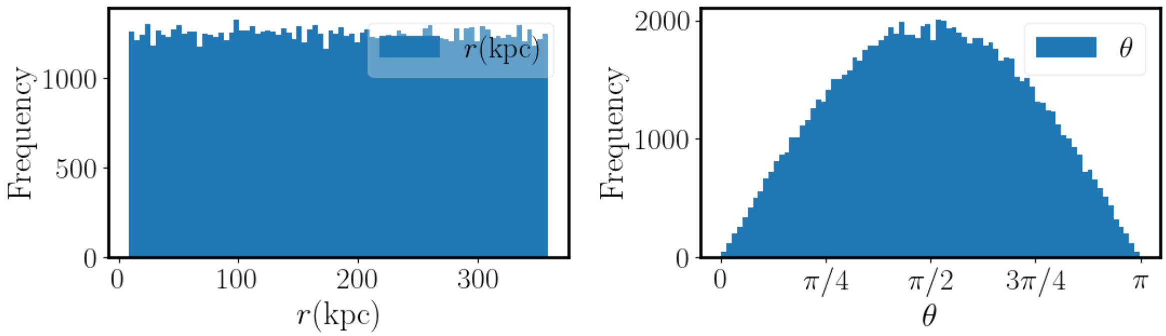

Figure 3.4 Histograms of the initial distribution of the 10^5 test particles in fiducial ($\mu = 10^{-25}\mathrm{eV}/c^2$) units. In the left panel the uniform distribution in the radial r coordinate, and in the right panel the distribution of the polar θ coordinate that allows a uniform distribution of particles over the sphere.

below.

3.2 Analysis of test particle trajectories

Now the motion of test particles within the gravitational potential $V(\mathbf{x})$ of equation (2.1) will be studied. The Lagrangian per unit mass of a particle under an axi-symmetric potential $V(r,\theta)$ is

$$\mathcal{L} = \frac{1}{2}(\dot{r}^2 + r^2 \sin^2\theta\dot{\phi}^2 + r^2\dot{\theta}^2) - V(r,\theta)$$

the Euler-Lagrange equations are then

$$\begin{aligned} \ddot{r} &= r\dot{\theta}^2 - \frac{\partial V_{eff}}{\partial r} \\ \frac{d}{dt}\left(r^2\dot{\theta}\right) &= -\frac{\partial V_{eff}}{\partial \theta} \end{aligned}$$

where the effective potential

$$V_{eff} = \frac{L^2}{2r^2\sin^2\theta} + V(r,\theta)$$

where L is the angular momentum per unit mass.

The trajectories of 10^5 test particles with initial positions randomly chosen from an uniform distribution over the radius interval $(0, R = 4]$ are integrated, in Figure 3.4 histograms showing the initial uniform distribution of particles at radial position and the distribution of particles in the polar θ coordinate that allows a uniform distribution of particles over the sphere are plotted. In the left panel of Figure 3.5, the 3D initial positions of the test particles are plotted in cartesian coordinates (x, y, z).

The initial speed of the particles is also randomly chosen from a uniform distribution over the interval $(0, v_{\max} = av_{\mathrm{esc}}]$, where v_{esc} is the escape velocity of a particle at radius $R = 4$.

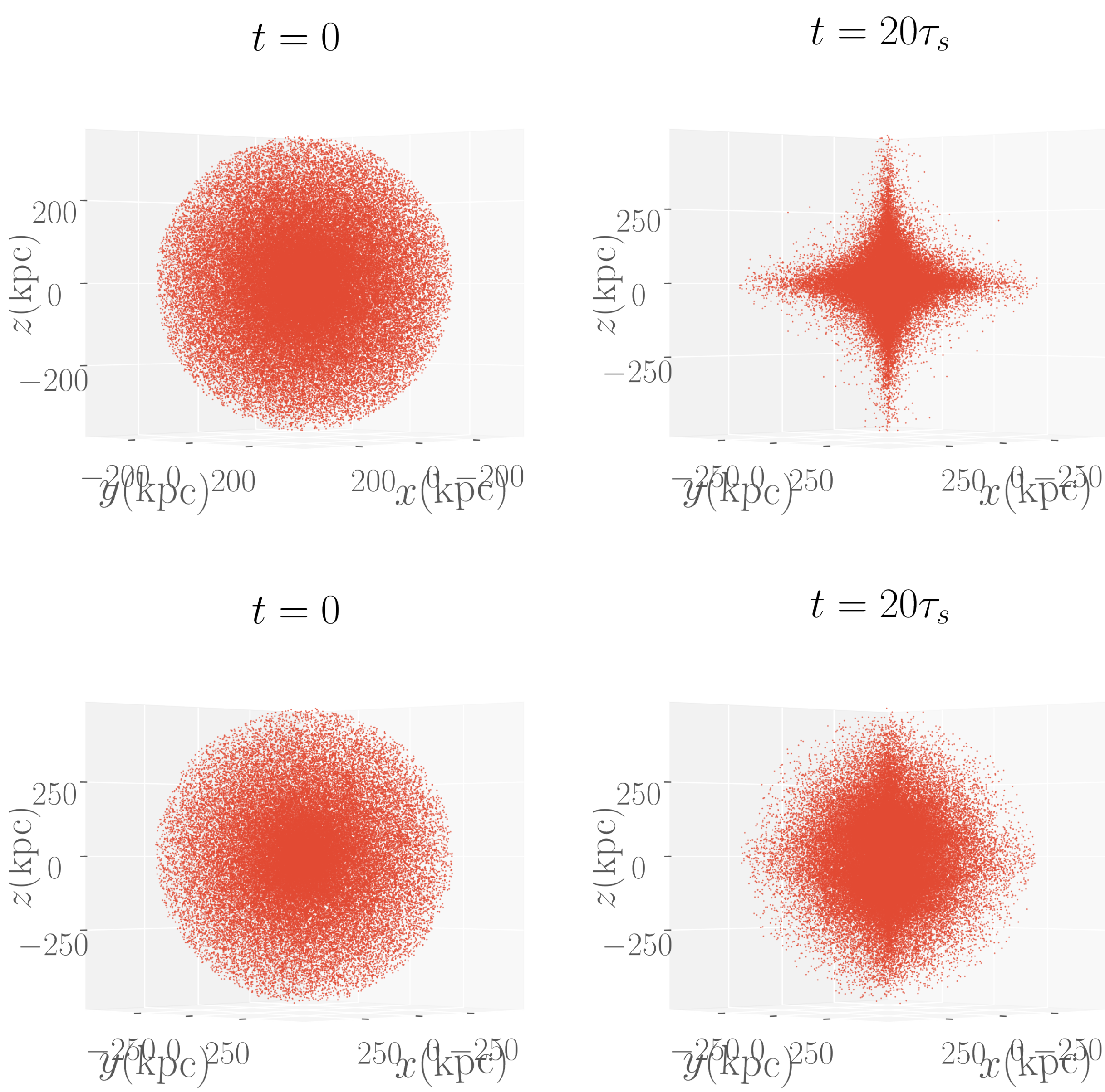

Figure 3.5 Spatial distribution of 10^5 test particles in cartesian (x, y, z) galactocentric coordinates at initial time (left panel), and after $20\tau_s$ (right panel). At the top the position of test particles for the **monopole**-dominated configuration with $\eta = 3$ is shown. At the bottom the position particles for the dipolar dominated case $\eta = 0.36$ is shown.

Four specific values of the fraction a of the escape velocity are used, namely $a = 1/4, 1/2, 3/4$ and 1. The direction of the initial velocities are uniformly distributed in the unit sphere.

The total time of evolution for all test particles is $20\tau_s$ where τ_s is the time scale defined as the time it takes a test particle, initially located on the equatorial plane $\theta = \pi/2$ at a distance $\lambda\hat{\mu}r = 4$ from the origin, with an initial velocity equal to a quarter its escape velocity, to complete an orbit. In physical units, this time scale takes is of the order of Giga years.

As the effective radius of dwarf Milky Way satellite galaxies is ~ 2 kpc and satellites are at distances ~ 20 kpc to 260 kpc from the galactic center, satellite galaxies can not be considered as test particles, however the motion of test particles can indicate where the non-gravitationally dominating structures under the influence of a dark matter halo potential accumulate with a certain likelihood in the asymptotic time, so the regions where the test particles accumulate the most, will also be those regions where a single particle has the bigger likelihood to reside.

3.3 Results for the $v_{\max} = v_{\text{esc}}/2$ case

3.3.1 Positions

In the right panel of Figure 3.5 the spatial distribution of particles after evolving during $20\tau_s$ are shown for the monopole and **dipole**-dominated configurations. The density blobs associated to the dipolar contribution to the density ρ_{210}, afect the initially spherically symmetric distribution of particles until at final evolution time $t = 20\tau_s$ the particles follow a full axi-symmetric distribution, the particles concentrate mainly around the equatorial plane of the configuration and along the $z-$axis.

Monopole-dominated configuration

In this configuration, after the evolution time $t = 20\tau_s$ the test particles distribute in a star-like shape at large radii (see the upper right panel of Figure 3.5), but most of them remain concentrated around the center within a sphere of radius $\lesssim 200$kpc (see the bottom left panel of Figure 3.6).

In Figure 3.6 histograms of the radial position r and polar angle θ position of all test particles at initial time (first row) and after the evolution time (second and third rows) are shown. In the histograms of the final evolution time, the test particles are filtered by distance to distinguish between those particles within a distance of the order of the galaxy size $r \in (0, 30)$kpc (second row) from those at distances corresponding to satellite galaxies distances $r \in (30, 300)$kpc (third row). In the former case, particles distribute close to isotropically at the equator $\theta = \pi/2$ (at the stellar disc plane $z = 0$). In the later case, the test particles distribute anisotropically at three preferential angles $\theta = 0, \pi/2$ and π, thus particles with random initial conditions will accumulate with bigger probability near these angles.

Dipole-dominated configuration

In this configuration, after the evolution time, although the particles distribute anisotropically, the anisotropy is not that enhanced as in the **monopole**-dominated configuration (see the bottom right panel of Figure 3.5). Figure 3.7 is the analogous of Figure 3.6, there are important

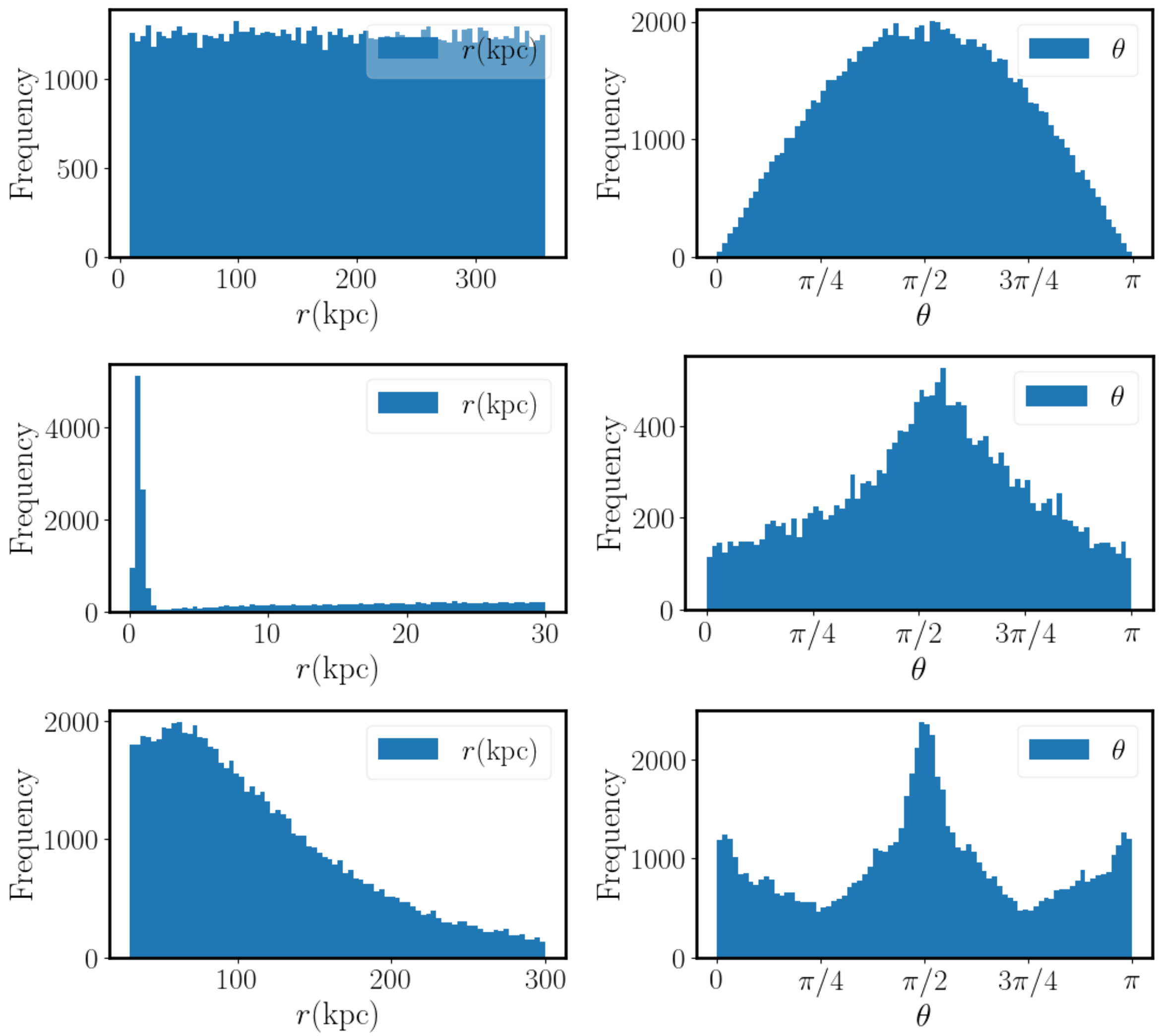

Figure 3.6 First row: Histograms of the positions (r and θ coordinates) of the 10^5 test particles at initial time for the **monopole**-dominated configuration. Second and third rows: Histograms of the positions after a $20\tau_s$ time of evolution. The data is filtered by distances, in the second row only the particles at short distances $r \in (0, 30)$kpc appear and in the third row only the particles at $r \in (30, 300)$kpc appear. All physical distances are calculated using the fiducial ($\mu = 10^{-25}$eV$/c^2$) units.

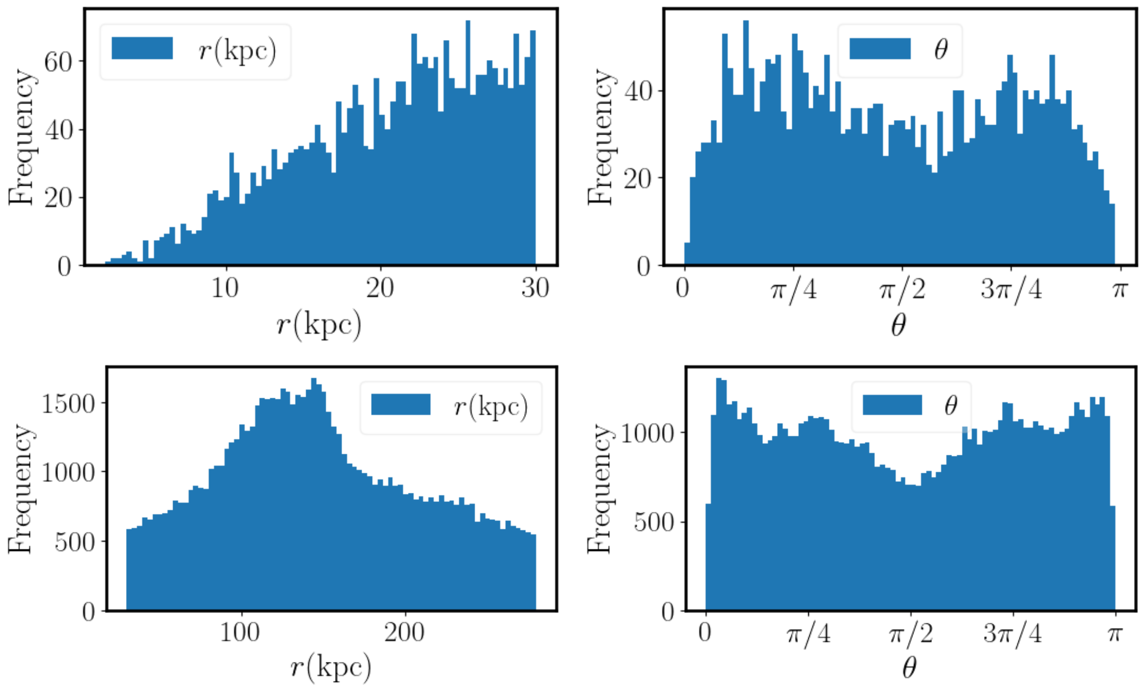

Figure 3.7 Histograms of the positions (r and θ coordinates) of the 10^5 test particles after a $20\tau_s$ time of evolution for the **dipole**-dominated configuration. The data is filtered by distances, in the first row only the particles at short distances $r \in (0, 30)$kpc appear and in the second row only the particles at $r \in (30, 280)$kpc appear.

differences in the radial distribution, in this configuration, the test particles do not accumulate near the origin because of the sub dominating monopolar contribution, and there is a peak concentration around 150 kpc due to the influence of the dominating dipolar contribution.

There are important differences in the polar angle distribution too, at small distances $r <$ 30kpc, there are now two peaks close to $\theta = \pi/4$ and $\theta = 3\pi/4$ and a decrease in the equatorial plane $\theta = \pi/2$. At large distances $(30 < r < 280)$ the peaks at $\theta = 0, \pi$ are not as sharp as in the **monopole**-dominated scenario and there is no peak in the equatorial plane.

3.3.2 Orbital poles

The direction of the angular momentum a.k.a orbital pole is defined as

$$l = \frac{\mathbf{L}}{|\mathbf{L}|} = \frac{\mathbf{x} \times \frac{d\mathbf{x}}{dt}}{\left|\mathbf{x} \times \frac{d\mathbf{x}}{dt}\right|},$$

in spherical coordinates (θ_l, ϕ_l):

$$l = \begin{bmatrix} \sin\theta_l \cos\phi_l \\ \sin\theta_l \sin\phi_l \\ \cos\theta_l \end{bmatrix}$$

As mentioned in the introduction, the orbital poles of the Milky Way classical satellites are pointing almost in the same direction, and almost parallel to the normal vector of the plane defined by its current positions (see Figure 1.10), indicating that satellites are co-rotating within that plane.

In Figures 3.8 and 3.9 the orbital poles of the test particles at distances in the range $r \in (30, 300)$ kpc at the final evolution time $t = 20\tau_s$ for both monopole and **dipole**-dominated configurations are plotted, in the upper panel the polar θ_l and azimuthal ϕ_l angles of the orbital poles are plotted, and in the bottom panel, the longitude l and latitude b of the orbital poles are plotted. The Milky Way classical satellites orbital poles calculated from the velocity measurements of Pawlowski and Kroupa [2013] are also plotted for comparison. In both cases, the orbital poles distribute around $\theta_l = \pi/2$ (or $b = 0°$), the dispersion being wider for the **dipole**-dominated configuration. The major difference is in the azimuthal angle, in the **monopole**-dominated configuration there are regions around $\phi_l = 0, \pi/2, \pi, 3\pi/2$ (or $l = 0°, 90°, 180°, 270°$) where orbital poles accumulate the most, which would in turn be more compatible with the data points of the Milky Way satellite galaxies, for which the mean direction of the seven most concentrated orbital poles points at $(l = 179.5°, b = -9°)$ Pawlowski and Kroupa [2020]. Note that these four preferential azimuthal angles in fact are only two: $\phi_l = 0, \pi/2$, because the other ones $\phi_l = \pi, 3\pi/2$ correspond to particles rotating in the opposite direction, as occurs in the Milky Way system, with Sculptor rotating in the opposite direction ($l = 0$) of the rest (Fornax, LMC, SMC, Ursa Minor Carina, Draco and Leo II) at $l = 180$.

In Figure 3.10 the time evolution of the orbital poles of all the test particles for the **monopole**-dominated configuration are shown. The figure starts in the upper left panel with a snapshot at $t = 0$ and follow with snapshots every $4\tau_s$ until $t = 20\tau_s$, the distribution of orbital poles tends to be stationary after $4\tau_s$, for this reason, a time lapse of $20\tau_s$ is considered as asymptotic time. For the **monopole**-dominated configuration $\tau_s \simeq 1.8$ Gyr, which implies that after 7.2 Gyr the orbital poles distribution would become nearly stationary.

Figure 3.11 is similar to Figure 3.10 but now the progression starts with a snapshot at $t = 0$ and follow with snapshots every $0.25\tau_s$ until $t = \tau_s$, to show now that the orbital poles start to accumulate around $\pi/2$ at earliest times.

3.4 Plane trajectories.

So far nothing has been said about the geometric properties of the test particles trajectories, in this section the torsion of the curves will be studied. If the torsion of a curve with is zero, then this curve belongs to a fixed plane. To know whether or not the trajectories become planar, the torsion at each time step t of the trajectory $\mathbf{x}(t)$ of each test particle is tracked. The torsion can be calculated as

$$\tau(t) = \frac{\left(\frac{d\mathbf{x}}{dt} \times \frac{d^2\mathbf{x}}{dt^2}\right) \cdot \frac{d^3\mathbf{x}}{dt^3}}{\left|\frac{d\mathbf{x}}{dt} \times \frac{d^2\mathbf{x}}{dt^2}\right|^2}.$$

In the top panel of Figure 3.12 the histogram of the values of τ of all test particles at initial time is plotted, and in the bottom panel the histograms of $\tau(20\tau_s)$ for the monopole and **dipole**-dominated configurations are shown. Due to the randomness of the initial conditions, the initial distribution of τ has a peak at $\tau = 0$ but there is also a considerable amount of particles with trajectories with high values of τ, however during the evolution, the torsion of all particles tends to smaller values, until a sharp peak near zero is found for both configurations.

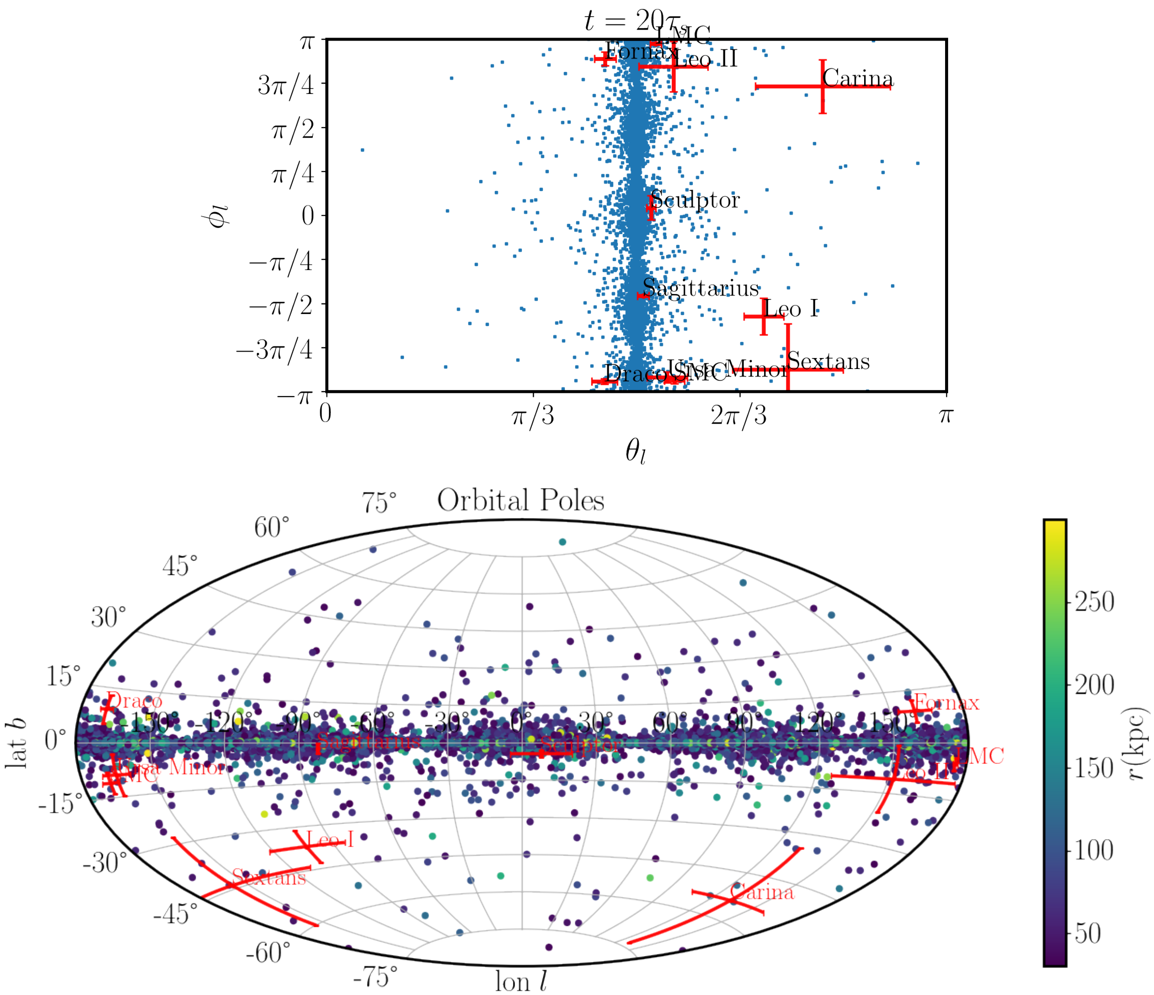

Figure 3.8 Polar angle θ_l and azimuthal angle ϕ_l (upper panel) and longitude l and latitude b (bottom panel) in galactocentric coordinates of the orbital poles (angular momentum) of the test particles that after $t = 20\tau_s$ are in a distance range $r \in (30, 300)$kpc, for the **monopole-**dominated configuration. The red markers are the orbital poles of the Milky Way classical satellites (calculated from the velocity data of Pawlowski and Kroupa [2013]). For the bottom panel, in color scale the galactocentric distance of the test particles is plotted.

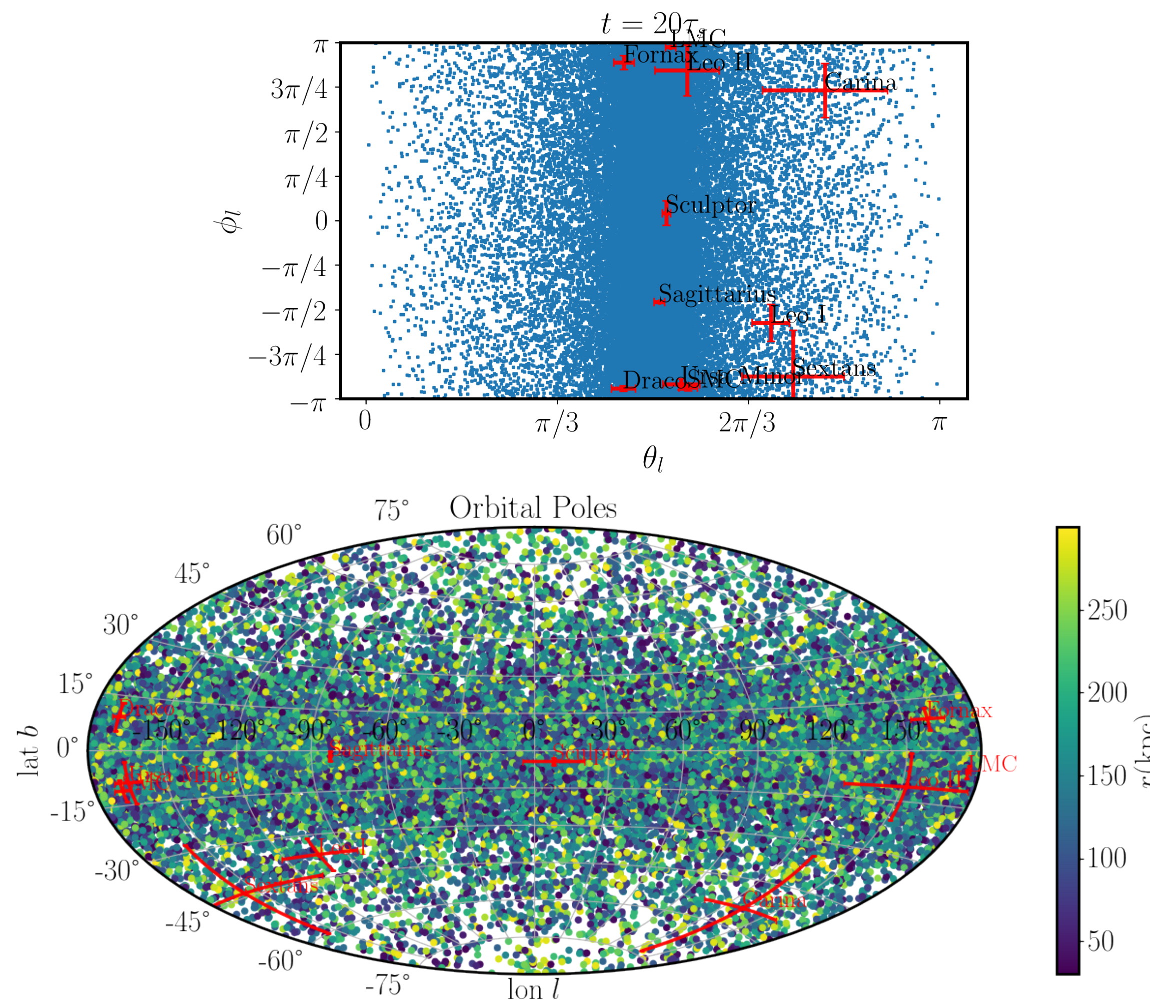

Figure 3.9 Same as in Figure 3.8 but now for the **dipole**-dominated configuration.

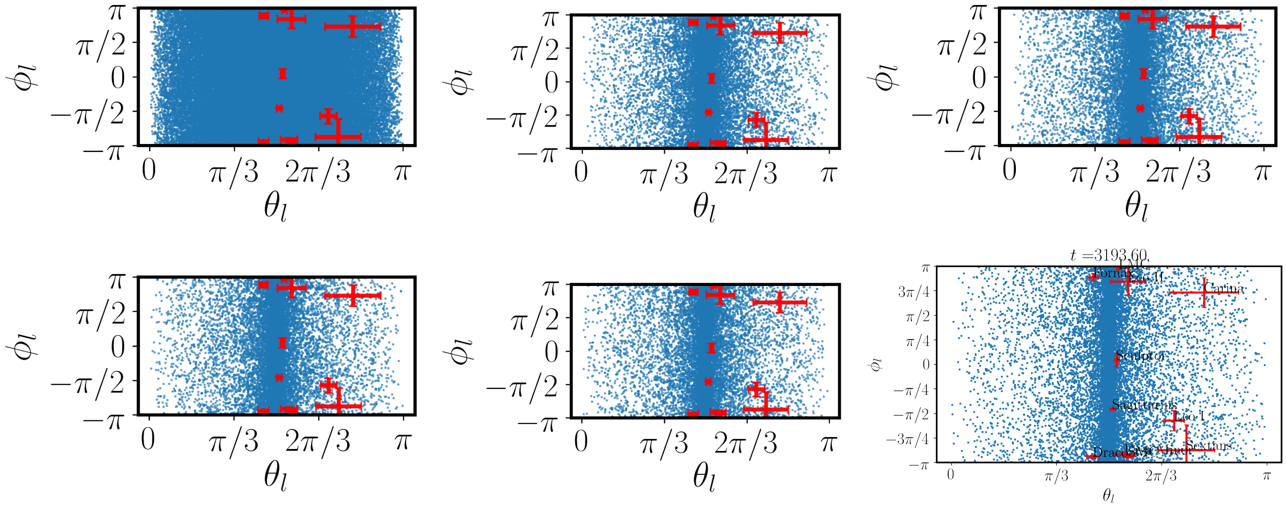

Figure 3.10 Snapshots of the angular poles for all the test particles under the potential of the **monopole**-dominated configuration. The progression shows snapshots every $4\tau_s$. Red markers are the orbital poles of the Milky Way classical satellites.

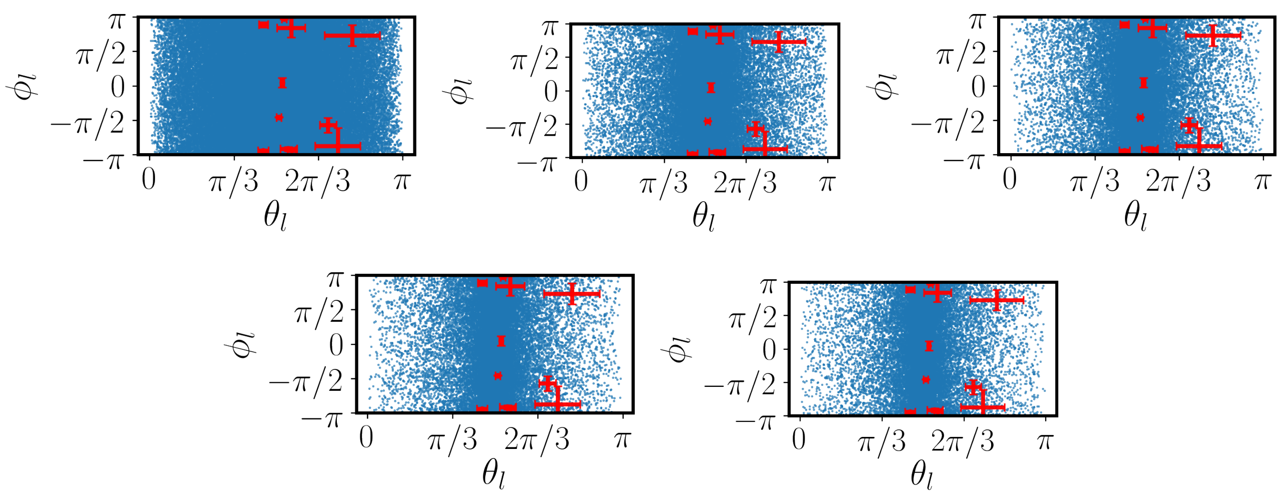

Figure 3.11 Same as in Figure 3.10 but now the progresion shows snapshots every $0.25\tau_s$.

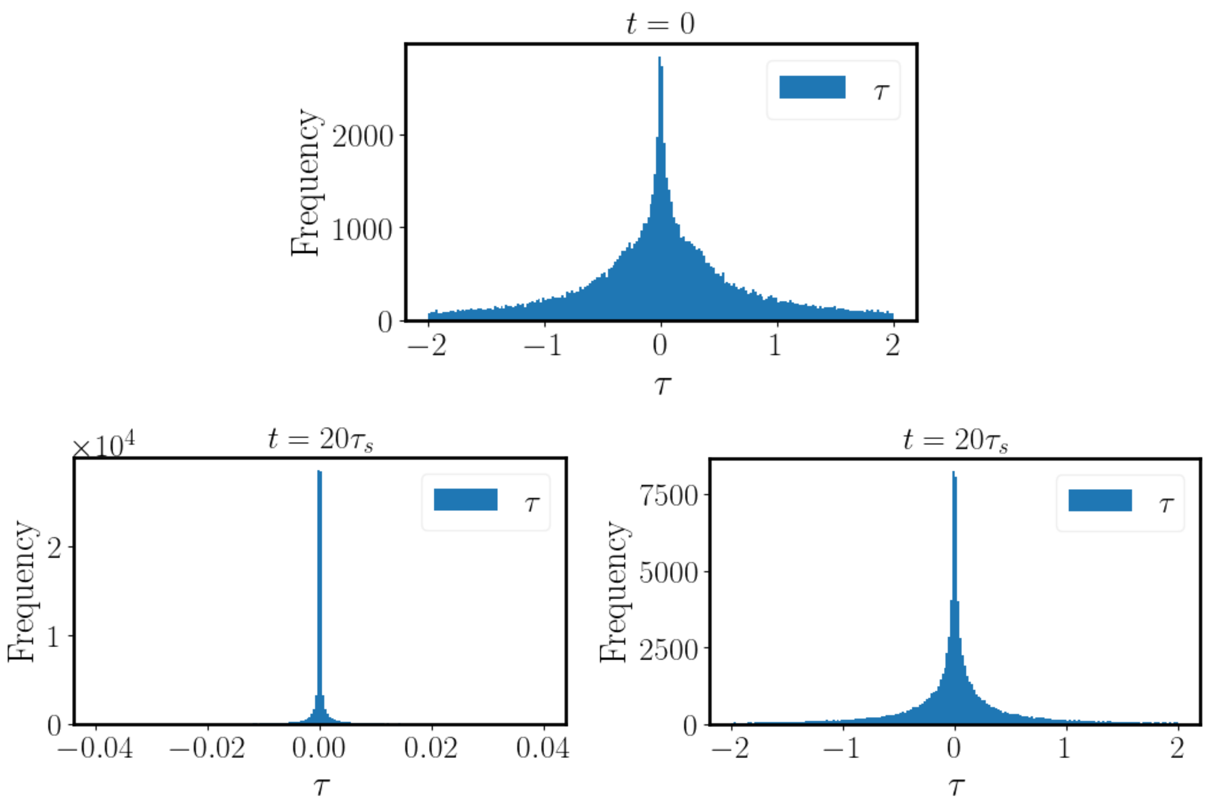

Figure 3.12 Snapshots of the histograms of all the 10^4 test particles torsions $\tau(t)$. In the top the distribution of values at initial time $\tau(0)$ is shown, and in the bottom the result at the asymptotic time $\tau(20\tau_s)$ is shown for the monopole (in the left) and **dipole**-dominated (right) configurations.

A curve is plane if it has zero torsion at all points, or in the case of a parametrized trajectory, at all times. As the evolution of $\tau(t)$ for each test particle is not tracked separately, it can only be said that particles tend to stay in close to planar trajectories.

This result toghether with the result that the test particles orbital poles accumulate near $\theta_l = \pi/2$ tells that in the multiSFDM (Ψ_{100}, Ψ_{210}) configurations test particles tend corotate in planar polar orbits.

3.5 Results for the $v_{\max} = v_{\text{esc}}/4, 3v_{\text{esc}}/4, v_{\text{esc}}$ cases

So far, the results with the test particle initial speeds bounded at $v_{\max} = v_{\text{esc}}/2$ have been the main attention points. In this section, the results still with random direction of the test particles initial velocity but now with different bounds on the initial speed, specifically $v_{\max} = v_{\text{esc}}/4, 3v_{\text{esc}}/4$ and $v_{\max} = v_{\text{esc}}$ will be presented to complete and contrast with the already analyzed $v_{\text{esc}}/2$ case.

The polar and azimuthal (θ_l, ϕ_l) angles of all the 10^5 test particles orbital poles after the $t = 20\tau_s$ evolution time are plotted in Figure 3.13. From the left to the right panels, the four different runs are plotted in increasing speed bound, for both monopole and **dipole**-dominated configurations. Notice that for the 2 lower bounded speed runs $v_{\max} = v_{\text{esc}}/4, v_{\text{esc}}/2$ the test particles orbital poles show a clear accumulation around $\theta = \pi/2$ for both monopole and **dipole**-dominated configurations, whereas for the 2 higher bounded speed runs $v_{\max} = 3v_{\text{esc}}/4, v_{\text{esc}}$ the orbital poles distribution is nearly isotropical in both configurations. The dependency of the

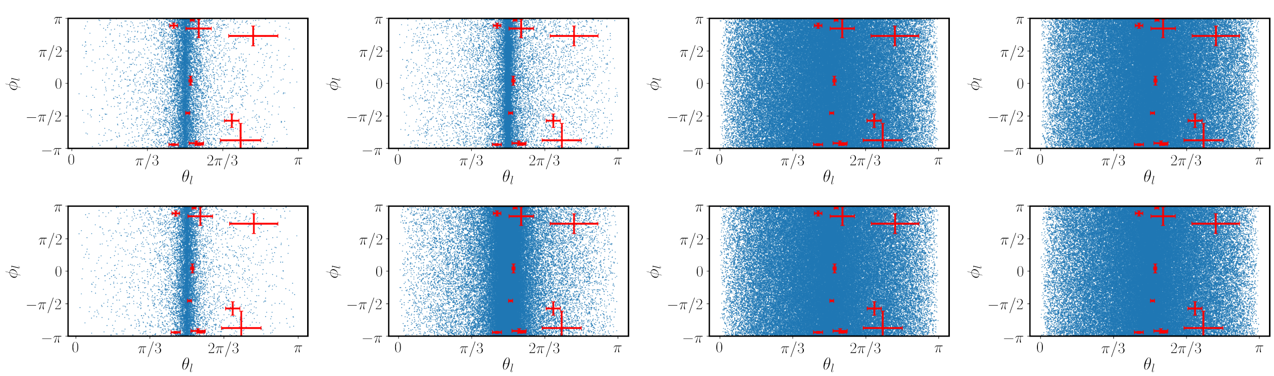

Figure 3.13 Polar θ_l and azimuthal ϕ_l angles of the 10^5 test particles orbital poles after an evolution time $t = 20\tau_s$. From left to right panels the $v_{\max} = v_{\text{esc}}/4, v_{\text{esc}}/2, 3v_{\text{esc}}/4$ and $v_{\max} = v_{\text{esc}}$ runs are plotted. In the upper panel the results correspond to the **monopole**-dominated configuration whereas in the bottom those of the **dipole**-dominated configuration. The red markers are the orbital poles of the Milky Way classical satellites calculated from the velocity data of Pawlowski and Kroupa [2013].

anisotropy in the orbital poles for different initial speed bounds thus adds an extra parameter to the analysis of specific galaxy system observations.

3.6 Disc stability

A dark matter halo should be able to host a disc-like structure as the observed in disc or spiral galaxies. It is important that the proposed axi-symmetric halo does not destroy the disc structure due to the potential wells produced by the dipole component.

To model a stellar disc hosted in a multiSFDM (Ψ_{100}, Ψ_{210}) halo four major assumptions are stated:

- The gravitational potential of the galaxy is dominated by the dark matter .
- The dark matter halo will be a stationary multiSFDM configuration.
- The disc stars are approximated as test particles orbiting inside the halo.
- The interaction between particles is neglected.

A set of 10^4 test particles initially distributed in a double exponential disc with dimensionless scale length $a_d = 1/3$ and extension $R \sim 1$ is evolved in time. Each test particle is assigned with an initial velocity

$$\mathbf{v}(0) = v_h(r, \theta)\hat{\phi}$$

where $v_h(r, \theta)$ is the circular velocity due to the multiSFDM (Ψ_{100}, Ψ_{210}) halo of a particle located at (r, θ) (Equation 2.23). In the top left panel of Figure 3.14 a histogram of the initial radial distribution of test particles is plotted and in the top panel of Figure 3.15, the 3 dimensional plot of the test particle positions in galactocentric cartesian coordinates (x, y, z) is shown.

In the top right panel of Figure 3.14 a histogram of the radial distribution of test particles after evolving during a time $t = 20\tau_s$ under the influence of the **monopole**-dominated configuration potential is shown and in the bottom right panel the positions in heliocentric (l, b) coordinates are plotted. The main characteristic to note is that the disc is not destroyed, the disk-like shape is preserved but with a larger scale length and a larger thickness (as seen in the 3D plot in Figure 3.15) due to the attraction produced by the blobs of the dipolar component.

The opposite happens in the **dipole**-dominated configuration, the disc is destroyed, given the deep potential wells in the z-axis produced by the dipolar component.

Andromeda galaxy system do not have satellites with polar orbits, satellites are at $\theta \approx 45°$ from the disc plane. The found polar orbits could be aplied to Andromeda supposing that the dark matter halo symmetry axis does not correspond to the stellar disc symmetry axis, for that a time evolution run with a disc tilted with respect to the dark matter equatorial plane was made, unfortunally tilted discs are distroyed by the axial position of the potential minima of the dipolar contribution in both configurations.

3.7 Control run

In order to check the differential equations system solver and to compare with the results obtained with the multiSFDM (Ψ_{100}, Ψ_{210}) configurations, a control run with the same number of test particles and the same initial conditions was made. In this control run, the system of test particles was evolved under the influence of the potential due to an equilibrium solution of the Schrödinger-Poisson system, a newtonian boson star. The ground state solution Ψ_{100},

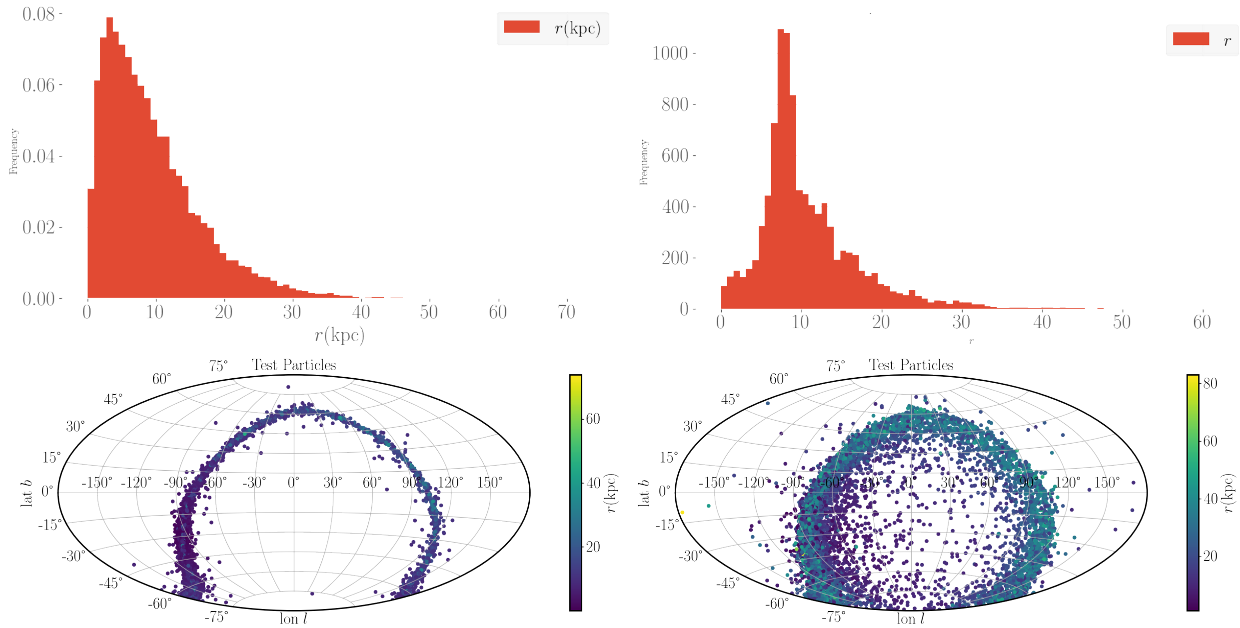

Figure 3.14 Upper panel: Histogram of the set of 10^4 test particles in a double exponential disc distribution at initial time (left panel) and at final evolution time (right) under the influence of the **monopole**-dominated configuration potential. Bottom panel: Plot of the positions of the 10^4 test particles in heliocentric (l, b) coordinates.

characterized with initial amplitude $\Psi_{100}(0) = 1$ and total mass $N_T = 2$ was used as the dark matter halo, this solution is plotted in Figure 1.3 in Chapter 1.

The top panel of Figure 3.16 show the initial and test particle positions in cartesian coordinates (x, y, z) and after a time evolution of $t = 20\tau_s$, while the middle panel shows the histograms at $t = 20\tau_s$ of the (r, θ) coordinates of the test particles, the spherically symmetric boson star potential keeps the particles spherically distributed, but the radial distribution changes with a larger amount of particles at $0 < r \leq 100$ kpc.

The orbital poles stay spherically distributed as well during the entire evolution as shown in the bottom panel of Figure 3.16 where the orbital poles of all the test particles are plotted at $t = 20\tau_s$ in two different projections.

This behaviuor would be spected in any spherical halo, in particular a Navarro-Frenk-White halo, given the symmetry of the particles position and velocities as well as the potential itself, only if triaxiality is considered the results could differ.

3.8 Tri-axial Navarro-Frenk-White potential

The Navarro-Frenk-White profile is based on spherical average of the resulting halos in the cold dark matter N-body simulations, although the halos are visible not spherical, for that reason a triaxial model would describe better the non-sphericity in the density profiles.

One could think that the non-sphericity in the cold dark matter simulations halos could give the same results than the multiSFDM (Ψ_{100}, Ψ_{210}) halos. Therefore in this section a non-

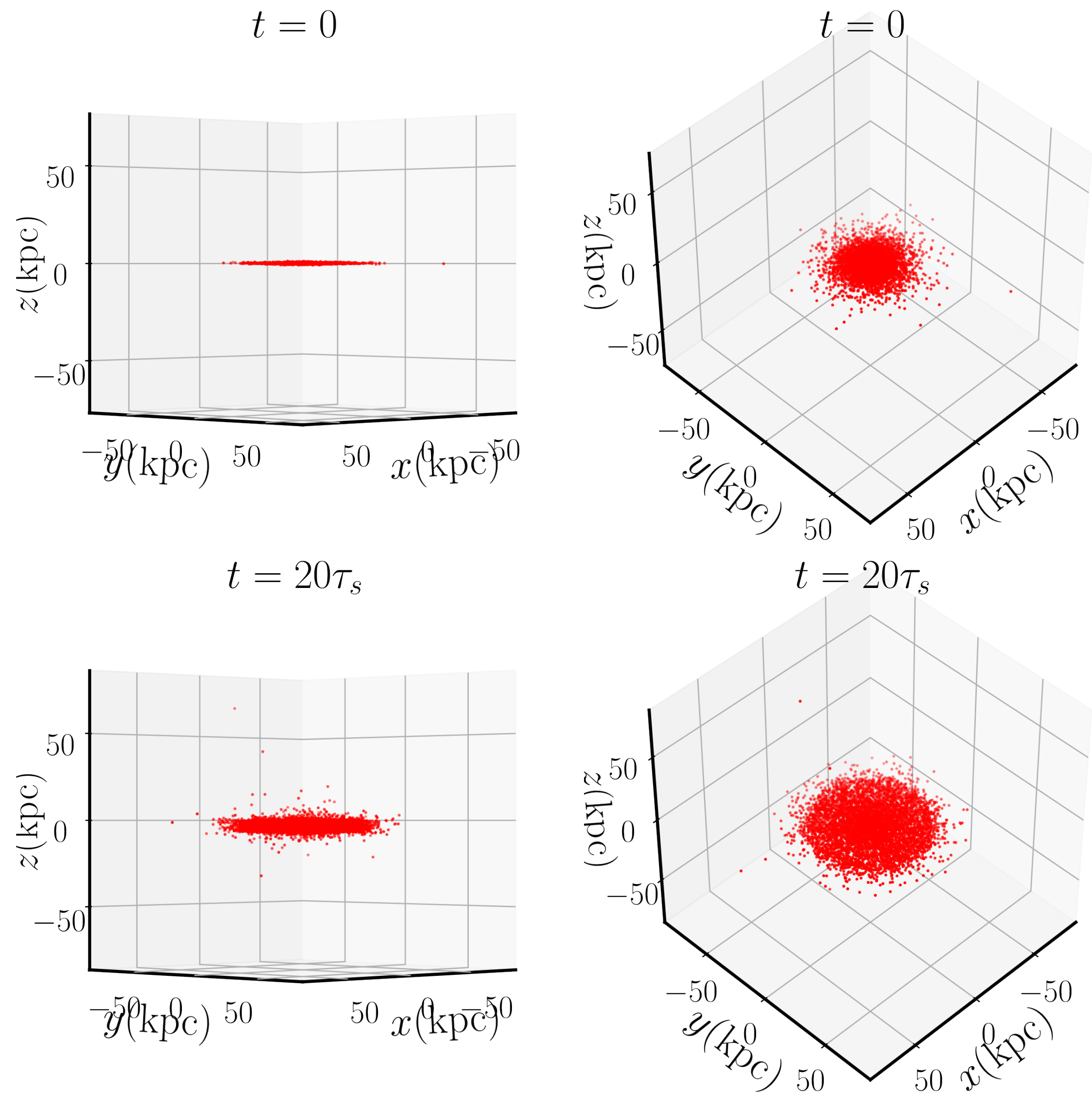

Figure 3.15 Upper panel: Set of 10^4 test particles in a double exponential disc distribution at initial time seen at two different perspectives. The initial characteristic radius of the disc is $\sim$ 30kpc. Bottom panel: Test particles distribution after evolving during $t = 20\tau_s$ under the influence of the **monopole**-dominated configuration potential, the radius is now $\sim$ 50kpc.

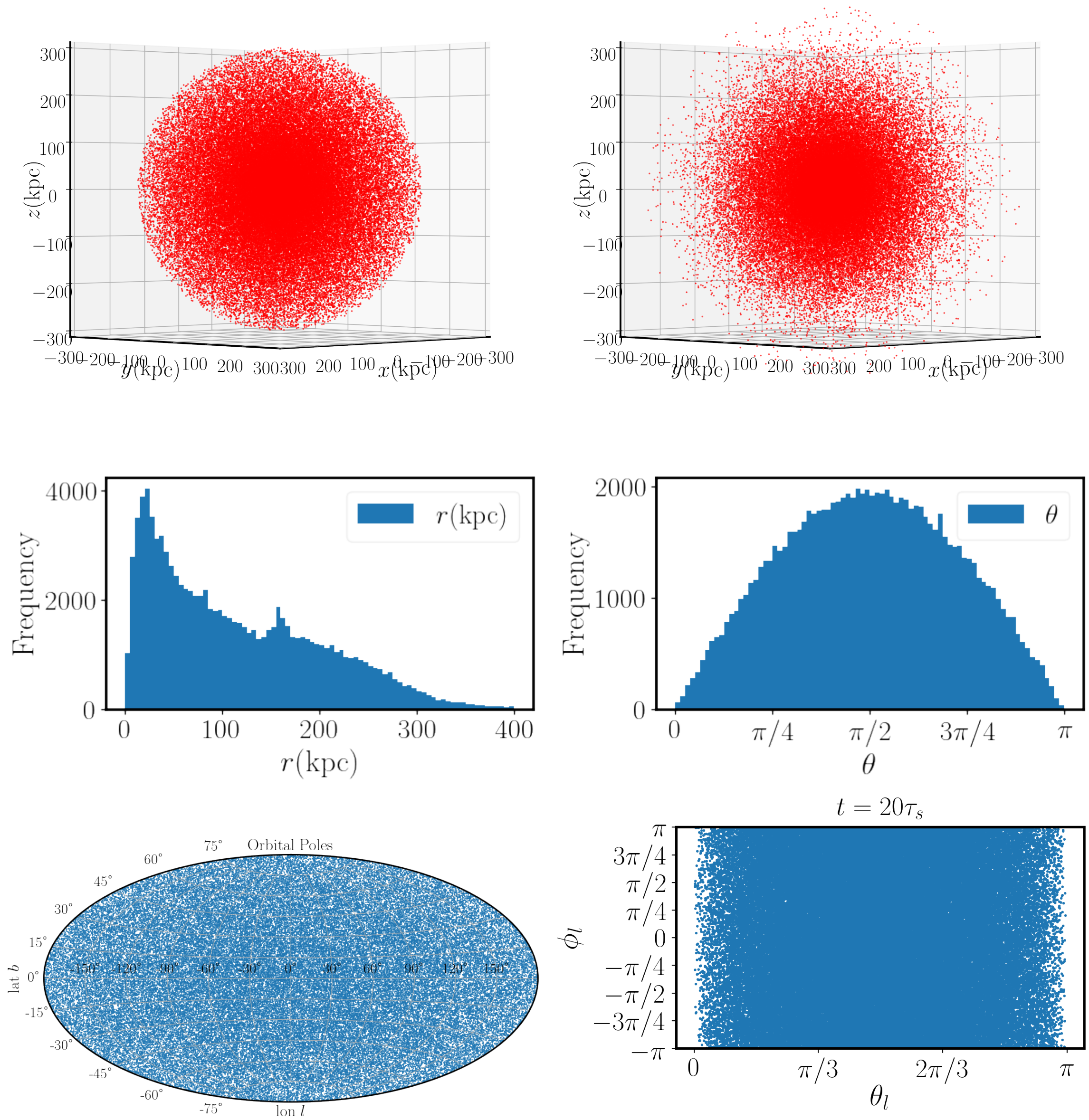

Figure 3.16 Top panel: 3D plot of the initial test particle positions (left) and the final (right) particle positions after evolving $t = 20\tau_s$ under the boson star potential. Middle panel: Histograms at final evolution of the (r, θ) spherical coordinates of the test particles after a $t = 20\tau_s$ evolution. Bottom panel: scatter plot of the orbital poles at final evolution time in spherical (l, b) (left) and (r, θ) (right) coordinates.

spherically symmetric Navarro-Frenk-White halo whose mass density could resemble that of a multiSFDM (Ψ_{100}, Ψ_{210}) halo is studied. The density profile has the same functional form of the usual Navarro-Frenk-White halo [Jing and Suto, 2002]:

$$\rho(x, y, z) = \frac{\rho_0}{(\varrho/r_s)(1 + \varrho/r_s)^2} \tag{3.1}$$

with the triaxiality given by the modification of the radial coordinate to an ellipsoidal one:

$$\varrho^2 = \alpha^2 \left(\frac{x^2}{\alpha^2} + \frac{y^2}{\beta^2} + \frac{z^2}{\delta^2} \right)$$

here r_s is the scale length, ρ_0 the characteristic density and α, β, γ are the axis lengths.

For the halo to resemble the multiSFDM (Ψ_{100}, Ψ_{210}) **monopole**-dominated configuration the distortion only along two directions was made, so that the triaxiality shows an oblate halo $\alpha = \beta = 0.5$ and $\delta = 1$. Density plots of the projection on the xy and xz planes of the mass density are shown in Figure 3.17.

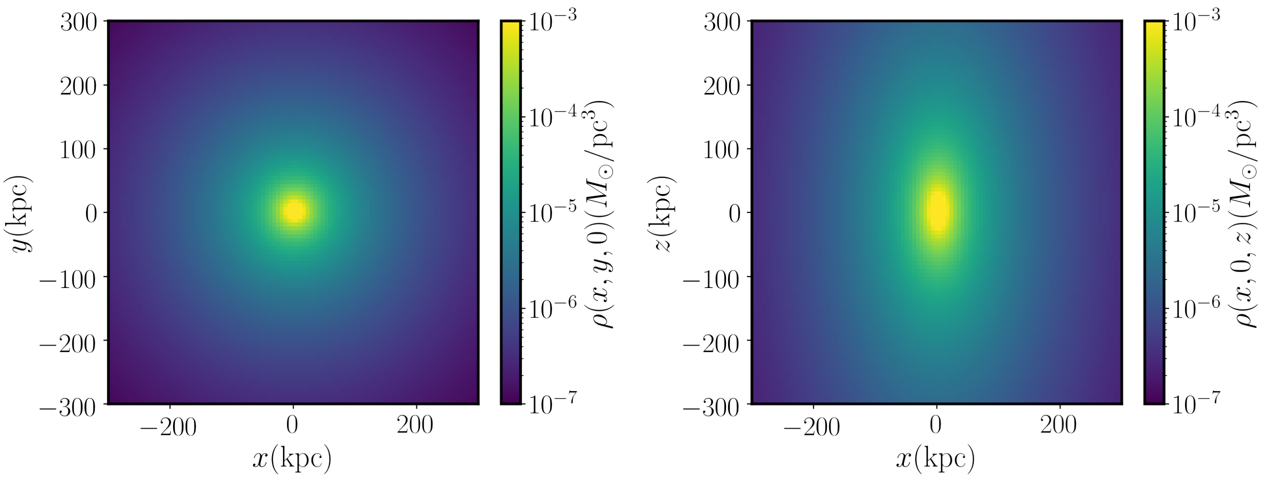

Figure 3.17 Tri-axial Navarro-Frenk-White mass density $\rho(x, y, z)$. In the left panel a density plot of the projection on the $xy-$plane of the mass density is shown, and in the right panel, the projection on the $xz-$plane.

For this halo a similar procedure than in the multiSFDM (Ψ_{100}, Ψ_{210}) configurations is followed, a set of 10^5 test particles with random initial positions, random initial velocity direction, and random initial speed bounded at $v_{\max} = v_{\text{esc}}/2$ is evolved in time under the influence of the gravitational potential sourced by the mass density of equation (3.1), the density plot of the projection on the ρz-plane of the potential is shown in Figure 3.18.

In Figure 3.19 the test particles initial positions and the position after evolving during $t = 20\tau_s$ are plotted in galactocentric cartesian coordinates.

Instead Figure 3.20 show the histograms of the radial r and polar θ spherical coordinates at initial time in the upper panel for all test particles and the coordinates of the particles that at final evolution time are in the $30 \leq r \leq 300$ kpc, i.e. at satellite distances, in the bottom panel.

The θ histogram resembles the histogram of the **dipole**-dominated multiSFDM (Ψ_{100}, Ψ_{210}) configuration (Figure 3.7), without the two picks in the poles $\theta = 0, \pi$. Although there is

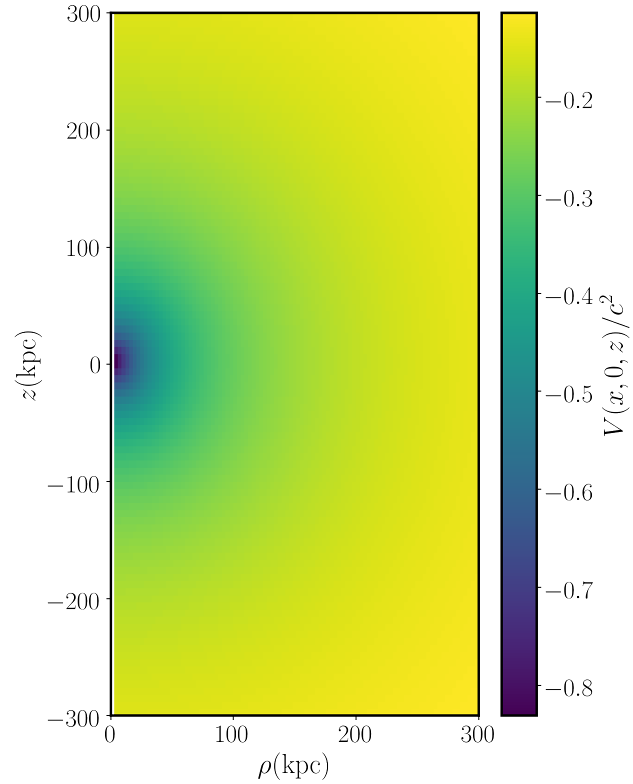

Figure 3.18 Projection on the ρz-plane of the tri-axial Navarro-Frenk-White potential $V(x, y, z)/c^2$.

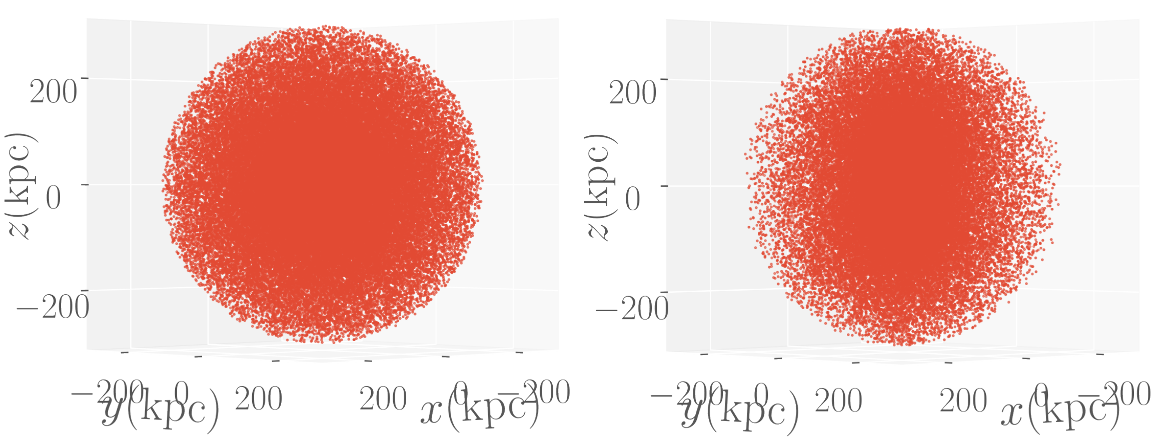

Figure 3.19 3D plot of the positions at $t = 0$ (left panel), and at $t = 20\tau_s$ (right panel) of the 10^5 test particles evolving under the triaxial Navarro-Frenk-White gravitational potential.

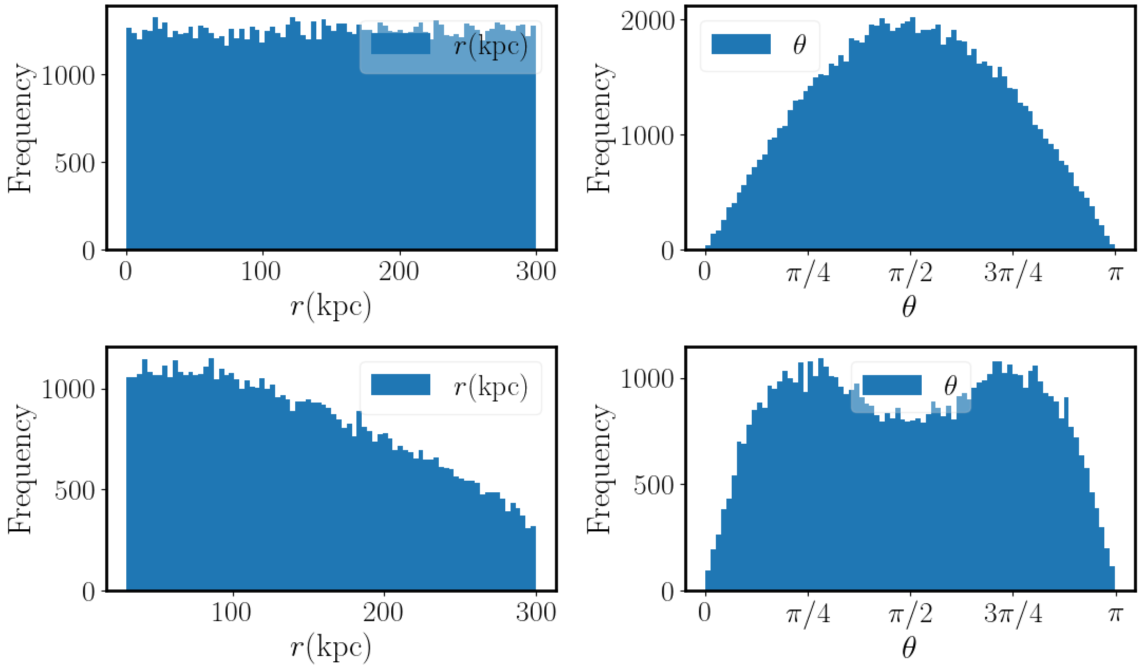

Figure 3.20 Top panel: Histograms of the initial (r, θ) positions of the 10^5 test particles. Bottom panel: Histograms of the radial and polar positions of the test particles within 30 and 300 kpc after a $20\tau_s$ evolution under the triaxial Navarro-Frenk-White potential.

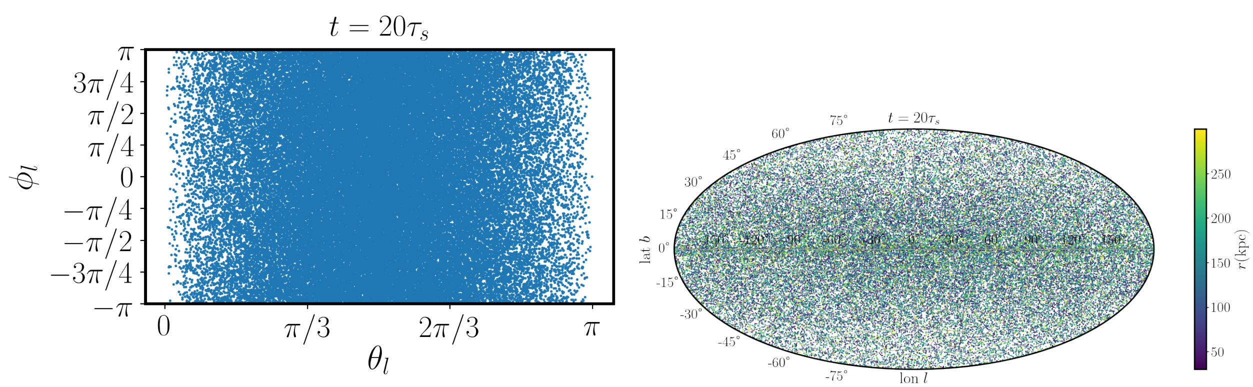

Figure 3.21 Polar angle θ_l and azimuthal angle ϕ_l (left panel) and longitude l and latitude b (right panel) in galactocentric coordinates of the orbital poles of the test particles that after a $20\tau_s$ time evolution under the triaxial Navarro-Frenk-White potential are in a distance interval 30kpc $\leq$ r $\leq$ 300kpc.

an anisotropy level in the particle distribution it is not as high than the observed in both multiSFDM (Ψ_{100}, Ψ_{210}) configurations.

Another important thing needed to compare is the orbital poles distribution, this configuration show a completely different behaviour than the multiSFDM (Ψ_{100}, Ψ_{210}) configurations, the scatter plot in Figure 3.21 of the polar and azimuthal angles of the test particles at the end of the evolution time shows that the orbital poles do not concentrate near $\theta = \pi/2$ (as in the case of **dipole**-dominated), nor in clusters around $(\theta = \pi/2, \phi = \pi/2)$ or $(\theta = \pi/2, \phi = \pi)$ (as in the **monopole**-dominated scenario), instead they appear isotropically distributed (compare Figure 3.21 with the upper left panel on Figure 3.10).

Although the triaxial Navarro-Frenk-White profile used in this section is axisymmetric and comparable with the multiSFDM (Ψ_{100}, Ψ_{210}) configurations, the results are not as promising to explain the anisotropic behaviour of the Milky Way (or M31) satellites as the multiSFDM (Ψ_{100}, Ψ_{210}) model, since the potential do not include the minimums far from the galactic plane produced by the (2,1,0) mode as the multiSFDM (Ψ_{100}, Ψ_{210}) halos do.

Chapter 4

Rotation Curves

At galactic scales any dark matter model has to be able to explain the observed rotation curves of galaxies. To verify whether the multiSFDM configurations are consistent with the Milky Way rotation curve, a simple model of a galaxy consisting of three components:

- A stellar disc,
- a spherical bulge,
- a dark matter halo in multiSFDM configuration

is assumed. Other components as the spiral arms, HI gas disc, bars, or the central super-massive black hole will not be considered. The circular velocity of a star due to these components is

$$v(r) = \sqrt{v_h^2 + v_d^2 + v_b^2} \tag{4.1}$$

where the subscripts (h, d, b) stand for halo, (stellar) disc, and bulge, respectively.

Stellar disc

To model the Milky Way stellar disc, the disc width and the spiral arms will be neglected, to end up with a razor-thin exponential disc profile whose surface mass density Σ_d in cylindrical coordinates (ρ, φ, z) is given by

$$\Sigma_d(\rho) = \Sigma_0 e^{-\rho/a_d},$$

where Σ_0 is the surface mass density at the origin (the galactic center), and a_d is the disc scale length. The total mass of the disc is the surface integral of Σ_d:

$$M_d = \int_0^{2\pi} \int_0^{\infty} \Sigma_d(\rho)\rho d\rho d\varphi = 2\pi\Sigma_0 a_d^2$$

The squared circular velocity due to this density profile is [Freeman, 1970]

$$v_d^2 = \frac{GM_d y^2}{2a_d} \left(I_0\left(\frac{y}{2}\right) K_0\left(\frac{y}{2}\right) - I_1\left(\frac{y}{2}\right) K_1\left(\frac{y}{2}\right) \right), \tag{4.2}$$

where I_n and K_n are the modified Bessel functions of the first and second kind, respectively, evaluated at $y/2$ were y is defined as $y \equiv \rho/a_d$.

Bulge

The central galaxy bulge is assumed to be spherically symmetric and thus is modeled using an exponential density profile [de Vaucouleurs, 1958, Sofue et al., 2009], in spherical coordinates (r, θ, ϕ) is given by:

$$\rho_b(r) = \rho_0 e^{-r/a_b},$$

where ρ_0 is the central density and a_b is the bulge scale length.

The squared circular velocity due to this profile is

$$v_b^2 = \frac{GM(r)}{r} \tag{4.3}$$

where

$$M(r) = \int_0^{2\pi} \int_0^{\pi} \int_0^{r} \rho_b(r) r^2 dr \sin(\theta) d\theta d\varphi = M_b \left(1 - \left(1 + \frac{r}{a_b} + \frac{r^2}{2a_b^2}\right) e^{-r/a_b}\right).$$

is the enclosed mass at radius r and M_b is the total mass of the bulge, related to the central density by $\rho_0 = M_b/(8\pi a_d^3)$.

Dark matter halo

To model the dark matter halo, the multiSFDM (Ψ_{100}, Ψ_{210}) and multiSFDM (Ψ_{100}, Ψ_{200}) configurations will be used, for these there are two parameters to fit, namely λ and $\hat{\mu}$. The circular velocity of a particle due to these axi-symmetric halos is given by

$$v_h = c\lambda \sqrt{\rho \left.\frac{\partial V}{\partial \rho}\right|_{z=0}}, \tag{4.4}$$

where V is the self gravitational potential produced by the Bose-Einstein condensate in the approximation of equation (2.10). Here the usual expression for the circular velocity of an axi-symmetric potential $\sqrt{\rho \left.\frac{\partial V}{\partial \rho}\right|_{z=0}}$ has to be multiplied by λ because of the scaling property $v_h \to \lambda v_h$ in the Schrödinger-Poisson system.

Finally, equations (4.2,4.3,4.2) have to be substituted in equation (4.1) to complete the information of the model. A total of six parameters to fit is obtained, namely $(\hat{\mu}, \lambda, M_d, a_d, M_b, a_b)$.

The circular velocity measurements of the Milky Way stars from Sofue [2012] data are fitted using the Markov Chain Monte Carlo (MCMC) method, sampling the parameter space from uniform priors. A total of 10^4 steps with 30 % burn-in and 300 walkers are used to sample the parameter space. The posterior parameters and the 1σ and 2σ confidence levels were calculated using the Lmfit [Newville et al., 2014] and Emcee [Foreman-Mackey et al., 2013] Python packages.

In the top panel of Figure 4.1 the fits of the Milky Way rotation curve for all solutions in the multiSFDM (Ψ_{100}, Ψ_{210}) family are plotted, and in the bottom panel with the multiSFDM (Ψ_{100}, Ψ_{200}) family.

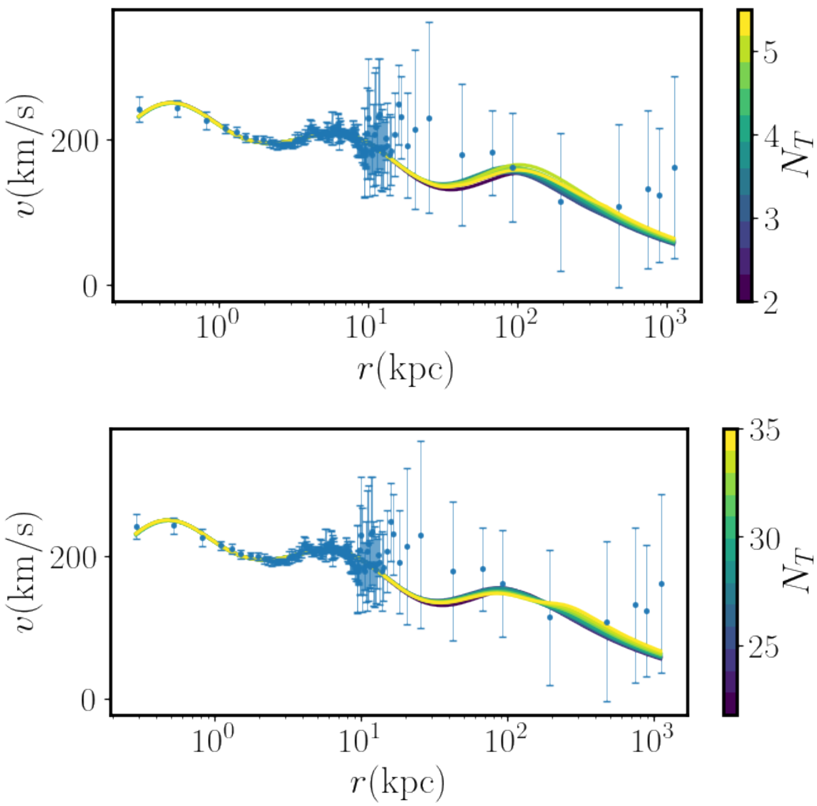

Figure 4.1 Fit of the Milky Way rotation curve for all solutions in the multiSFDM (Ψ_{100}, Ψ_{210}) family (upper panel) and for the multiSFDM (Ψ_{100}, Ψ_{200}) family (bottom panel). Data points and error bars (blue) are taken from Sofue [2012].

Table 4.1 Mean value, 1σ and 2σ spread of the parameters of the Milky Way MCMC fit. Columns 3-5 for the **dipole**-dominated configuration. Columns 6-8 for the **monopole**-dominated configuration.

		dipole-dominated			**monopole**-dominated		
Name	Units	Mean	1σ	2σ	Mean	1σ	2σ
(1)	(2)	(3)	(4)	(5)	(6)	(7)	(8)
λ	10^{-3}	0.94	0.3	0.64	0.59	0.19	0.39
$\hat{\mu}$	1/kpc	70.733	44.141	68.744	59.868	39.485	67.336
μc^2	10^{-25} eV	4.5228	2.8225	4.3957	3.8281	2.5248	4.3056
M_d	$10^{10} M_\odot$	6.7594	0.3385	0.7177	6.7494	0.3484	0.7438
a_d	kpc	3.1269	0.1199	0.2491	3.1265	0.1207	0.2521
M_b	$10^{10} M_\odot$	0.9737	0.0454	0.0909	0.9733	0.0453	0.0904
a_b	kpc	0.1353	0.0118	0.0237	0.1354	0.0119	0.0238

In Figure 4.2 only the contributions of the stellar disc and bulge are plotted to note that the dark matter contribution acts principally in the outer regions of the galaxy, flattening the rotation curve at radii $r > 50$ kpc. These fits show that the multiSFDM configurations allow fitting galaxy rotation curves .

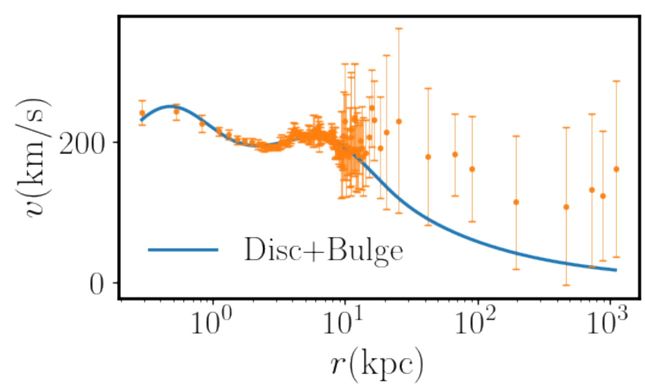

Figure 4.2 The Milky Way rotation curve (blue solid line) without the dark matter contribution.

As the fitting parameters have a low variation ($< 10\%$) within the family, only for the particular cases of the **monopole**-dominated and **dipole**-dominated configurations, the posterior parameters and the 1σ and 2σ confidence levels are shown in Table 4.1. A stellar disc mass $M_d = (6.7 \pm 0.3) \times 10^{10} M_\odot$ and scale length $a_d = (3.12 \pm 0.12)$ kpc are found for both configurations, similarly the bulge mass $M_b = (9.7 \pm 0.4) \times 10^9 M_\odot$ and scale length $a_b = 135 \pm 12$pc are obtained for both configurations, being in agreement with results from fittings with Navarro-Frenk-White halos [see, for example, Maleki et al., 2020].

On the top panel of Figure 4.3 the fit of the total rotation curve is plotted along with the contribution of the disc and bulge for the **monopole**-dominated configuration and in Figure 4.4 for the **dipole**-dominated configuration. On the bottom panel of Figure 4.3 and Figure 4.4 the posterior parameters of the MCMC fit are plotted in a triangle plot for the monopole and **dipole**-dominated configurations respectively.

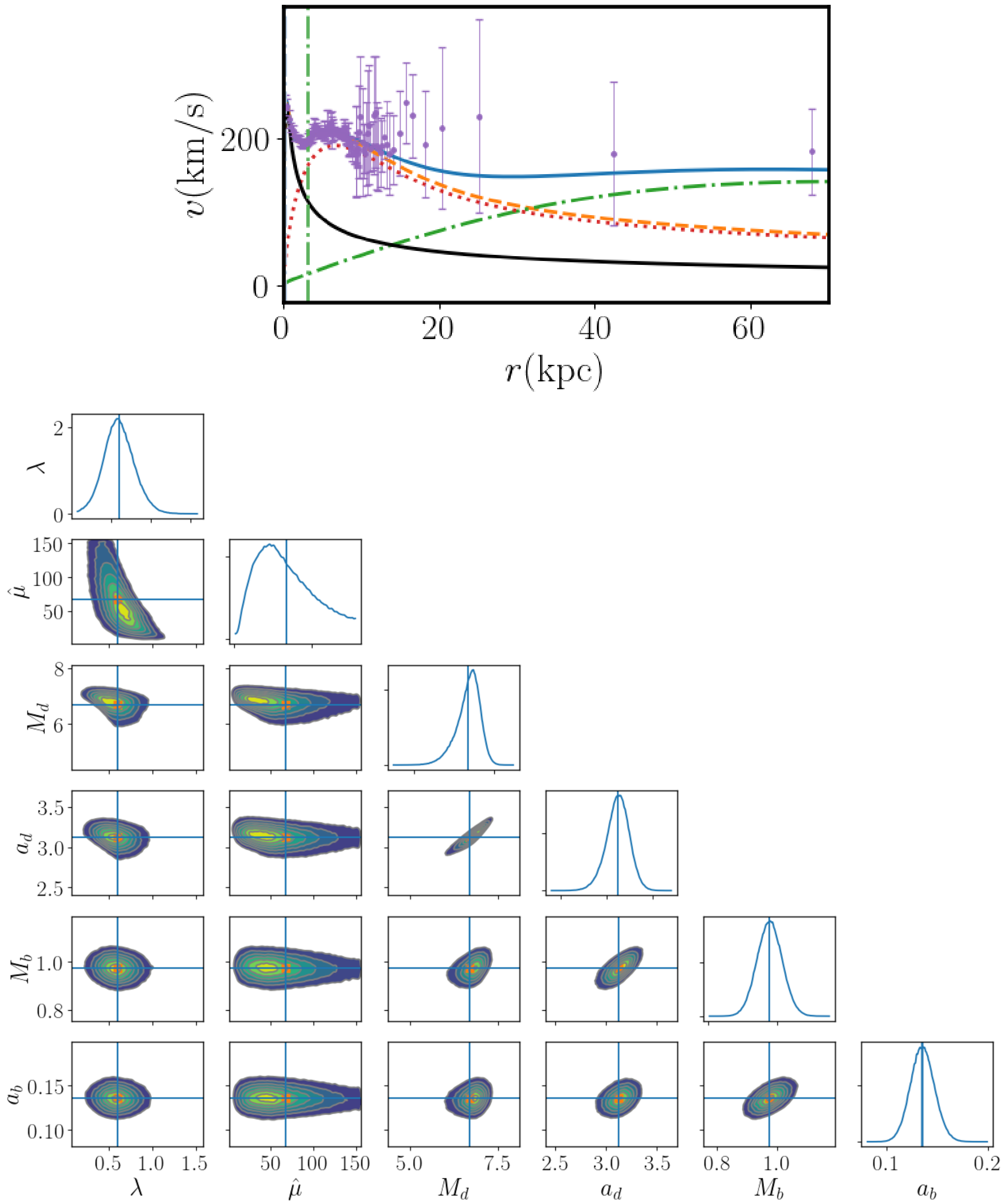

Figure 4.3 Top panel: Fit of the Milky Way rotation curve (blue solid line), the disc (red dotted line) and bulge (black continuous line) are modeled with exponential profiles and the dark matter halo (green dash-dotted line) with the **monopole**-dominated multiSFDM (Ψ_{100}, Ψ_{210}) configuration $\eta = 0.36$. The contribution of disc and bulge without dark matter is plotted with the orange dashed line. The green dash-dotted vertical line represent the stellar disc scale length a_d. Data points and error bars (red) are taken from Sofue [2012]. Bottom panel: Triangle plot of the 1D and 2D posterior parameters. Here $\hat{\mu}$ is in 1/kpc units, λ in 10^{-3} dimensions, a_d, a_b in kpc units, and M_d, M_b in $10^{10} M_\odot$ units.

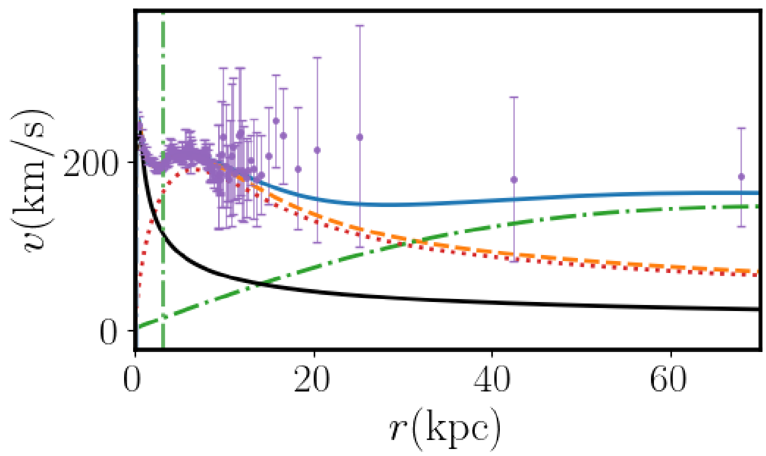

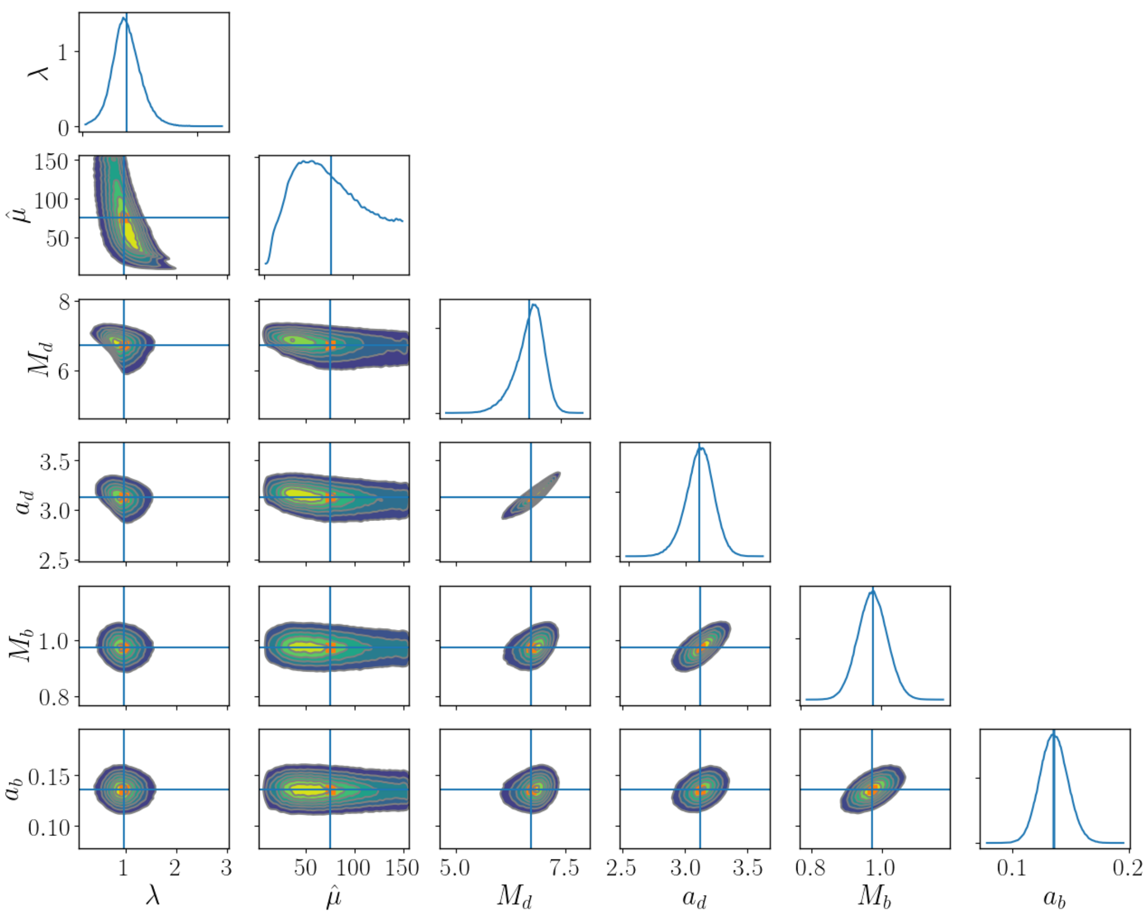

Figure 4.4 Same as in Figure 4.3 but now for the **dipole**-dominated configuration $\eta = 3$.

Chapter 5

Conclusions

In this work the scalar field dark matter model was studied, this dark matter model behave at large scales as the standard cold dark matter model, but at galactic scales, distances $<$ 1 Mpc the results have substantial differences. In this model the halo is a self-gravitating Bose-Einstein condensate ruled by the Gross-Pitaevskii-Poisson equations, usually only the ground state equilibrium solution is considered, but now multiple states equilibrium solutions, the multiSFDM, are proposed to solve the small-scale problems of cold dark matter .

When more than multiple self-gravitating scalar fields of the same mass, or equivalently, multiple states of a scalar field, are considered, the usual Gross-Pitaevskii-Poisson system becomes a variant Gross-Pitaevskii-Poisson system with multiple Gross-Pitaevskii equations and a Poisson equation sourced by the sum of the densities of all scalar fields. In Chapter 2, families of equilibrium solutions are found in the case of multiSFDM (Ψ_{100}, Ψ_{210}) , (Ψ_{100}, Ψ_{200}) and (Ψ_{100}, Ψ_{211}) configurations.

To explain the anisotropic distribution of satellite galaxies observed in the Milky Way , M31 and Cen A systems, two particular solutions of the multiSFDM (Ψ_{100}, Ψ_{210}) configuration with different density-mode domination, namely, the **monopole**-dominated and **dipole**-dominated were tasted as dark matter halos. In Chapter 3 a set of 10^5 test particles with random initial velocities and positions were evolved under the potential of both halos, in the asymptotic time, the test particles distributed anisotropically, with high concentrations at the poles and the equatorial plane of the system, a result in contrast with the one obtained if the single-state configuration consisting only in the ground state Ψ_{100} is considered, where particles remain spherically distributed, changing only the radial distribution.

Not only the position distribution of galaxy satellites is anisotropic, the satellites seem to be co-rotating in a plane made by its current positions, to that purpose, the test particles angular momentum directions (orbital poles) were analyzed. The **monopole**-dominated configuration obtained the best results, the orbital poles of the test particles that, in the asymptotic time were located at satellite galaxies distances ($30\,\mathrm{kpc} \leq \mathrm{r} \leq 300\,\mathrm{kpc}$), accumulate at preferential regions around the polar angle $\theta_l = \pi/2$ (or $b = 0°$) and the azimuthal angle $\phi_l = \pi$, $3\pi/2$ (or $l = 180°, 270°$) compatible with the data points of the Milky Way satellite galaxies, for which the mean direction of the seven most concentrated (Fornax, LMC, SMC, Ursa Minor Carina, Draco and Leo II) orbital poles points at $(l = 179.5°, b = -9°)$ Pawlowski and Kroupa [2020]. Then a single particle, interpreted as a satellite galaxy hosted by a galaxy with a multiSFDM (Ψ_{100}, Ψ_{210}) dark matter halo, farther than 30 kpc from the galactic origin, would be more likely to have a polar flat orbit.

The analysis is supported by the consistency check of the multiSFDM (Ψ_{100}, Ψ_{210}) solutions with the stability of disc distributions. Through a set of test particles initially placed in a double exponential thin disc distribution perpendicular to the axis of the dipole, and with initial circular velocities, the time evolution under the monopole and **dipole**-dominated configurations was studied. In the **monopole**-dominated configuration the disk-like shape was preserved in the asymptotic time but with a wider and larger disc. Unfortunately, in the **dipole**-dominated configuration, the deeper potential wells given by the density blobs destroyed the disc-like distribution. As not all galaxy systems mentioned have satellites with polar orbits, Andromeda for one case where the satellites are at $\theta \approx 45°$, a time evolution with a disc tilted with respect to the equatorial plane was also run, in this way the results of the polar orbits could be applied to Andromeda supposing that the dark matter halo symmetry axis does not correspond to the stellar disc symmetry axis, unfortunately tilted discs are destroyed in both configurations. Nevertheless, these results are valid in the long-term, which means that eventually the observed polar angles of Andromeda satellites should approach $\theta = \pi/2$ as time evolves.

The motion of test particles traveling on top of a spherical symmetric ground state solution (Ψ_{100}) of the Schrödinger-Poisson system as a control case was studied too, under a spherical potential, test particles with this general initial conditions preserve the spherical symmetry in both positions and orbital poles in the asymptotic time.

In order to check if a non-spherical cold dark matter halo could give similar results to the multiSFDM (Ψ_{100}, Ψ_{210}) configurations, in Section 3.8 a run with a triaxial Navarro-Frenk-White profile distorted along two directions to resemble the **monopole**-dominated configuration was carried. In this axi-symmetric potential an in-homogeneous distribution of particles at asymptotic time is found, but unlike the multiSFDM (Ψ_{100}, Ψ_{210}) configurations, the isotropy in the orbital poles is preserved.

In Chapter 4 the consistency of the multiSFDM solutions with the Milky Way rotation curve was checked obtaining similar fits with the multiSFDM (Ψ_{100}, Ψ_{210}) and (Ψ_{100}, Ψ_{200}) families of solutions, a scalar field particle mass $\mu c^2 \sim 10^{-25}$eV was obtained, the fiducial mass used in the test particle simulations. A simple mass model with stellar razor-thin disc, spherical exponential bulge and multiSFDM halo was proposed, obtaining a stellar disc mass of $(6.7 \pm 0.3) \times 10^{10} M_\odot$ with length scale $a_d = (3.12 \pm 0.12)\,\mathrm{kpc}$, and a stellar bulge mass of $(9.7 \pm 0.4) \times 10^9 M_\odot$ with length scale $a_b = (0.13 \pm 0.01)\,\mathrm{kpc}$.

The test particle trajectories in two sample configurations with different mass ratio η between modes have been studied, nevertheless there is a continuous universe of solutions with different η for whose effects may vary, and thus potentially useful to study each particular galaxy system. Furthermore, beside the two-states equilibrium solutions of the Gross-Pitaevskii-Poisson equations considered here, there is a even larger universe of multistate configurations with different excited states or different number of excited states to explore, implying that the ultralight bosonic scalar field dark matter model has potential to explain the plane of satellites problem in the known cases of the Milky Way , Andromeda and Cen A or even different small-scale problems to come.

Bibliography

Kevork Abazajian, George M. Fuller, and Wallace H. Tucker. Direct detection of warm dark matter in the x-ray. *The Astrophysical Journal*, 562(2):593–604, dec 2001. doi:10.1086/323867.

Miguel Alcubierre, J. Barranco, Argelia Bernal, Juan Degollado, Alberto Diez-Tejedor, Miguel Megevand, and Olivier Sarbach. *l-boson stars.* Classical and Quantum Gravity*, 35, 08 2018. doi:10.1088/1361-6382/aadcb6.*

Alexandre Arbey, Julien Lesgourgues, and Pierre Salati. Quintessential haloes around galaxies. Physical Review D*, 64:123528, 2001. doi:10.1103/PhysRevD.64.123528.*

Alexandre Arbey, Julien Lesgourgues, and Pierre Salati. Cosmological constraints on quintessential halos. Physical Review D*, 65:083514, Apr 2002. doi:10.1103/PhysRevD.65.083514.*

Alexandre Arbey, Julien Lesgourgues, and Pierre Salati. Galactic halos of fluid dark matter. Physical Review D*, 68:023511, Jul 2003. doi:10.1103/PhysRevD.68.023511.*

Argelia Bernal and F. Siddhartha Guzmán. Scalar field dark matter: Nonspherical collapse and late-time behavior. Phys. Rev. D*, 74:063504, Sep 2006. doi:10.1103/PhysRevD.74.063504.*

Michael Boylan-Kolchin, Volker Springel, Simon D. M. White, Adrian Jenkins, and Gerard Lemson. Resolving cosmic structure formation with the Millennium-II Simulation. Monthly Notices of the Royal Astronomical Society*, 398(3):1150–1164, 09 2009. ISSN 0035-8711. doi:10.1111/j.1365-2966.2009.15191.x.*

Michael Boylan-Kolchin, James S. Bullock, and Manoj Kaplinghat. Too big to fail? The puzzling darkness of massive Milky Way subhaloes. Monthly Notices of the Royal Astronomical Society: Letters*, 415(1):L40–L44, 07 2011. ISSN 1745-3925. doi:10.1111/j.1745-3933.2011.01074.x.*

Michael Boylan-Kolchin, James S. Bullock, and Manoj Kaplinghat. The Milky Way's bright satellites as an apparent failure of ΛCDM. Monthly Notices of the Royal Astronomical Society*, 422(2):1203–1218, 2012. doi:10.1111/j.1365-2966.2012.20695.x.*

Hubert L. Bray. On Dark Matter, Spiral Galaxies, and the Axioms of General Relativity. 2010. doi:10.1090/conm/599/11945.

Tom Broadhurst, Ivan De Martino, Hoang Nhan Luu, George F. Smoot, and S.-H. Henry Tye. Ghostly galaxies as solitons of Bose-Einstein dark matter. Physical Review D*, 101(8), Apr 2020. ISSN 2470-0029. doi:10.1103/physrevd.101.083012.*

James S. Bullock and Michael Boylan-Kolchin. Small-scale challenges to the Λ*CDM paradigm.* Annual Review of Astronomy and Astrophysics*, 55(1):343–387, 2017. doi:10.1146/annurev-astro-091916-055313.*

C G Böhmer and T Harko. Can dark matter be a Bose–Einstein condensate? Journal of Cosmology and Astroparticle Physics*, 2007(06):025–025, jun 2007. doi:10.1088/1475-7516/2007/06/025.*

Erminia Calabrese and David N. Spergel. Ultra-light dark matter in ultra-faint dwarf galaxies. Monthly Notices of the Royal Astronomical Society*, 460(4):4397–4402, 05 2016. ISSN 0035-8711. doi:10.1093/mnras/stw1256.*

Pierre-Henri Chavanis. Mass-radius relation of newtonian self-gravitating Bose-Einstein condensates with short-range interactions. I. Analytical results. Physical Review D*, 84:043531, Aug 2011. doi:10.1103/PhysRevD.84.043531.*

Shu-Rong Chen, Hsi-Yu Schive, and Tzihong Chiueh. Jeans analysis for dwarf spheroidal galaxies in wave dark matter. Monthly Notices of the Royal Astronomical Society*, 468(2):1338–1348, 02 2017. ISSN 0035-8711. doi:10.1093/mnras/stx449.*

Douglas Clowe, Maruša Bradač, Anthony H. Gonzalez, Maxim Markevitch, Scott W. Randall, Christine Jones, and Dennis Zaritsky. A direct empirical proof of the existence of dark matter. The Astrophysical Journal*, 648(2):L109–L113, aug 2006. doi:10.1086/508162.*

Pedro Colin, Vladimir Avila-Reese, and Octavio Valenzuela. Substructure and halo density profiles in a warm dark matter cosmology. The Astrophysical Journal*, 542(2):622–630, oct 2000. doi:10.1086/317057.*

Monica Colpi, Stuart L. Shapiro, and Ira Wasserman. Boson stars: Gravitational equilibria of self-interacting scalar fields. Phys. Rev. Lett.*, 57:2485–2488, Nov 1986. doi:10.1103/PhysRevLett.57.2485.*

A. R. Conn, G. F. Lewis, R. A. Ibata, Q. A. Parker, D. B. Zucker, A. W. McConnachie, N. F. Martin, D. Valls-Gabaud, N. Tanvir, M. J. Irwin, A. M. N. Ferguson, and S. C. Chapman. The three-dimensional structure of the M31 satellite system; strong evidence for an inhomogeneous distribution of satellites. The Astrophysical Journal*, 766(2):120, mar 2013. doi:10.1088/0004-637x/766/2/120.*

W. J. G. de Blok, Albert Bosma, and Stacy McGaugh. Simulating observations of dark matter dominated galaxies: towards the optimal halo profile. Monthly Notices of the Royal Astronomical Society*, 340(2):657–678, 04 2003. ISSN 0035-8711. doi:10.1046/j.1365-8711.2003.06330.x.*

G. de Vaucouleurs. Photoelectric photometry of the Andromeda Nebula in the UBV system. The Astrophysical Journal*, 128:465, November 1958. doi:10.1086/146564.*

John Dubinski and R. G. Carlberg. The Structure of Cold Dark Matter Halos. The Astrophysical Journal*, 378:496, September 1991. doi:10.1086/170451.*

Ricardo A. Flores and Joel R. Primack. Observational and Theoretical Constraints on Singular Dark Matter Halos. The Astrophysical Journal, *427:L1–L4, May 1994. doi:10.1086/187350.*

R. Foot and Z.K. Silagadze. Thin disk of co-rotating dwarfs: A fingerprint of dissipative (mirror) dark matter? Physics of the Dark Universe, *2(3):163–165, 2013. ISSN 2212-6864. doi:10.1016/j.dark.2013.10.001.*

Daniel Foreman-Mackey, David W. Hogg, Dustin Lang, and Jonathan Goodman. emcee: The MCMC hammer. Publications of the Astronomical Society of the Pacific, *125(925):306–312, Mar 2013. ISSN 1538-3873. doi:10.1086/670067.*

K. C. Freeman. On the Disks of Spiral and S0 Galaxies. The Astrophysical Journal, *160:811, June 1970. doi:10.1086/150474.*

Gaia Collaboration. Gaia data release 2 - Kinematics of globular clusters and dwarf galaxies around the Milky Way. Astronomy & Astrophysics, *616:A12, 2018. doi:10.1051/0004-6361/201832698.*

Shea Garrison-Kimmel, Miguel Rocha, Michael Boylan-Kolchin, James S. Bullock, and Jaspreet Lally. Can feedback solve the too-big-to-fail problem? Monthly Notices of the Royal Astronomical Society, *433(4):3539–3546, 06 2013. ISSN 0035-8711. doi:10.1093/mnras/stt984.*

Jennifer M. Gaskins. A review of indirect searches for particle dark matter. Contemporary Physics, *57(4):496–525, 2016. doi:10.1080/00107514.2016.1175160.*

Alma X. González-Morales, David J. E. Marsh, Jorge Peñarrubia, and Luis A. Ureña-López. Unbiased constraints on ultralight axion mass from dwarf spheroidal galaxies. Monthly Notices of the Royal Astronomical Society, *472(2):1346–1360, 08 2017. ISSN 0035-8711. doi:10.1093/mnras/stx1941.*

F. Governato, C. Brook, L. Mayer, A. Brooks, G. Rhee, J. Wadsley, P. Jonsson, B. Willman, G. Stinson, T. Quinn, and P. Madau. Bulgeless dwarf galaxies and dark matter cores from supernova-driven outflows. Nature, *463:203–206, 2010. doi:10.1038/nature08640.*

F. S. Guzmán and L. Arturo Ureña López. Gravitational atoms: General framework for the construction of multistate axially symmetric solutions of the Schrödinger-Poisson system. Physical Review D, *101:081302, Apr 2020. doi:10.1103/PhysRevD.101.081302.*

F Siddhartha Guzmán and Tonatiuh Matos. Scalar fields as dark matter in spiral galaxies. Classical and Quantum Gravity, *17(1):L9–L16, dec 2000. doi:10.1088/0264-9381/17/1/102.*

F. Siddhartha Guzmán and L. Arturo Ureña López. Evolution of the Schrödinger-Newton system for a self-gravitating scalar field. Physical Review D, *69:124033, Jun 2004. doi:10.1103/PhysRevD.69.124033.*

Francisco S. Guzmán. Stability of multistate configurations of fuzzy dark matter. Astronomische Nachrichten, *342(1-2):398–403, 2021. doi:10.1002/asna.202113941.*

F.S. Guzmán, T. Matos, and H.B. Villegas. Scalar fields as dark matter in spiral galaxies: comparison with experiments. Astronomische Nachrichten, 320(3):97–104, 1999. doi:10.1002/1521-3994(199907)320:3<97::AID-ASNA97>3.0.CO;2-M.

T. Harko. Evolution of cosmological perturbations in Bose–Einstein condensate dark matter. Monthly Notices of the Royal Astronomical Society, 413(4):3095–3104, 05 2011a. ISSN 0035-8711. doi:10.1111/j.1365-2966.2011.18386.x.

T Harko. Bose-Einstein condensation of dark matter solves the core/cusp problem. Journal of Cosmology and Astroparticle Physics, 2011(05):022–022, may 2011b. doi:10.1088/1475-7516/2011/05/022.

Renée Hlozek, Daniel Grin, David J. E. Marsh, and Pedro G. Ferreira. A search for ultralight axions using precision cosmological data. Phys. Rev., D91(10):103512, 2015. doi:10.1103/PhysRevD.91.103512.

Philip F. Hopkins. A stable finite-volume method for scalar field dark matter. Monthly Notices of the Royal Astronomical Society, 489(2):2367–2376, Jul 2019. ISSN 1365-2966. doi:10.1093/mnras/stz1922.

Wayne Hu, Rennan Barkana, and Andrei Gruzinov. Fuzzy cold dark matter: The wave properties of ultralight particles. Phys. Rev. Lett., 85:1158–1161, Aug 2000. doi:10.1103/PhysRevLett.85.1158.

Lam Hui, Jeremiah P. Ostriker, Scott Tremaine, and Edward Witten. Ultralight scalars as cosmological dark matter. Phys. Rev., D95(4):043541, 2017. doi:10.1103/PhysRevD.95.043541.

Rodrigo A Ibata, Geraint F Lewis, Anthony R Conn, Michael J Irwin, Alan W McConnachie, Scott C Chapman, Michelle L Collins, Mark Fardal, Annette MN Ferguson, Neil G Ibata, A. Dougal Mackey, Nicolas F. Martin, Julio Navarro, R. Michael Rich, David Valls-Gabaud, and Lawrence M. Widrow. A vast, thin plane of corotating dwarf galaxies orbiting the Andromeda galaxy. Nature, 493(7430):62, 2013. doi:10.1038/nature11717.

Dennis J. Hegyi and Keith A. Olive. Can galactic halos be made of baryons? Physics Letters B, 126(1):28–32, 1983. ISSN 0370-2693. doi:10.1016/0370-2693(83)90009-6.

M. J. Jee, H. C. Ford, G. D. Illingworth, R. L. White, T. J. Broadhurst, D. A. Coe, G. R. Meurer, A. van der Wel, N. Benitez, J. P. Blakeslee, R. J. Bouwens, L. D. Bradley, R. Demarco, N. L. Homeier, A. R. Martel, and S. Mei. Discovery of a ringlike dark matter structure in the core of the galaxy cluster cl 0024+17. The Astrophysical Journal, 661(2):728–749, jun 2007. doi:10.1086/517498.

S. U. Ji and S. J. Sin. Late-time phase transition and the galactic halo as a Bose liquid. II. The effect of visible matter. Physical Review D, 50:3655–3659, Sep 1994. doi:10.1103/PhysRevD.50.3655.

Y. P. Jing and Yasushi Suto. Triaxial Modeling of Halo Density Profiles with High-Resolution N-Body Simulations. The Astrophysical Journal, 574(2):538–553, August 2002. doi:10.1086/341065.

Anatoly Klypin, Andrey V. Kravtsov, Octavio Valenzuela, and Francisco Prada. Where are the missing galactic satellites? The Astrophysical Journal*, 522(1):82–92, sep 1999. doi:10.1086/307643.*

Andreas Koch and Eva K. Grebel. The anisotropic distribution of M31 satellite galaxies: A polar great plane of early-type companions. The Astronomical Journal*, 131(3):1405–1415, mar 2006. doi:10.1086/499534.*

P. Kroupa, C. Theis, and C. M. Boily. The great disk of Milky-Way satellites and cosmological sub-structures. Astronomy & Astrophysics*, 431(2):517–521, 2005. doi:10.1051/0004-6361:20041122.*

Kroupa, P., Famaey, B., de Boer, K. S., Dabringhausen, J., Pawlowski, M. S., Boily, C. M., Jerjen, H., Forbes, D., Hensler, G., and Metz, M. Local-group tests of dark-matter concordance cosmology - towards a new paradigm for structure formation. Astronomy & Astrophysics*, 523:A32, 2010. doi:10.1051/0004-6361/201014892.*

Jae-weon Lee and In-gyu Koh. Galactic halos as boson stars. Phys. Rev. D*, 53:2236–2239, Feb 1996. doi:10.1103/PhysRevD.53.2236.*

Federico Lelli, Stacy S. McGaugh, James M. Schombert, and Marcel S. Pawlowski. One law to rule them all: The radial acceleration relation of galaxies. The Astrophysical Journal*, 836 (2):152, feb 2017. doi:10.3847/1538-4357/836/2/152.*

Julien Lesgourgues, Alexandre Arbey, and Pierre Salati. A light scalar field at the origin of galaxy rotation curves. New Astronomy Reviews*, 46(12):791–799, 2002. ISSN 1387-6473. doi:10.1016/S1387-6473(02)00247-6. An Alternative to Dark Matter: MOND.*

D. G. Levkov, A. G. Panin, and I. I. Tkachev. Gravitational Bose-Einstein condensation in the kinetic regime. Phys. Rev. Lett.*, 121:151301, Oct 2018. doi:10.1103/PhysRevLett.121.151301.*

W. B. Lin, D. H. Huang, X. Zhang, and R. Brandenberger. Nonthermal production of weakly interacting massive particles and the subgalactic structure of the universe. Phys. Rev. Lett.*, 86:954–957, Feb 2001. doi:10.1103/PhysRevLett.86.954.*

Andrew Lipnicky and Sukanya Chakrabarti. Is the vast polar structure of dwarf galaxies a serious problem for Λ cold dark matter? Monthly Notices of the Royal Astronomical Society*, 468 (2):1671–1682, 2017. doi:10.1093/mnras/stx286.*

V Lora, Juan Magaña, Argelia Bernal, F.J Sánchez-Salcedo, and E.K Grebel. On the mass of ultra-light bosonic dark matter from galactic dynamics. Journal of Cosmology and Astroparticle Physics*, 2012(02):011–011, feb 2012. doi:10.1088/1475-7516/2012/02/011.*

D. Lynden-Bell. Dwarf galaxies and globular clusters in high velocity hydrogen streams. Monthly Notices of the Royal Astronomical Society*, 174:695–710, March 1976. doi:10.1093/mnras/174.3.695.*

Juan Magaña and Tonatiuh Matos. A brief review of the scalar field dark matter model. Journal of Physics: Conference Series, *378:012012, aug 2012. doi:10.1088/1742-6596/378/1/012012.*

Juan Magaña, Tonatiuh Matos, Abril Suárez, and F.J Sánchez-Salcedo. Structure formation with scalar field dark matter: the field approach. Journal of Cosmology and Astroparticle Physics, *2012(10):003–003, oct 2012. doi:10.1088/1475-7516/2012/10/003. URL https://doi.org/10.1088/1475-7516/2012/10/003.*

Alireza Maleki, Shant Baghram, and Sohrab Rahvar. Constraint on the mass of fuzzy dark matter from the rotation curve of the milky way. Phys. Rev. D, *101:103504, May 2020. doi:10.1103/PhysRevD.101.103504.*

David J. E. Marsh and Pedro G. Ferreira. Ultralight scalar fields and the growth of structure in the universe. Physical Review D, *82:103528, Nov 2010. doi:10.1103/PhysRevD.82.103528.*

David J. E. Marsh and Ana-Roxana Pop. Axion dark matter, solitons and the cusp–core problem. Monthly Notices of the Royal Astronomical Society, *451(3):2479–2492, 06 2015. ISSN 0035-8711. doi:10.1093/mnras/stv1050.*

David J.E. Marsh. Axion cosmology. Physics Reports, *643:1–79, 2016. ISSN 0370-1573. doi:10.1016/j.physrep.2016.06.005. Axion cosmology.*

Tonatiuh Matos and L. Arturo Ureña López. Flat rotation curves in scalar field galaxy halos. General Relativity and Gravitation, *39:1279–1286, 2007. doi:10.1007/s10714-007-0470-y.*

Tonatiuh Matos and L. Arturo Ureña-López. Quintessence and scalar dark matter in the universe. Classical and Quantum Gravity, *17(13):L75–L81, jun 2000. doi:10.1088/0264-9381/17/13/101.*

Tonatiuh Matos and L. Arturo Ureña-López. Further analysis of a cosmological model with quintessence and scalar dark matter. Physical Review D, *63:063506, Feb 2001. doi:10.1103/PhysRevD.63.063506.*

Tonatiuh Matos, F Siddhartha Guzmán, and L Arturo Ureña-López. Scalar field as dark matter in the universe. Classical and Quantum Gravity, *17(7):1707–1712, mar 2000. doi:10.1088/0264-9381/17/7/309.*

Stacy S. McGaugh. The baryonic tully-fisher relation of gas-rich galaxies as a test of Λ CDM and MOND. The Astronomical Journal, *143(2):40, jan 2012. doi:10.1088/0004-6256/143/2/40.*

M. Membrado, A. F. Pacheco, and J. Sañudo. Hartree solutions for the self-Yukawian boson sphere. Phys. Rev. A, *39:4207–4211, Apr 1989. doi:10.1103/PhysRevA.39.4207.*

Manuel Metz, Pavel Kroupa, and Helmut Jerjen. The spatial distribution of the Milky Way and Andromeda satellite galaxies. Monthly Notices of the Royal Astronomical Society, *374(3): 1125–1145, 12 2007. ISSN 0035-8711. doi:10.1111/j.1365-2966.2006.11228.x.*

Manuel Metz, Pavel Kroupa, and Noam I. Libeskind. The orbital poles of Milky Way satellite galaxies: A rotationally supported disk of satellites. The Astrophysical Journal, *680(1):287–294, jun 2008. doi:10.1086/587833.*

Manuel Metz, Pavel Kroupa, and Helmut Jerjen. Discs of satellites: the new dwarf spheroidals. Monthly Notices of the Royal Astronomical Society*, 394(4):2223–2228, 2009. doi:10.1111/j.1365-2966.2009.14489.x.*

M. Milgrom. A modification of the Newtonian dynamics as a possible alternative to the hidden mass hypothesis. The Astrophysical Journal*, 270:365–370, July 1983a. doi:10.1086/161130.*

M. Milgrom. A modification of the Newtonian dynamics - Implications for galaxies. The Astrophysical Journal*, 270:371–383, July 1983b. doi:10.1086/161131.*

M. Milgrom. A modification of the newtonian dynamics : implications for galaxy systems. The Astrophysical Journal*, 270:384–389, July 1983c. doi:10.1086/161132.*

Mordehai Milgrom. Mond—theoretical aspects. New Astronomy Reviews*, 46(12):741–753, 2002. ISSN 1387-6473. doi:10.1016/S1387-6473(02)00243-9. An Alternative to Dark Matter: MOND.*

Philip Mocz, Mark Vogelsberger, Victor H. Robles, Jesús Zavala, Michael Boylan-Kolchin, Anastasia Fialkov, and Lars Hernquist. Galaxy formation with BECDM – I. Turbulence and relaxation of idealized haloes. Monthly Notices of the Royal Astronomical Society*, 471(4): 4559–4570, 07 2017. ISSN 0035-8711. doi:10.1093/mnras/stx1887.*

Philip Mocz, Anastasia Fialkov, Mark Vogelsberger, Fernando Becerra, Mustafa A. Amin, Sownak Bose, Michael Boylan-Kolchin, Pierre-Henri Chavanis, Lars Hernquist, Lachlan Lancaster, and et al. First star-forming structures in fuzzy cosmic filaments. Physical Review Letters*, 123(14), Oct 2019. ISSN 1079-7114. doi:10.1103/physrevlett.123.141301.*

Philip Mocz, Anastasia Fialkov, Mark Vogelsberger, Fernando Becerra, Xuejian Shen, Victor H Robles, Mustafa A Amin, Jesús Zavala, Michael Boylan-Kolchin, Sownak Bose, Federico Marinacci, Pierre-Henri Chavanis, Lachlan Lancaster, and Lars Hernquist. Galaxy formation with BECDM – II. Cosmic filaments and first galaxies. Monthly Notices of the Royal Astronomical Society*, 494(2):2027–2044, 04 2020. ISSN 0035-8711. doi:10.1093/mnras/staa738.*

Ben Moore. Evidence against dissipation-less dark matter from observations of galaxy haloes. Nature*, 370:629–631, oct 1994. doi:10.1038/370629a0.*

Ben Moore, Sebastiano Ghigna, Fabio Governato, George Lake, Thomas Quinn, Joachim Stadel, and Paolo Tozzi. Dark matter substructure within galactic halos. The Astrophysical Journal*, 524(1):L19–L22, oct 1999. doi:10.1086/312287.*

Oliver Müller, Helmut Jerjen, Marcel S. Pawlowski, and Bruno Binggeli. Testing the two planes of satellites in the Centaurus group. Astronomy & Astrophysics*, 595:A119, 2016. doi:10.1051/0004-6361/201629298.*

Oliver Müller, Marcel S. Pawlowski, Helmut Jerjen, and Federico Lelli. A whirling plane of satellite galaxies around Centaurus A challenges cold dark matter cosmology. Science*, 359: 534, 2018. doi:10.1126/science.aao1858.*

Oliver Müller, Marcel S. Pawlowski, Federico Lelli, Katja Fahrion, Marina Rejkuba, Michael Hilker, Jamie Kanehisa, Noam Libeskind, and Helmut Jerjen. The coherent motion of Cen A dwarf satellite galaxies remains a challenge for cosmology. Astronomy & Astrophysics*, 645: L5, 2021. doi:10.1051/0004-6361/202039973.*

Vijay K. Narayanan, David N. Spergel, Romeel Davé, and Chung-Pei Ma. Constraints on the mass of warm dark matter particles and the shape of the linear power spectrum from the Ly α forest. The Astrophysical Journal*, 543(2):L103–L106, nov 2000. doi:10.1086/317269.*

Julio F. Navarro, Carlos S. Frenk, and Simon D. M. White. A Universal Density Profile from Hierarchical Clustering. The Astrophysical Journal*, 490(2):493–508, December 1997. doi:10.1086/304888.*

Julio F. Navarro, Aaron Ludlow, Volker Springel, Jie Wang, Mark Vogelsberger, Simon D. M. White, Adrian Jenkins, Carlos S. Frenk, and Amina Helmi. The diversity and similarity of simulated cold dark matter haloes. Monthly Notices of the Royal Astronomical Society*, 402 (1):21–34, 02 2010. ISSN 0035-8711. doi:10.1111/j.1365-2966.2009.15878.x.*

Matthew Newville, Till Stensitzki, Daniel B. Allen, and Antonino Ingargiola. LMFIT: Non-Linear Least-Square Minimization and Curve-Fitting for Python. September 2014. doi:10.5281/zenodo.11813.

Jens C. Niemeyer. Small-scale structure of fuzzy and axion-like dark matter. Progress in Particle and Nuclear Physics*, 113:103787, 2020. ISSN 0146-6410. doi:10.1016/j.ppnp.2020.103787.*

Se-Heon Oh, W. J. G. de Blok, Elias Brinks, Fabian Walter, and Robert C. Kennicutt. Dark and luminous matter in THINGS dwarf galaxies. The Astronomical Journal*, 141(6):193, may 2011. doi:10.1088/0004-6256/141/6/193.*

Papastergis, E., Giovanelli, R., Haynes, M. P., and Shankar, F. Is there a "too big to fail" problem in the field? A&A*, 574:A113, 2015. doi:10.1051/0004-6361/201424909.*

M. S. Pawlowski, J. Pflamm-Altenburg, and P. Kroupa. The VPOS: a vast polar structure of satellite galaxies, globular clusters and streams around the Milky Way. Monthly Notices of the Royal Astronomical Society*, 423(2):1109–1126, 06 2012. ISSN 0035-8711. doi:10.1111/j.1365-2966.2012.20937.x.*

Marcel S. Pawlowski. The alignment of SDSS satellites with the VPOS: effects of the survey footprint shape. Monthly Notices of the Royal Astronomical Society*, 456(1):448–458, 12 2016. ISSN 0035-8711. doi:10.1093/mnras/stv2673.*

Marcel S. Pawlowski. The planes of satellite galaxies problem, suggested solutions, and open questions. Modern Physics Letters A*, 33(06):1830004, 2018. doi:10.1142/S0217732318300045.*

Marcel S. Pawlowski and Pavel Kroupa. The rotationally stabilized VPOS and predicted proper motions of the Milky Way satellite galaxies. Monthly Notices of the Royal Astronomical Society*, 435(3):2116–2131, 09 2013. ISSN 0035-8711. doi:10.1093/mnras/stt1429.*

Marcel S Pawlowski and Pavel Kroupa. The Milky Way's disc of classical satellite galaxies in light of Gaia DR2. Monthly Notices of the Royal Astronomical Society*, 491(2):3042–3059, 11 2020. ISSN 0035-8711. doi:10.1093/mnras/stz3163.*

Marcel S. Pawlowski, Pavel Kroupa, and Helmut Jerjen. Dwarf galaxy planes: the discovery of symmetric structures in the Local Group. Monthly Notices of the Royal Astronomical Society*, 435(3):1928–1957, 09 2013. ISSN 0035-8711. doi:10.1093/mnras/stt1384.*

Marcel S. Pawlowski, Stacy S. McGaugh, and Helmut Jerjen. The new Milky Way satellites: alignment with the VPOS and predictions for proper motions and velocity dispersions. Monthly Notices of the Royal Astronomical Society*, 453(1):1047–1061, 08 2015. ISSN 0035-8711. doi:10.1093/mnras/stv1588.*

Pawlowski, M. S., Kroupa, P., and de Boer, K. S. Making counter-orbiting tidal debris - The origin of the Milky Way disc of satellites? Astronomy & Astrophysics*, 532:A118, 2011. doi:10.1051/0004-6361/201015021.*

P. J. E. Peebles. Large-scale background temperature and mass fluctuations due to scale-invariant primeval perturbations. The Astrophysical Journal Letters*, 263:L1–L5, December 1982. doi:10.1086/183911.*

Massimo Persic, Paolo Salucci, and Fulvio Stel. The universal rotation curve of spiral galaxies — I. The dark matter connection. Monthly Notices of the Royal Astronomical Society*, 281 (1):27–47, 07 1996. ISSN 0035-8711. doi:10.1093/mnras/278.1.27.*

Tanja Rindler-Daller and Paul R Shapiro. Complex scalar field dark matter on galactic scales. Modern Physics Letters A*, 29(02):1430002, 2014. doi:10.1142/S021773231430002X.*

Victor H. Robles and T. Matos. Flat central density profile and constant dark matter surface density in galaxies from scalar field dark matter. Monthly Notices of the Royal Astronomical Society*, 422(1):282–289, Mar 2012. ISSN 0035-8711. doi:10.1111/j.1365-2966.2012.20603.x.*

Victor H Robles, James S Bullock, and Michael Boylan-Kolchin. Scalar field dark matter: helping or hurting small-scale problems in cosmology? Monthly Notices of the Royal Astronomical Society*, 483(1):289–298, Nov 2018. ISSN 1365-2966. doi:10.1093/mnras/sty3190.*

Miguel Rocha, Annika H. G. Peter, James S. Bullock, Manoj Kaplinghat, Shea Garrison-Kimmel, Jose Oñorbe, and Leonidas A. Moustakas. Cosmological simulations with self-interacting dark matter – I. Constant-density cores and substructure. Monthly Notices of the Royal Astronomical Society*, 430(1):81–104, 01 2013. ISSN 0035-8711. doi:10.1093/mnras/sts514.*

Vera C. Rubin and Jr. Ford, W. Kent. Rotation of the Andromeda Nebula from a Spectroscopic Survey of Emission Regions. The Astrophysical Journal*, 159:379, February 1970. doi:10.1086/150317.*

Remo Ruffini and Silvano Bonazzola. Systems of self-gravitating particles in general relativity and the concept of an equation of state. Phys. Rev.*, 187:1767–1783, Nov 1969. doi:10.1103/PhysRev.187.1767.*

Varun Sahni and Limin Wang. New cosmological model of quintessence and dark matter. Physical Review D*, 62:103517, Oct 2000. doi:10.1103/PhysRevD.62.103517.*

Isabel M E Santos-Santos, Julio F Navarro, Andrew Robertson, Alejandro Benítez-Llambay, Kyle A Oman, Mark R Lovell, Carlos S Frenk, Aaron D Ludlow, Azadeh Fattahi, and Adam Ritz. Baryonic clues to the puzzling diversity of dwarf galaxy rotation curves. Monthly Notices of the Royal Astronomical Society*, 495(1):58–77, 04 2020. ISSN 0035-8711. doi:10.1093/mnras/staa1072.*

Hsi-Yu Schive, Tzihong Chiueh, and Tom Broadhurst. Cosmic Structure as the Quantum Interference of a Coherent Dark Wave. Nature Physics*, 10:496–499, 2014a. doi:10.1038/nphys2996.*

Hsi-Yu Schive, Ming-Hsuan Liao, Tak-Pong Woo, Shing-Kwong Wong, Tzihong Chiueh, Tom Broadhurst, and W-Y. Pauchy Hwang. Understanding the core-halo relation of quantum wave dark matter from 3d simulations. Phys. Rev. Lett.*, 113:261302, Dec 2014b. doi:10.1103/PhysRevLett.113.261302.*

Bodo Schwabe, Jens C. Niemeyer, and Jan F. Engels. Simulations of solitonic core mergers in ultralight axion dark matter cosmologies. Physical Review D*, 94:043513, Aug 2016. doi:10.1103/PhysRevD.94.043513.*

M.P. Silverman and R.L Mallett. Dark matter as a cosmic Bose-Einstein condensate and possible superfluid. General Relativity and Gravitation*, 34:633–649, 2002. doi:10.1023/A:1015934027224.*

Sang-Jin Sin. Late-time phase transition and the galactic halo as a Bose liquid. Physical Review D*, 50:3650–3654, Sep 1994. doi:10.1103/PhysRevD.50.3650.*

Yoshiaki Sofue. Grand Rotation Curve and Dark-Matter Halo in the Milky Way Galaxy. Publications of the Astronomical Society of Japan*, 64(4), 08 2012. ISSN 0004-6264. doi:10.1093/pasj/64.4.75. 75.*

Yoshiaki Sofue, Mareki Honma, and Toshihiro Omodaka. Unified Rotation Curve of the Galaxy — Decomposition into de Vaucouleurs Bulge, Disk, Dark Halo, and the 9-kpc Rotation Dip —. Publications of the Astronomical Society of Japan*, 61(2):227–236, 04 2009. ISSN 0004-6264. doi:10.1093/pasj/61.2.227.*

Jesper Sommer-Larsen and Alexandre Dolgov. Formation of disk galaxies: Warm dark matter and the angular momentum problem. The Astrophysical Journal*, 551(2):608–623, apr 2001. doi:10.1086/320211.*

David N. Spergel and Paul J. Steinhardt. Observational evidence for self-interacting cold dark matter. Phys. Rev. Lett.*, 84:3760–3763, Apr 2000. doi:10.1103/PhysRevLett.84.3760.*

Volker Springel et al. Simulating the joint evolution of quasars, galaxies and their large-scale distribution. Nature*, 435:629–636, 2005. doi:10.1038/nature03597.*

J. Stadel, D. Potter, B. Moore, J. Diemand, P. Madau, M. Zemp, M. Kuhlen, and V. Quilis. Quantifying the heart of darkness with GHALO – a multibillion particle simulation of a galactic halo. Monthly Notices of the Royal Astronomical Society: Letters*, 398(1):L21–L25, 09 2009. ISSN 1745-3925. doi:10.1111/j.1745-3933.2009.00699.x.*

Kung-Yi Su and Pisin Chen. Solving the cusp-core problem with a novel scalar field dark matter. Journal of Cosmology and Astroparticle Physics*, 2011(08):016–016, aug 2011. doi:10.1088/1475-7516/2011/08/016.*

Abril Suárez and Pierre-Henri Chavanis. Hydrodynamic representation of the Klein-Gordon-Einstein equations in the weak field limit: General formalism and perturbations analysis. Phys. Rev. D*, 92:023510, Jul 2015. doi:10.1103/PhysRevD.92.023510.*

Abril Suárez, Victor H Robles, and Tonatiuh Matos. A review on the scalar field/Bose-Einstein condensate dark matter model. In Accelerated Cosmic Expansion*, pages 107–142. Springer, 2014. doi:10.1007/978-3-319-02063-1_9.*

Erik J. Tollerud, Michael Boylan-Kolchin, and James S. Bullock. M31 satellite masses compared to ΛCDM subhaloes. Monthly Notices of the Royal Astronomical Society*, 440(4):3511–3519, 04 2014. ISSN 0035-8711. doi:10.1093/mnras/stu474.*

R. Brent Tully, Noam I. Libeskind, Igor D. Karachentsev, Valentina E. Karachentseva, Luca Rizzi, and Edward J. Shaya. Two planes of satellites in the Centaurus A group. The Astrophysical Journal*, 802(2):L25, apr 2015. doi:10.1088/2041-8205/802/2/l25.*

L. Arturo Ureña López and Argelia Bernal. Bosonic gas as a galactic dark matter halo. Physical Review D*, 82:123535, Dec 2010. doi:10.1103/PhysRevD.82.123535.*

Jan Veltmaat and Jens C. Niemeyer. Cosmological particle-in-cell simulations with ultralight axion dark matter. Physical Review D*, 94:123523, Dec 2016. doi:10.1103/PhysRevD.94.123523.*

M. Vogelsberger, S. Genel, V. Springel, P. Torrey, D. Sijacki, D. Xu, G. Snyder, S. Bird, D. Nelson, and L. Hernquist. Properties of galaxies reproduced by a hydrodynamic simulation. Nature*, 509:177–182, 2014. doi:10.1038/nature13316.*

Jie Wang, Sownak Bose, Carlos S. Frenk, Liang Gao, Adrian Jenkins, Volker Springel, and Simon D. M. White. Universal structure of dark matter haloes over a mass range of 20 orders of magnitude. Nature*, 585:39–42, 2020. doi:10.1038/s41586-020-2642-9.*

Asher Wasserman, Pieter van Dokkum, Aaron J. Romanowsky, Jean Brodie, Shany Danieli, Duncan A. Forbes, Roberto Abraham, Christopher Martin, Matt Matuszewski, Alexa Villaume, and et al. Spatially resolved stellar kinematics of the ultra-diffuse galaxy dragonfly 44. ii. constraints on fuzzy dark matter. The Astrophysical Journal*, 885(2):155, Nov 2019. ISSN 1538-4357. doi:10.3847/1538-4357/ab3eb9.*

Simon D. M. White, Carlos S. Frenk, Marc Davis, and George Efstathiou. Clusters, Filaments, and Voids in a Universe Dominated by Cold Dark Matter. The Astrophysical Journal*, 313: 505, February 1987. doi:10.1086/164990.*

Tak-Pong Woo and Tzihong Chiueh. High-resolution simulation on structure formation with extremely light bosonic dark matter. The Astrophysical Journal*, 697(1):850–861, may 2009. doi:10.1088/0004-637x/697/1/850.*

Donald G. York, J. Adelman, and Jr. John E. Anderson. The sloan digital sky survey: Technical summary. The Astronomical Journal*, 120(3):1579–1587, sep 2000. doi:10.1086/301513.*

F. Zwicky. On the Masses of Nebulae and of Clusters of Nebulae. The Astrophysical Journal*, 86:217, October 1937. doi:10.1086/143864.*